Electrical Machine Characterisation and Analysis for Renewable Energy Applications

David P. Cashman

A thesis submitted to the
National University of Ireland
in fullfillment of the requirements for
the degree of Doctor of Philosophy

August 2010

Research Supervisor: Dr. John G. Hayes
Research Co-Supervisor: Dr. Michael G. Egan

Department of Electrical and Electronic Engineering
University College Cork

Abstract

There has been an increased use of the doubly-fed induction machine (DFIM) in ac drive applications in recent times, particularly in the field of renewable energy systems and other high power variable-speed drives. The DFIM is widely regarded as the optimal generation system for both onshore and offshore wind turbines and has also been considered in wave power applications.

Wind power generation is the most mature renewable technology. However, wave energy has attracted a large interest recently as the potential for power extraction is very significant. Various wave energy converter (WEC) technologies currently exist with the oscillating water column (OWC) type converter being one of the most advanced. There are fundemental differences in the power profile of the pneumatic power supplied by the OWC WEC and that of a wind turbine and this causes significant challenges in the selection and rating of electrical generators for the OWC devises.

The thesis initially aims to provide an accurate per-phase equivalent circuit model of the DFIM by investigating various characterisation testing procedures. A novel testing methodology based on the series-coupling tests are employed and are found to provide a more accurate representation of the DFIM than standard IEEE testing methods. The series-coupling tests provide a direct method of determining the equivalent-circuit resistances and inductances. The tests allow for these parameters to be determined independently in contrast to the standard IEEE tests that require assumptions to be made in order to determine the parameters. A third approach known as the extended short-circuit test is also presented as an alternative characterisation method.

Experimental a 1.1 kW DFIM and a 30 kW DFIM utilising the various characterisation procedures is presented in the thesis. The various test methods are analysed and validated through comparison of model predictions and experimental results for torque-versus-speed curve for each induction machine. Sensitivity analysis is also used as a means of quantifying the effect of experimental error on the results from each of the testing procedures. This analysis is used to determine the suitability of the test procedures for characterising each of the devices.

The research then focuses on the OWC WEC and the modelling of this device. A software model is implemented based on data obtained from a scaled prototype device situated at the Irish test site. Test data from the electrical system of the device is analysed and this data is used to develop a performance curve for the air turbine utilised in the WEC. This performance curve was applied in a software model to represent the turbine in the electro-mechanical system and the software results are validated by the measured electrical output data from the actual scaled device.

Finally, once both the DFIM and OWC WEC power take-off system have been modelled succesfully, an investigation of the application of the DFIM to the OWC WEC model is carried out to determine the electrical machine rating required for the pulsating power derived from OWC WEC device. Thermal analysis of a 30 kW induction machine is carried out using a first-order thermal model. The simulations aim to quantify the limits of operation for the machine and give an insight into the rating requirements of an electrical generation system for the OWC WEC.

Acknowledgements

There have been many people who have contributed to the completion of this thesis. To try and thank everyone would be a long task, so I will mention a few.

Firstly, I would like to thank my academic advisors Dr. John Hayes and Dr. Michael Egan for their support, guidance and patience. Their enthusiasm and expertise provided a stimulating work environment that made the experience of the last number of years all the more enjoyable. I wish to express my appreciation to Dr. Dara O' Sullivan for his invaluable advice and support throughout the period of this work.

I would also like to thank collaborators of the work including the staff of the Hydraulics and Maritime Research Centre at UCC and Dr. Sinisa Djurovic and Dr. Sandy Smith of the University of Manchester. I would also like to express my appreciation to Sustainable Energy Ireland and the Irish Research Council for Science Engineering and Technology for co-funding the research.

I wish to thank the staff of the Department of Electrical and Electronic Engineering at University College Cork, thank you to Professor Patrick Murphy for allowing me access to the facilities of the department. Thank you to the staff at the Power Electronics Research Laboratory who provided invaluable advice and friendship. Among the many contributors are Dr. Ray Foley, James Griffiths, Dr. Richard Morrison, Daithí Power, John Slowey, Alex Kyriakopoulos, Dr. Brendan Lyons, Thomas Meade, Gerry McCarthy and Sharon Babbington. I would like to thank the Mechanical workshop staff, Mick O' Shea and Tim Power. Among the administrative staff I would like to thank Geraldine Mangan, Rita Sarteschi, Mary Costello and Ralf O' Flaherty.

I would also like to pay tribute to my fellow postgraduate students who provided great camaraderie and whom I shared many great times with. Particular mention must go to Dónal Murray, Eoin Thomas, James Curran, Jason Hannon, Kevin Hartnett, Marek Rylko, Naveen Boggarapu, Neil Hanley, Niamh O' Mahoney and Orla Doyle.

Finally, my sincere gratitude goes to my parents, Bernie and Billy, whose support, patience and encouragement knows no bounds. Also thanks to my brother and sister, Conor and Orla, for their understanding and support.

Associated Publications

- D. P. Cashman, J. G. Hayes, M. G. Egan, **Parameter characterisation of a doubly-fed induction machine using series-coupling and IEEE Std.112 test methods**, *Power Electronics Specialists Conference*, Rhodes, Greece, June 15-19, 2008, pp. 3836-3842.

- D. P. Cashman, J. G. Hayes, M. G. Egan, **Comparison of test methods for characterisation of a doubly-fed induction machine**, *Industry Applications Society Annual Meeting*, Edmonton, Alberta, Canada, October 5-9, 2008, pp 1-8.

- D. P. Cashman, D. L. O' Sullivan, M. G. Egan, J. G. Hayes, **Modelling and analysis of an offshore oscillating water column wave energy converter**, *8th European Wave and Tidal Energy Conference*, Uppsala, Sweden, September 7-10, 2009, pp 924-933.

- J. G. Hayes, D. P. Cashman, M. G. Egan, T. O'Donnell, N. Wang, **Comparison of test methods for characterization of high-leakage two-winding transformers**, *Industry Applications, IEEE Transactions on*, Vol. 45, No. 5, September/October 2009, pp 1729-1741.

- D. P. Cashman, J. G. Hayes, M. G. Egan, **Comparison of test methods for characterisation of doubly-fed induction machines**, *Industry Applications, IEEE Transactions on*, Vol. 46, No. 5, September/October 2010, *Paper currently in press*.

Contents

List of Figures

List of Tables

Nomenclature

a	acceleration (m.s^{-1})
A_a	annular area of Wells turbine (m^2)
A_c	chamber area (m^2)
B_m	machine friction factor (Nm.s)
B_r	damping ratio
B_t	damping coefficient (kg.rad.s^{-1} m^{-4})
C_{Th}	thermal capacitance (J^{o}C^{-1})
D	diameter of Wells turbine (m)
E_{elec}	electrical energy (J)
E_s	per-phase back-emf referred to stator frame (V)
f_{op}	rated operating frequency (Hz)
f_{red}	reduced applied frequency (Hz)
F_g	gravitational force (N)
F_j	inertial force (N)
F_n	Froude number
g	acceleration due to gravity (m.s^{-1})
G_c	per-phase core conductance (Mho)
$i_c(t)$	per-phase time varying core-loss current (A)
i_{cd}	per-phase d-axis core-loss current (A)

i_{cq} per-phase q-axis core-loss current (A)

$i_e(t)$ per-phase time varying excitation current (A)

$i_m(t)$ per-phase time varying magnetising current (A)

$i_r(t)$ per-phase time varying rotor current (A)

i_{rd} per-phase d-axis rotor current (A)

i_{rq} per-phase q-axis rotor current (A)

$i_s(t)$ per-phase time varying stator current (A)

i_{sd} per-phase d-axis stator current (A)

i_{sq} per-phase q-axis stator current (A)

I_a armature current (A)

I_{cum} per-phase cumulative current (A)

I_{dif} per-phase differential current (A)

I_{r-os} per-phase open-circuit stator current (A)

I_{s-or} per-phase open-circuit rotor current (A)

I_{LR} per-phase locked-rotor current (A)

I_{NL} per-phase no-load current (A)

J system inertia (kg.m^2)

k_t dc machine constant (V.s.rad^{-1})

l length (m)

L_{1-o2} open-circuit secondary inductance (mH)

L_{2-o1} open-circuit prmary inductance (mH)

L_{cum} per-phase cumulative inductance (mH)

L_{dif} per-phase differential inductance (mH)

L_{l1} primary leakage inductance (mH)

L_{l2} secondary leakage inductance (mH)

L'_{l2} secondary leakage inductance referred to the primary side (mH)

L_{lr} per-phase rotor leakage inductance (mH)

L'_{lr}	per-phase rotor leakage inductance referred to the stator frame (mH)
L_{ls}	per-phase stator leakage inductance (mH)
L_m	per-phase magnetising inductance for a series configuration (mH)
L_{mp}	per-phase magnetising inductance for a parallel configuration (mH)
L_r	per-phase rotor self inductance (mH)
L_{r-os}	per-phase open-circuit stator inductance (mH)
L_s	per-phase stator self inductance (mH)
L_{sc}	per-phase short-circuit secondary inductance (mH)
L_{s-or}	per-phase open-circuit rotor inductance (mH)
n	effective turns ratio
N	rotational speed (rad.s^{-1})
p	machine poles
p_c	Pressure head in the buoy chamber (Pa)
P_c	per-phase core-loss power (W)
P_{elec}	electrical power (W)
P_{eloss}	electrical power losses (W)
P_m	mechanical power (W)
P_{m-fl}	full-load mechanical power (W)
P_{mloss}	mechanical power losses (W)
P_{pneu}	pneumatic power (W)
P_{LR}	per-phase locked-rotor power (W)
P_{NL}	per-phase no-load power (W)
PF	power factor
Q	axial flowrate (m^3.s^{-1})
Q_c	cooling heat flow (W)
Q_{fl}	full-load reactive power (VAr)
Q_{LR}	per-phase locked-rotor reactive power (VAr)

Q_{NL} per-phase no-load reactive power (VAr)

Q_{Th} thermal heat flow (W)

R_1 primary resistance (Ω)

R_{1-o2} open-circuit secondary resistance (Ω)

R_2 secondary resistance (Ω)

R'_2 secondary resistance referred to the primary side (Ω)

R_{2-o1} open-circuit primary resistance (Ω)

R_a armature resistance (Ω)

R_c per-phase core-loss resistance for a series configuration (Ω)

R_{cp} per-phase core-loss resistance for a parallel configuration (Ω)

R_{cum} per-phase cumulative resistance (Ω)

R_{dif} per-phase differential resistance (Ω)

R_r per-phase rotor resistance (Ω)

R'_r per-phase rotor resistance referred to the stator frame (Ω)

R_{r-os} per-phase open-circuit stator resistance (Ω)

R_s per-phase stator resistance (Ω)

R_{sc} per-phase short-circuit primary resistance (Ω)

R_{s-or} per-phase open-circuit rotor resistance (Ω)

R_{Th} thermal resistance (^{o}CW^{-1})

s machine slip

S_{YX} sensitivity function of parameter *Y* to input variable *X*

t time (s)

T measured mechanical torque (Nm)

T_{em} electromagnetic torque (Nm)

T_f frictional torque (Nm)

T_j inertial torque (Nm)

T_m maximum mechanical torque (Nm)

T_{mech}	Mechanical torque (Nm)
T_{ND}	non-dimensional torque
u	velocity (m.s^{-1})
U_t	tip velocity (m.rad.s^{-1})
v_{cum}	per-phase time varying cumulative voltage (V)
v_{dif}	per-phase time varying differential voltage (V)
$v_r(t)$	per-phase time varying rotor voltage (V)
v_{rd}	per-phase d-axis rotor voltage (V)
v_{rq}	per-phase q-axis rotor voltage (V)
$v_s(t)$	per-phase time varying stator voltage (V)
v_{sd}	per-phase d-axis stator voltage (V)
v_{sq}	per-phase q-axis stator voltage (V)
V_a	armature voltage (V)
V_{boost}	voltage boost factor (V)
V_c	capacitor voltage (V)
V_{LR}	per-phase locked-rotor voltage (V)
V_{NL}	per-phase no-load voltage (V)
X_{cum}	per-phase cumulative reactance (Ω)
X_{dif}	per-phase differential reactance (Ω)
X_{lr}	per-phase rotor reactance (Ω)
X'_{lr}	per-phase rotor reactance referred to stator frame (Ω)
X_{ls}	per-phase stator reactance (Ω)
X_m	per-phase magnetising reactance (Ω)
X_{r-os}	per-phase open-circuit stator reactance (Ω)
X_{sc}	per-phase short-circuit reactance (Ω)
X_{s-or}	per-phase open-circuit rotor reactance (Ω)
Z_{1-o2}	open-circuit secondary impedance (Ω)

Z_{2-o1} open-circuit primary impedance (Ω)

Z_{cum} per-phase cumulative impedance (Ω)

Z_{dif} per-phase differential impedance (Ω)

Z_m per-phase magnetising impedance (Ω)

Z_r per-phase rotor impedance (Ω)

Z'_r per-phase rotor impedance referred to stator frame (Ω)

Z_{r-os} per-phase open-circuit stator impedance (Ω)

Z_s per-phase stator impedance (Ω)

Z_{sc} per-phase short-circuit impedance (Ω)

Z_{s-or} per-phase open-circuit rotor impedance (Ω)

Z_{th} Thevenin impedance (Ω)

θ temperature (^{o}C)

θ_{max} maximum temperature (^{o}C)

θ_{amb} ambient temperature (^{o}C)

Θ rotor position (^{o})

Θ_{cum} cumulative rotor position (^{o})

Θ_{dif} differential rotor position (^{o})

λ_{md} magnetising d-axis flux linkage (Wb)

λ_{mq} magnetising q-axis flux linkage (Wb)

λ_{rd} rotor d-axis flux linkage (Wb)

λ_{rq} rotor q-axis flux linkage (Wb)

λ_{sd} stator d-axis flux linkage (Wb)

λ_{sq} stator q-axis flux linkage (Wb)

μ Froude scaling factor

Π non-dimensional power coefficient

ρ_a air density (kg.m^{-3})

σ leakage coefficient

τ	thermal time constant (s)
ϕ	power factor angle (^{o})
ϕ_m	magnetising phase angle (^{o})
ϕ_s	stator phase angle (^{o})
Φ	flow coefficient
η	Efficiency
Ψ	non-dimensional pressure coefficient
ω_e	electrical frequency (rad.s^{-1})
ω_r	mechanical frequency (rad.s^{-1})
ω_{slip}	slip frequency (rad.s^{-1})
ω_{syn}	synchronous frequency (rad.s^{-1})

1

Thesis Introduction and Outline

1.1 Introduction

Global Concerns over secutity of energy supply and climate change are well documented reasons for the advancement of renewable energy technologies in recent times. Currently wind energy is at the foremost of the renewable energy developments for the majority of countries and has a worldwide installed capacity of 75 GW [1]. In Ireland the installed capacity of wind energy continues to grow with 921 MW currently installed and up to 1300 MW contracted to be connected in the coming years [2]. With the energy consumption of the world expected to rise considerably and a large number of countries committed to reducing carbon emissions, the development of other

forms of renewable energy will be important. Energy from the worlds oceans is estimated to have a potential of 8000-80000 TWh per annum for wave energy and 800 TWh per annum for tidal energy [3].

Wave energy is derived from winds as they blow across the ocean surface. The transfer of energy allows for highly concentrated energy to be stored in the water. Once waves are created they can travel very long distances without much loss of energy. One of the main processes by which energy in the waves is lost occurs as the waves approach the shoreline and interact with the sea bed. The energy flux in a wave is proportional to the wave period and the square of the wave amplitude [4].

The power density resources in the seas around Western Europe are estimated to be 33 kW/m in Southern regions such as Portugal ranging up to 75 kW/m off the coast of Scotland [5]. This makes the coastal Atlantic regions of Western Europe one of the richest areas in the world for wave power. A recent study estimated that the annual potential power off the coast of Ireland is in the region of 59 TWh [6].

The potential of energy extraction from such an abundant energy source has led to an increased interest in the development of a wave energy industry. Traditionally this industry has not received as much attention as other renewable sources such as wind and solar energy. This is largely because of the significant economic and technical challenges that exist for the development of wave energy systems when compared to other more established technologies. There are, for example, fundamental differences which exist between wave and wind energy generation. Some of these differences include the harsh and corrosive environment that exists at sea, a large ratio of peak to average loads exists and the first order oscillatory nature of sea waves in comparison to the wind.

Wave energy is currently in its infancy and is still very much in a research and development phase. It is therefore not yet economically competitive with other forms of renewable energy sources. Recently however, there have been major advancements in the field. This has largely been due to governmental support measures in research and development of wave energy technologies. Examples of pro-active European countries in this area are Portugal, Ireland, UK, Sweden,

Denmark and Norway [7].

The Irish government has commited to having 13.2% of its total electricity consumption to be derived from renewable sources by 2010 and to have 15-30% from renewable sources by 2020 [8]. This has led to a governmental strategy aiming at having fully commercial ocean energy devices connected to the National Grid by 2016.

To date successful testing of pre-commercial prototypes has been achieved by various developers. In other European states similar policies have been put in place and there have been several successful pre-commercial prototypes developed using a range of different technologies.

An outline of the main technologies being investigated for the extraction of wave energy is discussed in the following section.

1.2 Wave Energy Devices

Many wave energy conversion technologies presently exist with some of the more popular types including heaving body converters, over-topping devices, floating hinged devices and oscillating water column devices. A summary of the device types is discussed in [9]. Many of these devices have been developed to pre-commercial prototypes and the progress of a number of them is variously discussed in [10–12].

All of the devices rely on a multi-stage conversion process from energy in the sea to electrical energy known as the device power take off (PTO). The response of the PTO is usually controlled to optimise the power capture of the device from the incident wave power. In times of extreme sea conditions the device PTO is usually set to shed the excess incident wave power as part of the device protection. Each device type and its PTO are explained below.

Floating-hinge-type device

The floating-hinge-type device operates on the motion of parts of the body relative to each other due to passing waves. The most advanced device of this type is the device developed by Pelamis

Wave Power Ltd. [13]. Figure 1.1(a) shows the Pelamis device. The device consists of a set of semi-submerged cylinders linked together by a set of hinged joints. This device operates with a two-step PTO transmission process and utilises pumps and hydraulics in the process.

The primary transmission uses the relative motion between the cylinders to pump high-pressure hydraulic fluid into accumulators which provide short-term energy storage. In the secondary transmission process a hydraulic motor uses the smooth high-pressure fluid supplied by the accumulators to drive an electrical generator, [14]. Control is used to vary the impeding joint movement of the device in order to maximise the power capture from the sea waves.

Over-topping device

The over-topping WEC's PTO uses oncoming waves to fill a low-head reservoir. The potential energy in the water is then converted using a low-head hydro-turbine which is in turn connected to an electrical generator. Wave Dragon is the most well known type of over-topping device and is shown in Figure 1.1(b).

The device uses reflector arms to focus the incoming waves onto a ramp and once the water overcomes this ramp it fills a reservoir [11]. The ramp height for the device can be increased depending on the sea state and the levels of energy present in the sea at particular times. This device has the advantage of having inherent energy storage in the device structure.

The potential energy of the water inside the reservoir is exploited using a number of low-head turbines to convert the energy to mechanical form. These turbines are required to operate at a relatively wide range of water heads and also must be robust to avoid excessive maintenance.

The speed of rotation of the turbines is far less than the electrical grid frequency and therefore two options were considered in [11] for the electrical generator. A high pole-number permanent magnet machine is initially considered while a squirrel-cage induction machine and gearbox are also considered. The electrical generators are each supplied by back-to-back power electronic converters to control the rotational speed of the system.

Point absorber device

For point absorber devices the PTO uses the waves to excite motion of an upper body relative to a lower body to produce mechanical energy [12]. Examples of these devices are Wave Bob and Archimedes Wave Swing (AWS). Wave Bob is shown in Figure 1.1(c).

AWS is a device that is fixed to the sea-bed and has an internal air-pocket that expands and contracts with pressure differences above the device due to wave crests and troughs. This causes the movable outer component to move up and down relative to the fixed structure. The device can be controlled to increase the linear stroke motion of the device to maximise power capture.

(a) Floaing Hinged Device: Pelamis.

(b) Over-Topping Device: Wave Dragon.

(c) Floating Absorber Device: Wave Bob

(d) Oscillating Water Column Device: OE Buoy

Figure 1.1: Wave Energy Converter types

Wavebob is a semi-submerged floating device where an upper section of the device moves relative to a lower section due to the passing waves. This device can also be controlled to tune the natural frequency of the device to resonate with the sea condtions to maximise power capture.

The linear motion can be converted to electrical energy by using a direct drive linear generator.

These generators are unlike conventional rotary generators in their construction and operation but have gained increased attention in recent times [15–17].

Oscillating water column device

Of all the proposed technologies, the oscillating water column (OWC) is one of the most advanced [18]. The OWC WEC utilises a three step power take-off (PTO) conversion process. Energy in the sea is firstly converted to aerodynamic energy which is then transformed to mechanical energy via an air turbine. The mechanical energy is converted in turn to electrical power via a rotary electrical generator.

The OWC WEC operates on the principle of water in the column rising and falling as the waves in the sea interact with the device. Working shore-based protoypes have been developed in Scotland [19, 20] and Portugal [21]. However, there is now an emphasis on developing offshore devices as the potential for power extraction is much greater. In the case of the offshore OWC WEC the waves excite motion in the buoy type structure and the relative motion between the buoy and the sea causes the water column to rise and fall. The device investigated here is a backward-bent duct device (BBDD) OWC and as an example, the Ocean Energy Ltd. prototype device named the OE Buoy is shown in Figure 1.1(d). A diagram of the device and its operation is shown in Figure 1.2. It can be seen that in the case where the water level in the column rises, relative to the buoy, the air in the buoy chamber is pushed out to the atmosphere. This outflow of air is used to rotate the turbine to convert the pneumatic power to mechanical power. The aerodynamic and thermodynamic principles involved in this process are beyond the scope of this chapter but can be found in [22].

The alternative motion is when the water inside the column falls causing air from the atmosphere to be pulled into the resulting vacuum in the buoy chamber. This airflow can again be converted to mechanical form via a turbine. The inflow and outflow motion of the air occurs once per sea wave cycle and it is for this reason that the Wells turbine is well suited to the OWC application. The Wells turbine is a bi-directional device that rectifies the power from the reciprocating

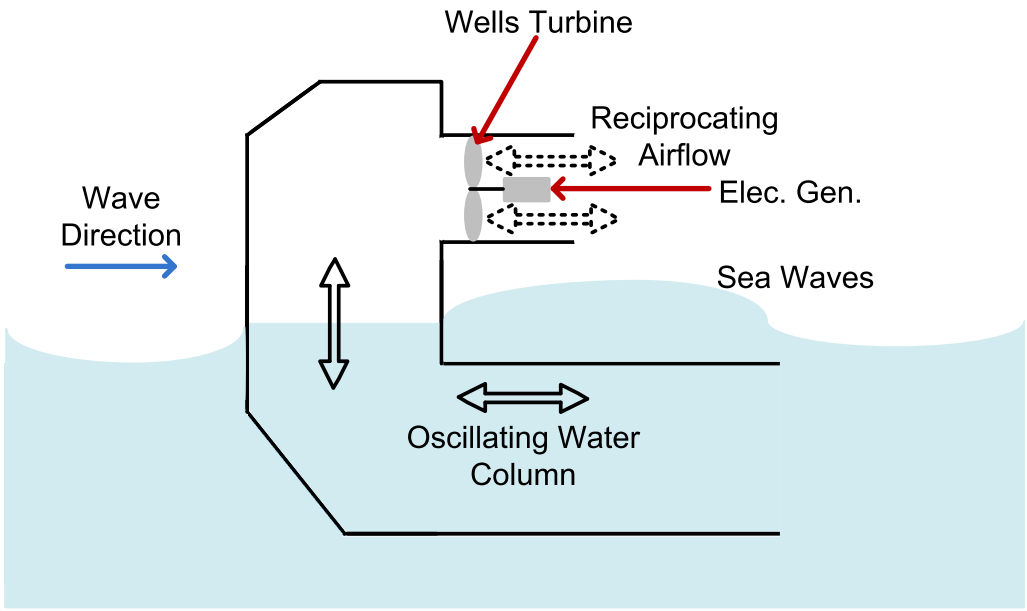

Figure 1.2: OWC operation

airflow. The turbine itself has no moving parts other than the rotor as its blades are generally fixed to the rotor structure making it attractive from a maintenance point of view. A drawback of the Wells turbine is that it has a narrow efficiency band meaning its aerodynamic performance drops off significantly outside a particular range of airflows.

The offshore OWC WEC is the device investigated in this thesis. The device employs the Wells turbine in its PTO and the operation of the device is analysed in further detail in later chapters.

1.3 Electrical Machines for Wind and Wave Applications

Wind Energy devices have been well established over the past number of decades. These devices use a horizontal axis three-bladed turbine which is connected via a gearbox to an electrical generator. In early turbines, direct drive asynchronous generators were connected to the grid. These turbines rotated at a fixed speed which was specified by the electrical grid frequency. Squirrel-cage induction generators (SCIG) were generally used in this topology.

A variable-speed design was preferred to the fixed-speed system as it allowed for a wider range of higher level system efficiency. The use of variable speed led to the doubly-fed induction generator (DFIG) becoming the industry standard generator. This type of generator was preferred to the standard squirrel-cage induction generator as the power electronic converter used only needs to be rated to handle the slip power which is typically only a fraction of the machine rating. Other advantages included the ability to operate above and below synchronous speed leading to sub- and super-synchronous modes of operation.

In [23] three induction generator topologies were investigated for a wind turbine application. A fixed speed SCIG system, variable-speed SCIG configuration and a variable-speed DFIG topology were considered. It was found that the variable-speed DFIG configuration provided the optimum solution as it provided the highest power capture over a range of wind speeds.

The doubly-fed induction machine is widely regarded as the optimum choice in wind turbine applications at present and is also used in other high power variable-speed ac drives [24]. The DFIM has also been considered in offshore wind farm projects [25, 26], although permanent-magnet ac (PMAC) machines are also popular for high power offshore wind turbines [27]. One of the disadvantages of the DFIG is that it is a brushed machine which makes it a significantly less desirable choice due to maintenance issues in offshore applications. Another disadvantage of the DFIG is that it suffers from fault ride-through issues.

In [27] the generation technology used in the ABB offshore wind turbines rated at 5 MW was presented. The system uses a synchrounous PMAC generator with a fully-rated back-to-back power electronic converter.

The popularity of the doubly-fed induction machine in wind turbine applications has led to it being considered as a generation topology for wave energy converters. The device is generally looked at in relation to rotary PTO devices such as the OWC WEC, [20, 21].

The fundamental difference between wind power generation and wave power generation exists in the profile of the power supplied to the device. In the case of wind energy there are variations in power around a mean value due to gusts in wind speed. Conversely, in the case of the pneumatic

power produced by the OWC WEC, the profile is oscillatory and varies between a maximum value to zero twice every wave cycle. This means that the peak-to-average ratio of power in the OWC WEC case is much higher than a wind application.

The optimum selection and rating of an electrical generator becomes a challenging problem for the design of the OWC WEC power take-off system. In [28] the investigation of different generator topologies for an offshore OWC WEC is presented. The generators investigated include the synchronous generator (SG), the squirrel-cage induction generator (SCIG), the doubly-fed induction generator (DFIG) and the permanent-magnet ac generator (PMAC).

In shore-based OWC devices a wound-rotor induction generator (WRIG) has been used, [19–21]. In [19] the WRIG is operated with an inverter-fed stator and a rotor configured with a variable external resistance. The rating of the machine was chosen conservatively and this caused a significant overrating of the machine with respect to the electrical power actually being handled.

This thesis aims to give an insight into the optimum induction machine rating for an offshore OWC WEC. In order to choose an optimum generator rating for the OWC WEC a key area of consideration is the thermal limitations of the machine. In this thesis the thermal rating of an electrical generator is investigated for an OWC application.

1.4 Thesis Objectives

This thesis focuses on the doubly-fed induction machine (DFIM) and the application of the machine to an OWC WEC device. In order to perform studies of the machine and OWC WEC it was vital to obtain accurate models of both the electrical machine and power conversion process in the OWC WEC.

The thesis initially considers the doubly-fed induction machine and the characterisation of the per-phase equivalent circuit parameters of the machine. As has been mentioned the DFIM is the most commonly used type of electrical generator in the wind industry and understanding the machines operation has become an important area of research. Precise knowledge of the

machines equivalent circuit parameters is essential in predicting the performance and operation of the machine.

The methods used for characterising the per-phase equivalent circuit parameters of the doubly-fed induction machine (DFIM) are investigated. IEEE standard 112 outlines the most established methods of determining the per-phase equivalent circuit of the DFIM and these tests are investigated initially.

The series-coupling tests are then presented as an alternative testing procedure to the IEEE method. These tests have been used in relation to high-leakage transformers and coupled inductors in the past with a high level of success, and the thesis aims to investigate the application of the series-coupling tests to the doubly-fed induction machine. The series-coupling tests produce three models for the device, namely the cumulative, differential and average models. These methods provide a more direct method of determining the equivalent circuit parameters of the DFIM, and thus provide an enhanced equivalent circuit model.

The thesis analyses and validates the results of each of the testing procedures through torque-versus-speed curve predictions and sensitivity analysis. By examining the characterisation procedures in this manner conclusions on the accuracy and suitability of each of the methods for characterising the DFIM can be drawn.

Once an accurate representation of the DFIMs equivalent circuit parameters was achieved the modelling of the OWC WEC was investigated. Modelling of the power take-off (PTO) for the OWC WEC is investigated in the thesis. The air turbine used in the mechanical conversion process is the focus of the research. The Wells turbine is the bi-directional air turbine employed, and a non-dimensional characteristic curve is developed to represent the turbine within the software model. The software model is developed based on experimental data from a prototype device situated at the Irish Test site. The model developed is a simplified first-order model of the Wells turbine. The aim of the research is to produce a software model that can be used in studies for the improvement of the electrical generation system used in OWC wave energy converters.

In this thesis the software model of the system is developed and validated through comparision

with experimental results. This validated OWC WEC model is then used with the doubly-fed induction machine model developed earlier in the thesis in simulations designed to study the thermal limitations of a 30 kW induction machine when it is employed with an OWC WEC. The OWC WEC model is scaled up using a method known as Froude scaling and the optimum device rating is matched to the thermal rating of the 30 kW machine. This study aims to give an insight into the thermal requirements and rating of an electrical generator for an OWC WEC.

Finally, conclusions on the outcome of the research is presented and future work that could be undertaken based on these results is discussed.

1.5 Thesis Outline

The outline of the thesis could be considered in three individual sections. The first section of the thesis contains Chapters 2 and 3 and focus on the accurate characterisation of the doubly-fed induction machine using various testing procedures. The second section, containing Chapter 4, concentrates on the modelling of the OWC WEC power-takeoff with particular focus on the Wells turbine. Validation of this model is carried outthrough comparision of simulations and experimental measurements. The third section of the thesis utilises the OWC WEC model from Chapter 4 with a 30 kW induction machine model to determine the optimum device rating for the specified machine. Simulations are carried out to perform thermal analysis of the machine to give a general insight into electrical machine rating for an OWC WEC device.

An outline of each of the thesis chapters is given as follows. This chapter gives background information on the current status of the wave energy industry with some of the most popular wave energy converter technologies discussed. An outline of the application of electrical machines in renewable generation systems is also presented.

Chapter 2 presents an overview of various methods that have been used to determine the equivalent circuit parameters of the DFIM. The chapter introduces and focuses on three testing procedures: IEEE Standard 112 tests, the series-coupling tests and the extended short-citcuit tests. The

theory behind these methods is presented in this chapter.

Chapter 3 describes the experimental testing of a high-leakage PWB transformer and two DFIMs. The use of standard testing procedures, the series-coupling tests and the extended short-citcuit tests to characterise the equivalent circuit parameters for the various devices are presented. The DFIMs are rated at 1.1 kW and 30 kW respectively. Both machines are tested using the IEEE, series-coupling and extended short-circuit approaches. An experimental torque versus speed curve for both machines is developed and the methodology used to obtain these curves is also given. Sensitivity analysis is used to further investigate the various characteristion procedures. This method is used to quantify the effect of measurement error on parameter prediction form each of the characterisation methods.

In Chapter 4 the OWC WEC is discussed in further detail and the development of a software model for the mechanical conversion within the device is discussed. Initially, the theory behind the Wells turbine operation is discussed in the chapter and this is then followed by the development of the software model. Experimental results from a scaled prototype device are used to develop a characteristic curve of the air turbine used within the device. Measured sea state data from the experimental prototype is then used to validate the results provided from the software simulations.

Chapter 5 uses a scaled version of the software model developed from the previous chapter to determine the electrical machine rating required for an OWC WEC device. Thermal analysis of a 30 kW induction machine is carried out using a first-order thermal model. The thermal analysis of the machine is used to quantify the limits of operation for the machine.

Finally, in Chapter 6 conclusions from the thesis are drawn and potential areas for future work are presented. The main outcomes from the thesis are discussed before possible areas of development are drawn up.

2

Induction Machine Characterisation Methods

2.1 Introduction

The characterisation of electrical equipment including transformers, electrical machines and power inductors is of vital importance in predicting the performance of these devices when employed in electrical systems.

Standard test approaches exist that can estimate parameters within a required level of accuracy. In the case of the two-winding transformer, standard open-circuit and short-circuit tests are used to solve for the six-element lumped-parameter equivalent circuit. Whilst these tests operate with a high level of accuracy for the majority of transformers, it has been found in recent studies that this

test approach does not provide the same level of accuracy for high leakage and lossy transformers [29].

High leakage transformers are widely used in many applications, notably resonant converters for dc-dc applications and seperable transformers for transcutaneous, marine and automotive inductive transfer [30, 31]. Leakages in such transformers tend to be large in relation to the magnetising inductance of the device making the standard open- and short-circuit testing procedures unsuitable [32].

Printed wiring board (PWB) integrated transformers and inductors are growing in popularity in the area of integrated power converters and other high frequency applications [33, 34]. In attemping to characterise this type of transformer difficulties are presented in the fact that the resistive and inductive elements are small relative to the interconnects used to test the devices.

For these reasons the development of a test approach that can determine the transformer elements in a more direct fashion than the standard two test approach has been investigated. In [35] the series-coupling test procedure is introduced and applied to high-leakage and integrated PWB transformers. It was seen that the results from these tests produced more accurate results than those obtained from the standard test approach. These loosely coupled transformers ranged in power from less than 1 W to greater than 100 kW and the leakage inductance as a percentage of open-circuit inductance was in the 1% to 5% range.

An extended-short-circuit test approach is also presented in [35]. This method uses the standard two-test approach in conjunction with a third test that allows for additional accuracy to be obtained when compared to the standard approach.

The doubly-fed induction machine (DFIM) is a machine commonly used in renewable energy applications. It differs from a conventional squirrel-cage induction machine (SCIM) as it has a wound rotor. This rotor configuration allows for its per-phase equivalent circuit to be represented in a manner that compares closely to the two-winding transformer. The DFIM also can contain a high level of leakage inductance and this can mainly be attributed to the large airgaps that exist in electrical machines of this type. High leakage machines can be desirable in wind generation as

higher leakages limit the short-circuit current in fault ride-through situations [36].

In general, standard dc, no-load and locked-rotor tests outlined in IEEE Standard 112 are used to characterise the DFIM [37]. Due to the resemblance of the DFIM equivalent circuit to a high-leakage transformer, the series-coupling tests have been investigated as a possible alternative to standard testing procedures for characterising the DFIM. The extended-short circuit test procedure is also presented as a method for characterising the DFIM.

Sensitivity analysis is a method presented in this thesis to compare the sensitivities of test methods to experimental measurement errors. This chapter outlines the theory behind the method and its application to the series-coupling tests.

This chapter reviews test methods that exist for the characterisation of induction machines. The IEEE Standard 112 testing procedures for characterising the DFIM are discussed in Section 2.3. The series-coupling tests are then presented as an alternative method for characterising the machine in Section 2.4. The extended-short-circuit test is used as a third approach for testing the machine and is presented in Section 2.6. Finally the theory behind the sensitivty analysis procedure is presented in Section 2.5.

2.2 Induction Machine Characterisation Methods Overview

As has been mentioned, the doubly-fed induction machine is a popular choice in the area of renewable energy generation systems. Characterisation of the machine's resistive and leakage elements can be especially important for optimising efficiency, functionality and determining the machine response under fault conditions. For example, control techniques such as field-oriented control and direct-torque control are found to be sensitive to parameter estimation errors [38]. Stankovic et al. have investigated the improved measurement of magnetizing inductance and discuss how it improves vector control performance [39]. The paper describes a method where a static dc test is carried out on the machine that provides a more direct measurement of the magnetising inductance. With the magnetising inductance determined, a no-load test was then used to independently

determine the stator leakage inductance.

The development of an accurate model can be used to aid winding-fault diagnostics in doubly-fed induction machines [40]. The aim of this paper was to monitor the condtion of the DFIM through investigating the harmonic content of the stator currents. In order to determine the harmonics that appear during particular fault conditions, the signals needed to be characterised so that a fault could be determined unambiguously. A time-stepped coupled-circuit model of the machines inductances was done to do aid this process.

Standard testing procedures in [37] are widely used to obtain the per-phase equivalent circuit model of the machine and these tests are presented in this chapter in Section 2.3.

In other texts, methods of characterisation have been presented with a view to improving the accuracy of induction machine characterisation.

In [41] a method involving fuzzy-control techniques to gain an improved squirrel-cage induction machine model is shown. The method uses a measured torque versus speed curve as a reference and uses a step-by-step fuzzy-control method to refine the parameters of the equivalent circuit until the predicted torque versus speed curve matches the reference curve.

Recursive least-squares methods are popular for increasing the accuracy of normal testing procedures and these methods are presented in [42–46]. In general, these methods require an 'initial guess' to begin calculating the equivalent circuit parameters. Thus, the accuracy of these methods is largely dependant on how good the initial estimate is. For this reason the IEEE standard tests are carried out to give the initial guess in [43]. In [44] a method that does not need an initial guess is provided but this method was found to suffer from errors due to un-modelled saturation effects, and extra steps had to be taken in order to overcome these problems.

Machine characterisation via finite element analysis (FEA) is also a popular approach. The literature shown in [47–50] discusses these methods of analysis. The FEA approach, as well as the least-squares methods, involve quite intensive and complex computational methods to determine the circuit parameters and, in the case of FEA, there is often a trade off between complex computations and the simplification of lumping parameters into a standard equivalent-circuit format.

A model that is developed using peak torque, frequency at peak torque and applied voltage at peak torque is discussed in [51]. This model uses a modified equivalent circuit that takes into account the coupling coefficient between the stator and the rotor. The model can be used for both rotary and linear induction generators.

Free acceleration and deceleration tests are carried out in [52] to obtain greater accuracy in the rotor parameters such as the rotor resistance and inductance. Another method used to improve the accuracy of the rotor parameters is the method carried out in [53] where a series of tests are carried out at different frequencies with the greatest accuracy determined by a single-phase test. Other models that involve injecting specialised signals to obtain machine models have been presented in [54, 55].

Induction machine models that are varied in order to take into account non-linear effects such as magnetic saturation are proposed in [56] and [57]. Both of these methods derived models that would perform better under saturation conditions than methods that determined circuit parameters by neglecting saturation effects. The model presented in [56] contains stator, rotor and magnetisation saturation effects. This model provides more accuracy in prediction of the machine performance in the saturation region. In [57] a π-model equivalent circuit is devloped that contains non-linear elements to account for saturation in the machine.

As has been mentioned sensitivity analysis methods can be used to compare the sensitivity of test methods to measurement error. This method has also been presented in [58] and [59] to determine the the effect of parameter uncertainty on the prediction of machine performance. The initial characterisation results are improved by adjusting the parameters using an adjustment factor that is determined based on the sensitivity analysis. In [60] sensitivity analysis is used to demonstrate the effect of circuit parameter errors on machine performance in a manner that allows for a model of the machine to be developed based on available manufacturer data.

A method involving the representation of a DFIM using a time stepped coupled-circuit method is shown in [40, 61]. This method allowed for higher order harmonics to be modelled for fault diagnostic purposes.

A wound rotor induction machine characterisation method is presented in [39]. This method requires that the neutral point of the rotor circuit be accessible. This puts a restriction on the test as the majority section of industrial wound-rotor induction machines do not readily allow for access to the neutral point of the rotor circuit.

The series-coupling test methods proposed in this chapter, provide a method of determining the equivalent circuit parameters of the induction machine without requiring computationally intensive methods that are common to those proposed in the FEA and least-squares approaches. They also provide additional and more accurate information on the circuit parameters than the standard IEEE tests.

2.3 IEEE Standard 112 Test Procedures

The IEEE Standard tests, [37], are well-established testing procedures for characterising both the squirrel-cage and the wound-rotor induction machines. The standard consists of four different methods that utilise no-load, locked-rotor and dc tests to determine the per-phase equivalent circuit of the machine. The standard equivalent circuit of the machine is given in Figure 2.1. This equivalent circuit is a T-model circuit with six lumped parameters, namely stator resistance, R_s, stator leakage inductance, L_{ls}, core-loss resistance, R_{cp}, magnetising inductance, L_{mp}, rotor resistance referred to the stator frame, R'_r and rotor inductance referred to the stator frame, L'_{lr}. The currents $i_s(t)$ and $i_r(t)$ are the stator and rotor currents respectively, $i_e(t)$ is the excitation current, $i_c(t)$ is the core-loss current and $i_m(t)$ is the magnetising current as outlined in [37].

Four methods exist in the IEEE standard 112 and any one of the four methods may be used to determine the machine parameters. Each method uses different procedures to calculate the parameters. The method to be used is generally based on the most practical option for a given situation. A brief description of the dc, no-load and locked rotor tests is given and this is followed by a description of each of the four methods used to determine the equivalent circuit of the induction machine.

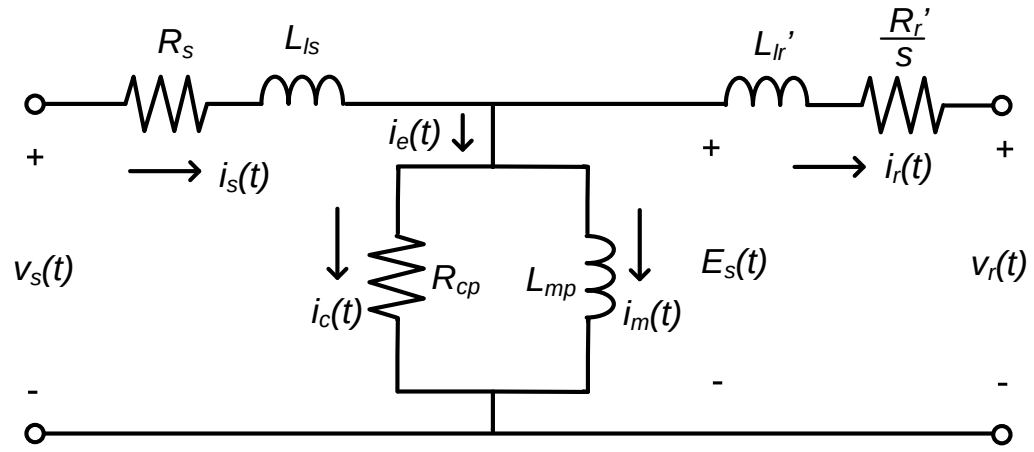

Figure 2.1: Per-phase equivalent circuit of the doubly-fed induction machine.

2.3.1 Dc, No-load and Locked-rotor tests

As has been noted, the IEEE standard methods are based on three experimental procedures which are the dc test, no-load test and locked-rotor test. The results from these procedures are then used to calculate the per-phase equivalent circuit. For all three tests, the rotor coils of the machine are shorted so that the machine resembles a squirrel-cage machine.

The dc test is initially carried out to determine a value for the stator resistance. A dc voltage is applied across two of the stator phases and the current drawn by the machine allows for the resistance to be obtained. The per-phase stator resistance is given as half of the measured quantity. The resistance values determined in this study do not account for the skin effect or effects due to temperature rise.

The no-load test is carried out by applying rated voltage and frequency to the machine when it operates without a mechanical load. The current, voltage and power factor are measured during the test. The losses measured in the no-load case consist of the stator resistive losses, friction and windage losses and core losses. The no-load losses also contain rotor copper losses however these losses are assumed negligible as the slip of the machine is close to zero meaning only a small rotor current exists.

The friction and windage losses can be determined by taking several readings at different voltage levels. The input power minus the stator resistance loss is plotted against the square of the applied voltage. This curve is then extrapolated to the zero voltage point. At this intercept the power is the friction and windage losses. This is depicted in Figure 2.2 where results from the 1.1 kW DFIM tested in Chapter 3 is shown. Measurements for the core, friction and windage losses are shown and a best fit line is plotted through this data. The line intercepts the y-axis at 56.27 W and this value corresponds to the no-load friction and windage losses.

The core-loss can then be determined by subtracting the stator losses and friction and windage losses from the input power.

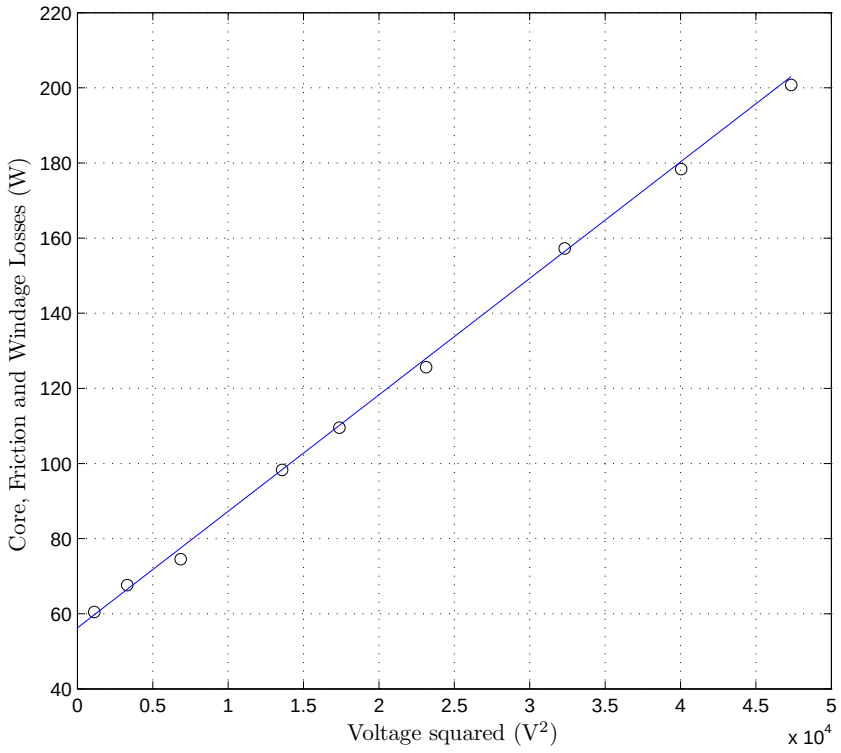

Figure 2.2: Core, Friction and Windage losses versus applied voltage squared

In the case of the locked-rotor test the machines rotor is locked down so that it cannot rotate. For wound-rotor machines the impedance of the rotor circuit is seen to vary with rotor position.

This is due to the brushed contacts that exist in this type of machine. Therefore, in order to avoid misrepresentation of the rotor impedance the voltage, current and power factor are measured over several locked-rotor positions for the machine. The position that gives the average between maximum impedance and minimum impedance is used for the test. The applied voltage is adjusted so that the rated current is drawn by the machine. The losses observed in the machine consist of stator and rotor losses in the locked-rotor case.

Once data for each of the three methods is obtained one of the following calculation methods can be used to determine the per-phase equivalent circuit parameters.

2.3.2 IEEE Standard Test Method 1

IEEE Method 1 is the method primarily used to characterise the induction machine and utilises a locked-rotor test at rated current with the dc and no-load tests. This section describes the calculation process required to determine the per-phase equivalent circuit parameters.

Initially, an assumption on the stator and rotor leakage reactances must be made. The standard states that these reactances are equal for wound-rotor induction machines. Taking this assumption and also making an initial assumption for the ratio of the stator inductance to the magnetising inductance allows for the calculation process to begin.

By using the no-load test results the reactive power can be determined by the following equation:

$$Q_{NL} = \sqrt{(3V_{NL}I_{NL})^2 - (P_{NL})^2} \tag{2.1}$$

where V, I and P are the measured voltage, current and power test values, respectively.

The magnetising reactance X_m is calculated using the following expression with an initial value assumed for the stator leakage reactance as well as a ratio between stator leakage reactance and magnetising reactance also assumed.

$$X_m = \frac{3V_{NL}^2}{Q_{NL}^2 - 3I_{NL}^2 X_{ls}} \frac{1}{\left(1 + \frac{X_{ls}}{X_m}\right)^2} \tag{2.2}$$

where V_{NL}, I_{NL} are the no-load voltage and current respectively, Q_{NL} is the no-load reactive power determined from (2.1), X_{ls} is the stator leakage reactance and $\frac{X_{ls}}{X_m}$ is the assumed relationship between the magnetisng and stator reactances.

The stator leakage reactance can be calculated by using the following equation and using the same assumed ratio between X_{ls} and X_m as above.

$$X_{ls} = \frac{Q_{LR}}{3I_{LR}^2 (1 + \frac{X_{ls}}{X'_{lr}} + \frac{X_{ls}}{X_m})} \left(\frac{X_{ls}}{X'_{lr}} + \frac{X_{ls}}{X_m}\right) \tag{2.3}$$

where I_{LR} is the locked-rotor current, Q_{LR} is the locked-rotor reactive power determined from (2.1) and $\frac{X_{ls}}{X'_{lr}}$ is the assumed ratio between the stator and rotor leakage reactances.

Once the magnetising and stator leakage reactances have been determined the ratio $\frac{X_{ls}}{X_m}$ can be re-calculated and substituted back into the two reactance equations (2.2) and (2.3). The parameters can be re-calculated using the revised reactance ratio and an iterative process should be carried out until the desired accuracy is obtained. In this study five iterations were carried out.

Once the desired accuracy for X_{ls} and X_m have been obtained the rotor leakage inductance, X'_{lr}, can be determined using:

$$X'_{lr} = \frac{X_{ls}}{\frac{X_{ls}}{X'_{lr}}} \tag{2.4}$$

The core conductance G_c and core resistance R_c can be calculated using the following expressions:

$$G_c = \frac{P_c}{3V_{NL}^2} \left(1 + \frac{X_{ls}}{X_m}\right)^2 \tag{2.5}$$

$$R_c = \frac{1}{G_c} \tag{2.6}$$

where P_c is the core-loss power determined from the no-load test by taking the per-phase input power absorbed and accounting for the stator losses and the frictional losses.

The final parameter that is to be calculated is the per-phase reflected rotor resistance R'_r and this is given by the following equation:

$$R'_r = \left(\frac{P_{LR}}{3I_{LR}^2} - R_s\right)\left(1 + \frac{X'_{lr}}{X_m}\right)^2 - X_{ls}^2 G_c \left(\frac{X'_{lr}}{X_{ls}}\right)^2 \tag{2.7}$$

Thus, all elements of the per-phase equivalent T-model of the wound-rotor induction machine have been determined using IEEE Method 1. Method 1 is generally the most convenient of the test methods and is used most often to determine the per-phase equivalent circuit. This is because Method 1 uses the dc, no-load and locked-rotor tests which are usually the most convenient tests to be carried out. The other IEEE methods presented utilise extra or alternative methods that may not be as realisable as the tests used in Method 1.

2.3.3 IEEE Standard Test Method 2

IEEE Method 2 is used to characterise the machine when the device is to be operated at a reduced operating frequency. The method involves performing the locked-rotor test at three different frequencies, one at rated frequency, one at 50% of rated frequency and one at 25% of rated frequency.

This calculation procedure is carried out by following the same steps as outlined in Method 1. The rotor resistance R'_r and total leakage inductances X_{ls} + X'_{lr} are calculated for three different test frequencies. Curves are then developed for rotor resistance and the total inductance of the machine over the range of frequencies, and from these curves the parameters can be determined for the specified operating frequency. The values for inductance and resistance can be rated to the

operating frequency by the following relationship:

$$X'_{lr} = \frac{f_{red}}{f_{op}} X'_{lr-fr} \tag{2.8}$$

where f_{red} is the reduced operating frequency, f_{op} is the rated operating frequency and X'_{lr-fr} is the rotor leakage reactance for the reduced frequency. This procedure can be used for the stator leakage reactance and the rotor resistance.

IEEE Method 2 is therefore a useful method for applications where the machine will be operating below rated frequency. If the machine is to operate at rated frequency, IEEE Method 2 is not required to determine the equivalent circuit parameters.

2.3.4 IEEE Standard Test Method 3

Method 3 offers an alternative method to the procedure introduced in Method 1. The procedure involves a test at a reduced frequency and voltage that gives the desired slip speed for the machine. Method 3 is therefore useful for applications where a locked-rotor test is not practical. The reduced frequency test is used with the no-load and dc tests discussed earlier.

The values obtained from the no-load test are used to obtain a plot of reactance versus applied voltage. This reactance is given as the sum of the magnetising reactance X_m and the stator leakage reactance X_{ls}. The highest point on the curve is used in this test for the sum of the two reactances. This is plot of reactance variation is shown for the 1.1 kW DFIM in Figure 2.3. Point A on the graph shows the highest point on the curve and it is this point that is used in the calculation process.

Using the data from the reduced frequency and voltage test, the stator phase angle ϕ_s, the total apparent resistance per phase R and the total apparent reactance per phase X are determined by the following equations.

$$\phi_s = cos^{-1} PF \tag{2.9}$$

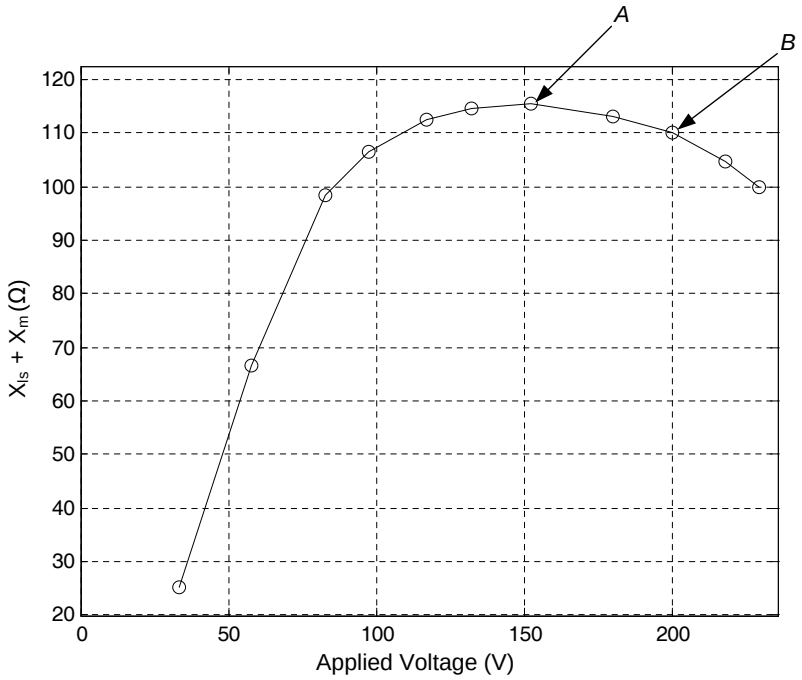

Figure 2.3: Variation of reactance versus applied voltage for the no-load test

$$R = Z\,cos(-\phi_s) \tag{2.10}$$

$$X = Z\,sin(-\phi_s) \tag{2.11}$$

where Z is the apparent impedance.

The value determined for X is used as an initial estimate for the sum of the stator and rotor leakage reactances. By making an initial assumption of the stator leakage reactance value as well as the ratio between stator and rotor leakage reactances then the following equation can be used to determine the stator leakage reactance.

$$X_{ls} = X\frac{\frac{X_{ls}}{X'_{lr}}}{1+\frac{X_{ls}}{X'_{lr}}} \tag{2.12}$$

Using the total reactance value $X_m + X_{ls}$ obtained from Figure 2.3 the magnetising reactance

can be determined from the following expression.

$$X_m = (X_{ls} + X_m) - X_{ls} \tag{2.13}$$

The voltage across the magnetising branch referred to the stator E_s can be calculated using the data obtained from the slip test. The stator resistance R_s, measured from the dc test, is also used:

$$E_s = \sqrt{(V_s - I_s(R_s cos\phi_s - X_{ls} sin\phi_s))^2 + (I_s(R_s sin\phi_s + X_{ls} cos\phi_s))^2} \tag{2.14}$$

Similarly, the phase angle ϕ_m can be calculated using the following equation:

$$\phi_m = tan^{-1}\left(\frac{-I_s(R_s sin\phi_s - X_{ls} cos\phi_s)}{V_s - I_s(R_s cos\phi_s - X_{ls} sin\phi_s)}\right) \tag{2.15}$$

Using the magnetising reactance determined from (2.13) and the magnetising branch voltage determined from (2.14) the magnetising current I_m can be calculated using the following equation.

$$I_m = \frac{E_s}{X_m} \tag{2.16}$$

The core resistance R_c is found by using the core-loss power P_c from the no-load test and the magnetising branch voltage:

$$R_c = 3\frac{E_s^2}{P_c} \tag{2.17}$$

Using the core resistance and the magnetising branch voltage allows for the core-loss current to be determined from the following equation:

$$I_c = \frac{E_s}{R_c} \tag{2.18}$$

The calculated results for stator phase angle ϕ_s, magnetising phase angle ϕ_m, magnetising current

I_m and core-loss current I_c can be used with the measured stator current I_s to determine the rotor current I_r from the following expression.

$$I_r = \sqrt{(I_s cos\phi_s - I_m sin\phi_m - I_c cos\phi_m)^2 + (-I_s sin\phi_s + I_m cos\phi_m + I_c sin\phi_m)^2} \quad (2.19)$$

The reflected rotor leakage reactance X'_{lr} can be determined using the following expression:

$$X'_{lr} = \frac{-V_s I_s sin\phi_s - I_s^2 X_{ls} - I_m^2 X_m}{I_r^2} \quad (2.20)$$

Using the value of X_{ls} from (2.12) with X'_{lr} from (2.20) a revised value of apparent reactance X can be determined.

$$X = X_{ls} + X'_{lr} \quad (2.21)$$

This value of X can be used in the next iteration of the data by re-using equations (2.12)-(2.21). Similar to the previous methods five iterations were used in this process. Once the desired accuracy has been found, the following equations are used to determine rotor resistance.

$$Z'_r = \frac{E_s}{I_r} \quad (2.22)$$

$$R'_r = s\sqrt{Z'^2_r - X'^2_{lr}} \quad (2.23)$$

where s is the machine slip and Z'_r is the rotor impedance.

Figure 2.3 is again referred to and point B which corresponds to the reactance at rated voltage is to be used in place of the previous value for the following calculations.

$$X_m = (X_{ls} + X_m) - X_{ls} \quad (2.24)$$

$$E_s = \sqrt{(V_s - I_s(R_s cos\phi_s + X_{ls} sin\phi_s))^2 + (I_s(R_s sin\phi_s + X_{ls} cos\phi_s))^2} \quad (2.25)$$

$$G_c = \frac{P_c}{3V_r^2} \quad (2.26)$$

G_c is the core conductance and the core resistance R_c can be determined by using (2.6).

The solutions from equations (2.12), (2.20), (2.23), (2.24) and (2.6) are used to determine the per-phase equivalent circuit parameters X_{ls}, X'_{lr}, R_r, X_m and R_c, respectively. The results from the dc test are used to determine the stator resistance R_s.

2.3.5 IEEE Standard Test Method 4

This method is used when the previous three methods are not practical. The method utilises the no-load and locked rotor tests as well as the reduced voltage slip test from the previous method. The slip test is carried out at the rated slip for the machine. The rotor and stator leakage reactances as well as the magnetising reactance and core-loss resistance are determined using the same procedure as was presented in Method 1. The rotor resistance is calculated by the utilising the calculation procedure of Method 3. By calculating E_s, ϕ_m, I_m, I_c, I_r and Z_r using the equations presented in Method 3 the rotor resistance can be found. The process is again iterated five times in this study to obtain the equivalent circuit parameters at the desired accuracy.

2.4 Series-Coupling Tests

As has been mentioned there are similarities between the DFIM equivalent circuit and that of a classical two-winding transformer. The DFIM has the advantage of having access to the rotor windings which allows for the comparison with the two-winding transformer. This is in contrast with the squirrel-cage induction machine where the rotor is inaccessible.

If the induction machine is modelled as a transformer and the equivalent circuit is represented as a transformer equivalent circuit, then transformer-type characterisation tests can be carried out

on the machine, assuming the effective turns ratio is known. The effective turns ratio, n, is a function of turns per coil, pitch factor and distribution factor of the machine [62]. The series-coupling test procedure involves using a model of the induction machine shown in Figure 2.4 where the magnetising branch in Figure 2.4 is represented as a series branch. The transformation from a parallel to series branch is outlined in [35]. The following equations are used to transform the parallel elements into an equivalent series form.

$$R_c = \frac{R_{cp}\omega_e^2 L_{mp}^2}{R_{cp}^2 + \omega_e^2 L_{mp}^2} \tag{2.27}$$

$$L_m = \frac{R_{cp}^2 L_{mp}}{R_{cp}^2 + \omega_e^2 L_{mp}^2} \tag{2.28}$$

where R_{cp} is the parallel branch core-loss resistance and L_{mp} is the parallel branch magnetising inductance. The sinusoidal excitation frequency is denoted ω_e.

The inverse transformations from series elements to parallel elements are given by the following expressions.

$$R_{cp} = \frac{R_{cp}^2 + \omega_e^2 L_{mp}^2}{R_{cp}} \tag{2.29}$$

$$L_m = \frac{R_{cp}^2 + \omega_e^2 L_{mp}^2}{\omega_e^2 L_{mp}} \tag{2.30}$$

The derivation of the parallel to series branch transformation and the corresponding inverse transformation are shown in Appendix A.

It should be noted that the equivalent circuit in Figure 2.4 assumes that the machine is static and therefore the machine slip is assumed to be 1. All tests used in the series-coupling testing procedure are carried out with the machines rotor locked down.

The series-coupling test procedures include the open-circuit tests and the differential and cu-

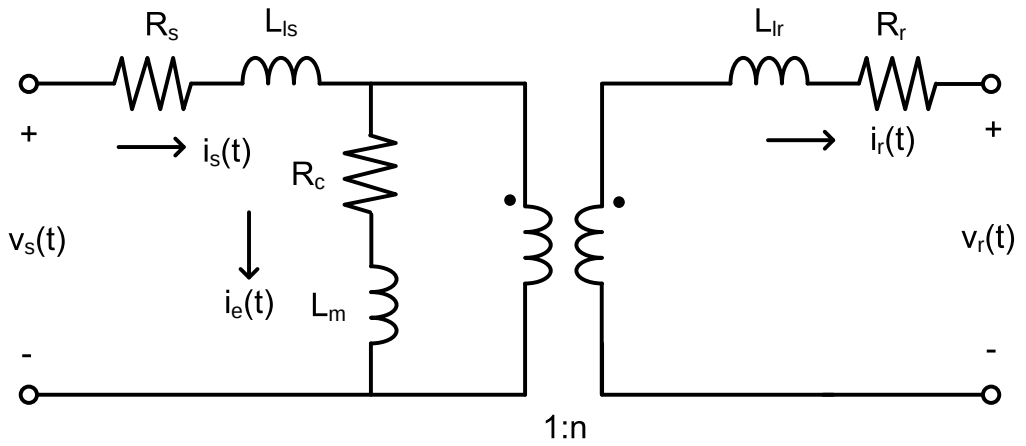

Figure 2.4: Transformer-type representation of the per-phase equivalent circuit of the doubly fed induction machine.

mulative tests. All of these tests are static tests and therefore the rotor of the DFIM must be locked down. An outline of these tests are given in the following sections.

2.4.1 Open-circuit tests

There are two open-circuit tests that are to be carried out on the machine: the open-circuit rotor (OR) test and the open-circuit stator (OS) test. These tests compare with the standard open-primary and open-secondary tests on a two-winding transformer.

By analysing Figure 2.4 and considering the stator back emf equation, it can be seen that the following expression can be developed:

$$v_s(t) = R_s i_s(t) + L_{ls}\frac{di_s(t)}{dt} + R_c i_e(t) + L_m\frac{di_e(t)}{dt} \tag{2.31}$$

The excitation current, $i_e(t)$, can be expressed in terms of stator current, $i_s(t)$, and rotor current $i_r(t)$ by the following equation:

$$i_e(t) = i_s(t) - n\, i_r(t) \tag{2.32}$$

Rearranging (2.31) by substituting (2.32) in for the excitation current gives the following equation:

$$v_s(t) = (R_s + R_c)i_s(t) - n\,R_c i_r(t) + (L_{ls} + L_m)\frac{di_s(t)}{dt} - n\,L_m\frac{di_r(t)}{dt} \tag{2.33}$$

A similar expression can be derived for the applied per-phase rotor voltage:

$$v_r(t) = -(R_r + n^2 R_c)i_r(t) + n\,R_c i_s(t) - (L_{lr} + n^2 L_m)\frac{di_r(t)}{dt} + n\,L_m\frac{di_s(t)}{dt} \tag{2.34}$$

These equations assume that the machine is connected in the star-star configuration.

These two tests alone are not sufficient to characterise the induction machine. In order to do this, these tests should be used in conjunction with the series-coupling tests or with the short-circuit tests. The former will be discussed in the next section with the latter used as a further technique in a later section.

2.4.2 Differential and Cumulative Tests

The series-coupling tests involve electrically connecting the stator (primary) coil to the rotor (secondary) coil, as is shown in Figure 2.5. This allows for two different measurement set-ups to be achieved. The first is the cumulative (series-aiding) test and the second is the differential (series-opposing) test. The cumulative test occurs when the poles of the machine align to give an algebraic summing of the machine fluxes that corresponds to a maximum inductive point. This condition will occur naturally if a voltage is applied and the rotor is free to move. For the differential test to be achieved the poles of the machine must be aligned in a fashion that the algebraic summing of the machine fluxes corresponds to a minimum inductive point. For a p-pole pair machine there will be p maximum and p minimum inductive points. Thus the differential point is displaced from the cumulative point by the following equation:

$$\Theta_{dif} = \Theta_{cum} \pm \frac{360^o}{2p} \tag{2.35}$$

where Θ_{dif} is the differential rotor position and in Θ_{cum} is the cumulative rotor position in degrees.

A 2-pole pair machine will therefore have two maximum and two minimum inductive points. By locking the rotor ninety degrees from the maximum inductive point then the minimum inductive point, or the differential point can be found. Data that was recorded on the 1.1 kW test machine to be discussed in Chapter 3 is shown in Figure 2.6 and it demonstrates the inductance variation over a range of rotor positions. The sinusoidal distribution of the flux can be seen in Figure 2.6

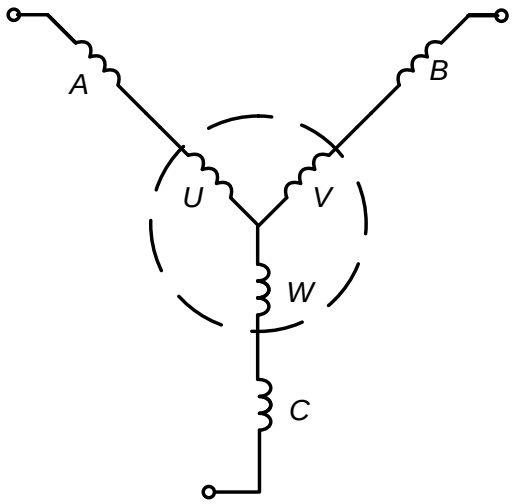

Figure 2.5: Series-coupling connections.

and the positions that the rotor must be locked at in order to achieve the maximum and minimum inductive points can also be seen. The cumulative point is seen to occur at approximately 20^{o} and the differential point is at approximately 110^{o}. The cumulative and differential tests must then be carried out at these points. When the DFIM is connected in the series-coupling configuration and locked at the differential point then it can be represented by the per-phase equivalent circuit shown in Figure 2.7(a), [32]. This is analagous to connecting the primary coils directly to the secondary coils of a transformer. It can be seen in Figure 2.7(a) that the negative terminal of the primary connects to the negative terminal of the secondary. This means that in this configuration

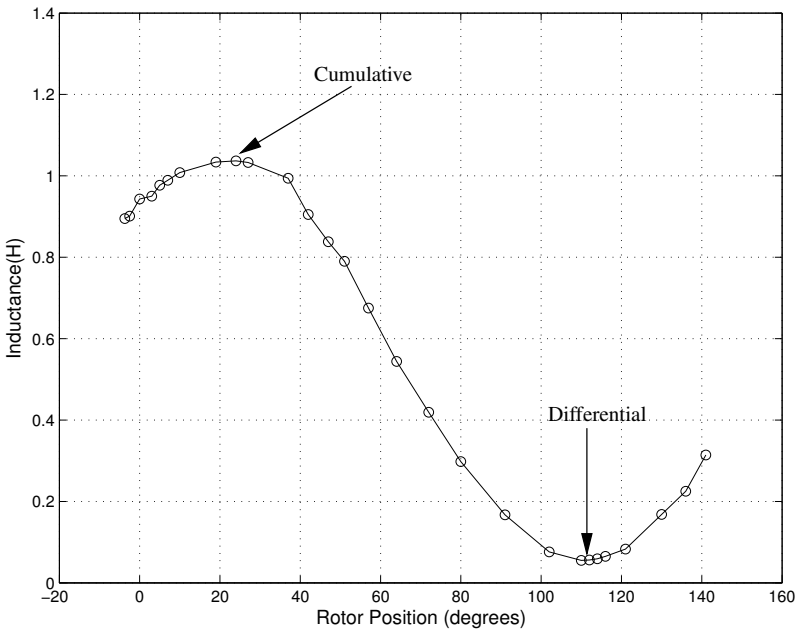

Figure 2.6: Plot of inductance variation with rotor position for 4-pole DFIM.

a common current flows in the stator and the rotor giving:

$$i_{dif}(t) = i_s(t) = i_r(t) \tag{2.36}$$

It can be seen that the voltage applied to the machine in this configuration is given by the following expression:

$$v_{dif}(t) = v_s(t) - v_r(t) \tag{2.37}$$

Equations (2.33), (2.34) and (2.36) can be substituted into (2.40) to develop the differential voltage equation.

$$v_{dif}(t) = \left[R_s + R_r + (1-n)^2 R_c\right] i_{dif}(t) + \left[L_{ls} + L_{lr} + (1-n)^2 L_m\right] \frac{di_{dif}(t)}{dt} \tag{2.38}$$

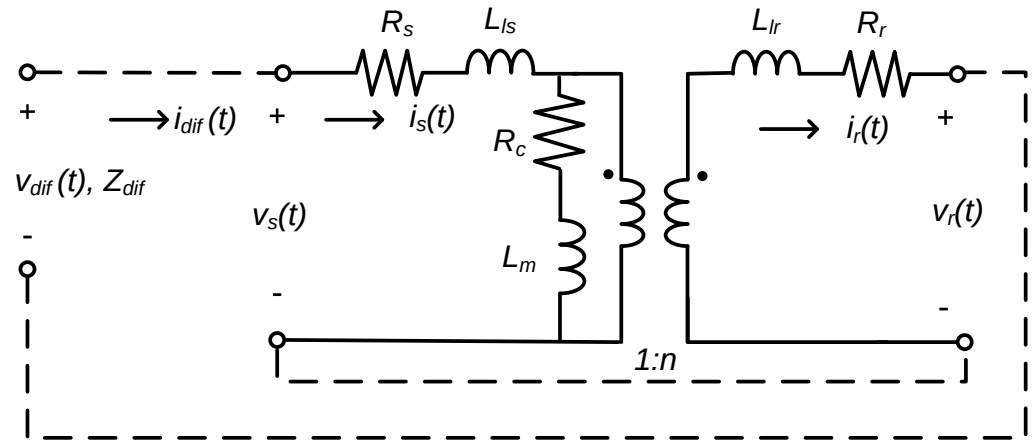

(a) Differential coupling equivalent circuit.

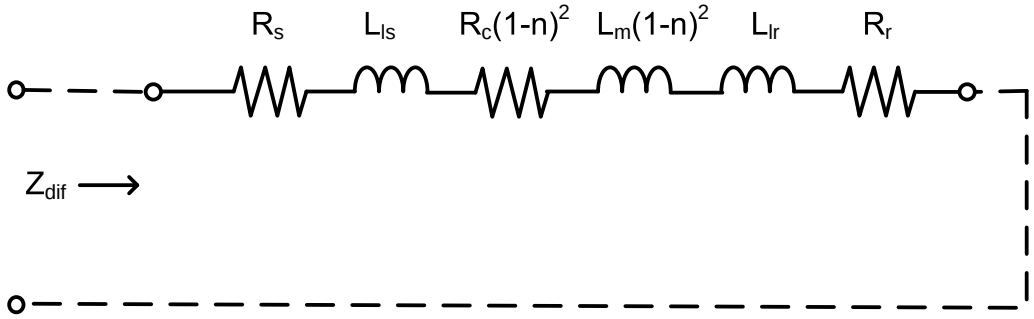

(b) Simplified differential coupling equivalent circuit impedance.

Figure 2.7: Transformer type equivalent circuit for differential-coupling of DFIM.

From the above equation the differential impedance is given by:

$$Z_{dif} = [R_s + R_r + (1-n)^2 R_c] + j\omega_e[L_{ls} + L_{lr} + (1-n)^2 L_m] \tag{2.39}$$

This impedance is illustrated schematically in the simplified differential coupled equivalent circuit shown in Figure 2.7(b).

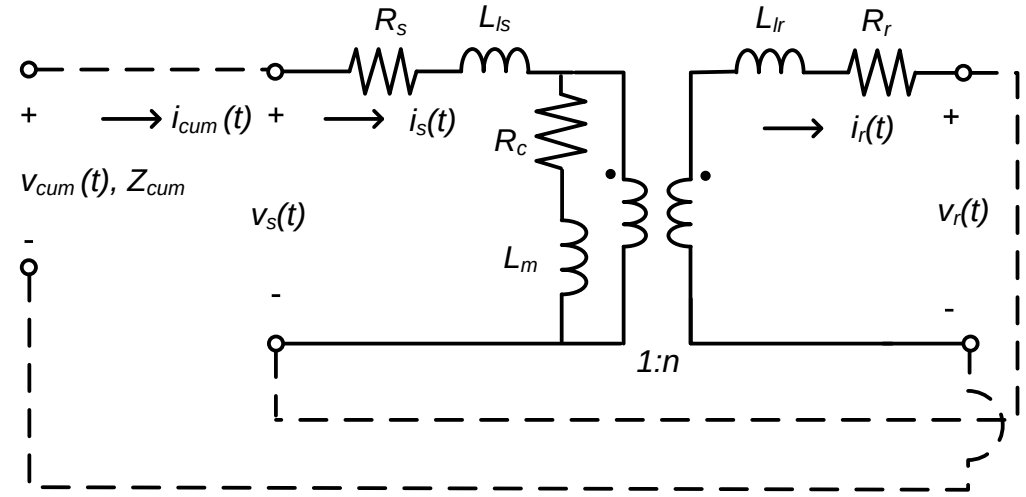

(a) Cumulative coupling equivalent circuit.

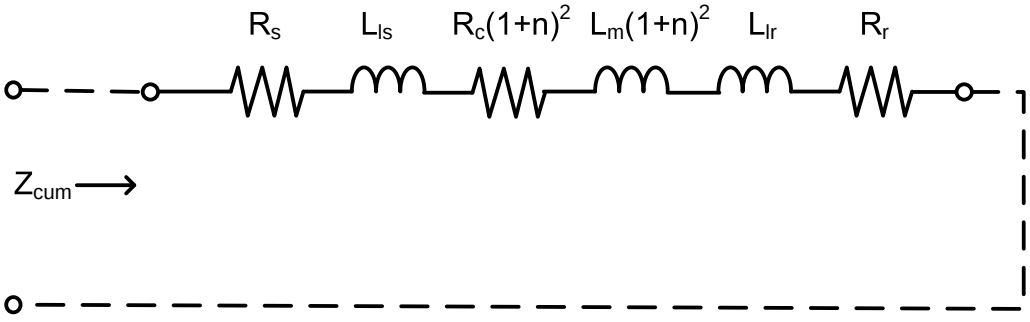

(b) Simplified cumulative coupling equivalent impedance.

Figure 2.8: Transformer type equivalent circuit for cumulative-coupling of DFIM.

In the case of a 2-pole pair machine the rotor must be locked at a position that is displaced ninety degrees from the differential point for the cumulative coupling test to be achieved. Using the transformer equivalent circuit analogy, locking the rotor in this position is equivalent to swapping

the secondary connections of a differentially connected transformer. This means that the negative terminal of the primary is connected to the positive terminal of the secondary, as is shown in Figure 2.8. For the cumulative coupling set up the voltage and current in the machine are given by the following equations.

$$v_{cum}(t) = v_s(t) + v_r(t) \tag{2.40}$$

$$i_{cum}(t) = i_s(t) = -i_r(t) \tag{2.41}$$

Using a similar analysis on the cumulative coupling equivalent circuit the voltage can be seen to be given by the following expression:

$$v_{cum}(t) = \left[R_s + R_r + (1+n)^2 R_c\right] i_{cum}(t) + \left[L_{ls} + L_{lr} + (1+n)^2 L_m\right] \frac{di_{cum}(t)}{dt} \tag{2.42}$$

If the same procedure is carried out for the cumulative test then it can be found that the cumulative impedance is given by:

$$Z_{cum} = [R_s + R_r + (1+n)^2 R_c] + j\omega_e [L_{ls} + L_{lr} + (1+n)^2 L_m] \tag{2.43}$$

It can be seen from the impedance equations (2.43) and (2.39), for the cumulative and differential tests that the resistances and inductances seen are the algebraic sum of the machines resistances and inductances and it is this property that allows for the direct measurement of the machine parameters.

2.4.3 Determining equivalent circuit parameters

By using the expressions for the impedances developed from the series-coupling tests with the impedances obtained from the open-circuit tests, the per-phase equivalent circuit parameters can be determined. This is achieved by obtaining eight equations from the open-circuit and series-

Table 2.1: Equations obtained from series coupling tests.

Test	Resistance	Inductance	Current
OR	$R_{s-or} = R_s + R_c$	$L_{s-or} = L_s + L_m$	I
OS	$R_{r-os} = R_r + R_c n^2$	$L_{r-os} = L_r + L_m n^2$	$\frac{I}{n}$
Dif	$R_{dif} = R_s + R_r + R_c(1-n)^2$	$L_{dif} = L_s + L_r + L_m(1-n)^2$	$\frac{I}{1-n}$
Cum	$R_{cum} = R_s + R_r + R_c(1+n)^2$	$L_{cum} = L_s + L_r + L_m(1+n)^2$	$\frac{I}{1+n}$

coupling tests to find six unknown parameters. Table 2.1 summarises the equations obtained from the tests. R_{s-or} is the measured stator resistance with the rotor circuit open, R_{r-os} is the measured rotor resistance with the stator circuit open, R_{dif} is the differential resistance and R_{cum} is the cumulative resistance. The inductances in the table are labelled in a similar fashion. I is the applied test current and n is the effective turns ratio.

The core-loss resistance and magnetising inductance parameters are non-linear elements that vary with different levels of flux in the core. In order to ensure these results are consistent the magnetising flux levels in the machine must remain constant throughout the testing. The applied current in each test must therefore be set to specific values and thus the following equalities must be held for the applied currents:

$$I_{s-or} = I_{r-os} n = I_{dif}(1-n) = I_{cum}(1+n) \tag{2.44}$$

Applying these conditions will ensure that a constant core-loss resistance and a constant magnetising inductance are attained. The required current levels for each test are shown in the final column of Table 2.1.

Thus using the resistance and inductance equations in Table 2.1 two equivalent circuit models

Table 2.2: Equations for core-loss resistances and magnetising inductances.

Test	Resistance	Inductance
Dif	$R_c = \frac{R_{s-or} + R_{r-os} - R_{dif}}{2n}$	$L_m = \frac{L_{s-or} + L_{r-os} - L_{dif}}{2n}$
Cum	$R_c = \frac{R_{cum} - R_{s-or} - R_{r-os}}{2n}$	$L_m = \frac{L_{cum} - L_{s-or} - L_{r-os}}{2n}$
Avg	$R_c = \frac{R_{cum} - R_{dif}}{4n}$	$L_m = \frac{L_{cum} - L_{dif}}{4n}$

can be obtained. The first model uses the open-circuit impedances in the first two rows of Table 2.1 with the differential test impedances and the second method uses the cumulative impedances in place of the differential impedances.

Table 2.2 shows the core-loss resistance and the magnetising inductance equations determined using the differential and cumulative test equations. A third equivalent circuit model known as the Average model is shown in the final row of Table 2.2. This model is developed by taking the average of the differential and cumulative test equations. The core-loss resistance and magnetising inductance can be used with the open-circuit rotor equations shown in the first row of Table 2.1 to determine the stator resistance R_s and stator leakage inductance L_{ls}. This gives the equations in Table 2.3 for the stator impedances.

Similarly the rotor resistance R_r and rotor leakage inductance L_{lr} can be determined using the open-circuit stator equations shown in Table 2.1. The equations obtained for the rotor resistances and inductances are given in Table 2.4

The stator and rotor leakage inductances are therefore determined independently using the series coupling tests. This is one of the main advantages that the series coupling tests have over the standard IEEE tests. The leakage inductances determined from the series coupling tests should be more accurate than the standard tests which, as mentioned in Section 2.3, will assume a fixed empirical relationship between the rotor and stator leakages in order to uniquely identify them.

Table 2.3: Equations for stator resistances and inductances.

Test	Resistance	Inductance
Dif	$R_s = \frac{(2n-1)R_{s-or} - R_{r-os} + R_{dif}}{2n}$	$L_{ls} = \frac{(2n-1)L_{s-or} - L_{r-os} + L_{dif}}{2n}$
Cum	$R_s = \frac{(2n+1)R_{s-or} + R_{r-os} - R_{cum}}{2n}$	$L_{ls} = \frac{(2n+1)L_{s-or} + L_{r-os} - L_{cum}}{2n}$
Avg	$R_s = R_{s-or} - \frac{R_{cum} - R_{dif}}{4n}$	$L_{ls} = L_{s-or} - \frac{L_{cum} - L_{dif}}{4n}$

Table 2.4: Equations for rotor resistances and inductances.

Test	Resistance	Inductance
Dif	$R_r = \frac{(2-n)R_{r-os} - n\,R_{s-or} + n\,R_{dif}}{2}$	$L_{lr} = \frac{(2-n)L_{r-os} - n\,L_{s-or} + n\,L_{dif}}{2}$
Cum	$R_r = \frac{(2+n)R_{r-os} + n\,R_{s-or} - n\,R_{cum}}{2}$	$L_{lr} = \frac{(2+n)L_{s-or} + n\,L_{r-os} - n\,L_{cum}}{2}$
Avg	$R_r = R_{r-os} - \frac{n\,R_{cum} - n\,R_{dif}}{4}$	$L_{lr} = L_{r-os} - \frac{n\,L_{cum} - n\,L_{dif}}{4}$

In the case where the effective turns ratio of the machine is one, there will be a total cancellation of magnetising flux in the machine and the differential impedance will consist only of leakage inductances and winding resistances. This condition is benign for the series-coupling tests as the various machine leakage and differential inductances do not vary significantly. This was found to be true for the case of a unity-turns ratio transformer tested in the following chapter.

2.5 Extended Short Circuit Tests

As has been mentioned, the characterisation of a high leakage transformer using the standard two-test approach can lead to inaccurate results in the measurement of inductive parameters due to the high level of leakages in relation to magnetising inductance. A third test can be used in conjunction with the standard two-test approach to provide greater accuracy. In the two-test approach the impedance of the transformer is measured when the secondary coils are open circuited and then short circuited. The third test introduced measures the impedance from the secondary side when the primary is open circuited. The open-circuit tests in the previous section are therefore used in conjunction with a short circuit test to form the extended-short circuit tests.

The transformer type representation of the per-phase equivalent circuit of the doubly-fed induction machine is again adopted to carry out the extended-short circuit tests on the machine. This method was used as a validation procedure for the series-coupling characterisation tests.

In the extended-short-circuit test the induction machine is locked down at the point where the open-circuit tests were carried out. It is important to lock the machine in the same position for all three tests to ensure that variations in impedance due to rotor position do not affect the test results. The stator coils are then connected in a star configuration and the rotor coils are shorted together. This set up is similar to that of the locked-rotor test, only rather than apply the rated current to the stator coils the differential current used in the series-coupling experimental test is applied. Another difference in the extended-short-circuit test is that the short-circuit test does not neglect the magnetising inductance as is done with a standard locked-rotor test. This means that

the equivalent circuit for this test appears as shown in Figure 2.9(c).

For this characterisation procedure the open-circuit tests are also used. These tests are used to develop a set of equations that allow for the three unknown impedances Z_s, Z_r and Z_m to be determined, where Z_s is the stator impedance, Z_r is the rotor impedance and Z_m is the magnetising impedance.

If the open-circuit rotor test is initially considered it can be noted that when a voltage is applied to the stator coil that the impedance seen consists of the stator resistance and leakage inductance in series with the core-loss resistance and magnetising inductance. This can be determined by considering Figure 2.9(a) and is then expressed by the equation below:

$$Z_{s-or} = (R_s + j\omega L_{ls}) + (R_{cp} + j\omega L_m) = Z_s + Z_m \tag{2.45}$$

Similarly if the open-circuit stator test is considered then the impedance seen from this test consists of the rotor resistance and inductance in series with the core-loss resistance and magnetising inductance referred to the rotor, as seen in Figure 2.9(b). This is shown in the following equation :

$$Z_{r-os} = (R_r + j\omega L_{lr}) + n^2(R_{cp} + j\omega L_m) = Z_r + Z'_m \tag{2.46}$$

If the same analysis is used for the short-circuit test then it can be seen that the impedance seen when a voltage is applied to the stator coils consists of the stator impedance plus the rotor impedance in parallel with the magnetising branch impedance referred to the stator. Again this can be seen in Figure 2.9(c) and will give the following equation.

$$Z_{sc} = Z_s + \frac{Z'_r Z_m}{Z'_r + Z_m} \tag{2.47}$$

Using equations (2.45), (2.46), (2.47) it can be shown that the rotor impedance referred to the

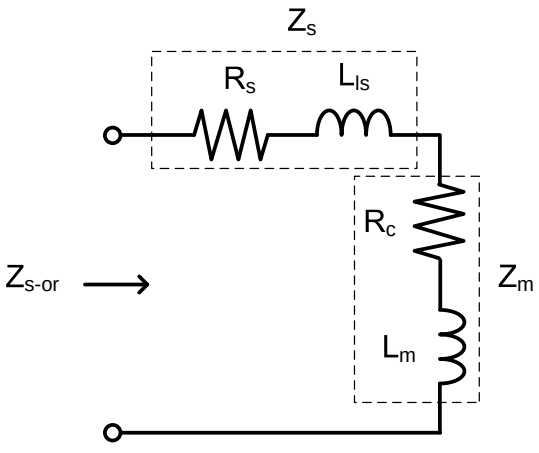

(a) Open-circuit rotor equivalent impedance

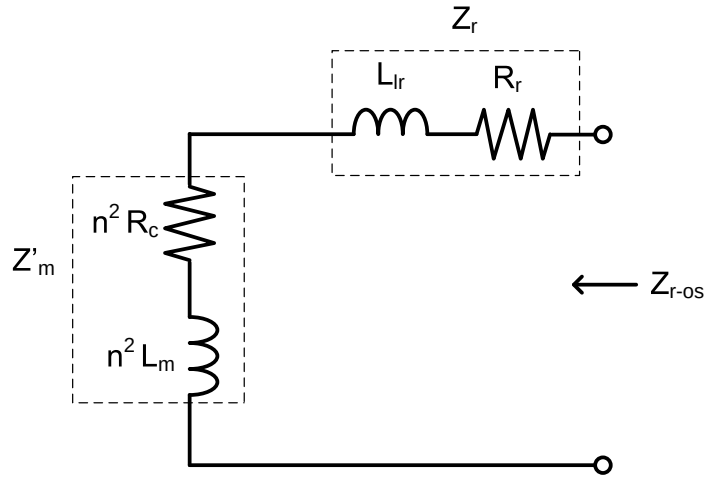

(b) Open-circuit stator equivalent impedance

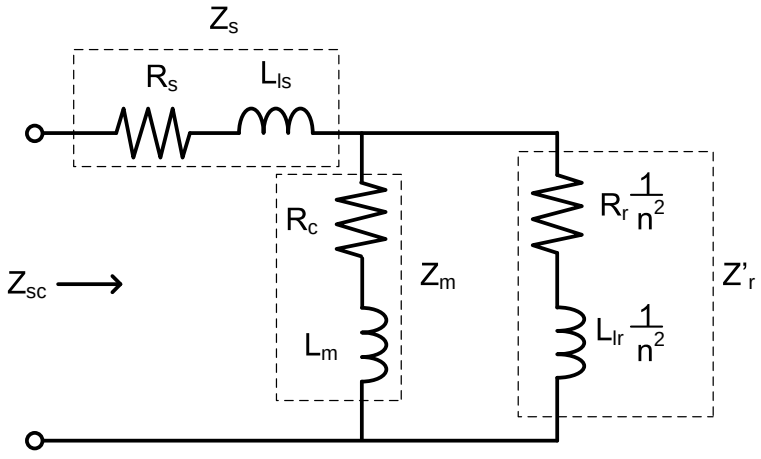

(c) Short circuit equivalent impedance

Figure 2.9: Equivalent circuit for extended short-circuit test of DFIM

stator can be given by:

$$Z'_r = \frac{Z_{r-os}}{n^2} - \sqrt{\frac{Z_{r-os}}{n^2}(Z_{s-or} - Z_{sc})} \tag{2.48}$$

Similarly the magnetising and stator impedances can be found to be given by the following equations:

$$Z_m = \frac{Z_{r-os}}{n^2} - Z'_r \tag{2.49}$$

$$Z_s = Z_{s-or} - Z_m \tag{2.50}$$

The impedances calculated from the above equations can be broken into the resistive and inductive elements and referred to the stator or rotor to give the per-phase equivalent circuit of the induction machine.

The drawback of this method is that the machine flux level cannot be controlled in the same manner as the series-coupling test method. The short-circuit test operates at a reduced flux condition when compared to the open-circuit tests and therefore consistency in the flux conditions is lost. This can lead to inaccuracies in the parameter measurements.

2.6 Sensitivity Analysis

Several different methods have been presented to develop equivalent circuit models for the induction machine. An important method of examining induction machine models is to carry out a sensitivity analysis on the model parameters. Sensitivity analysis allows for a relationship between the estimated value from the model and the actual experimental value to be determined by taking the parameter uncertainties into account. The sensitivity function S_{YX} is defined as:

$$S_{YX} = \frac{\delta Y}{\delta X}\frac{X}{Y} \approx \frac{\frac{\Delta Y}{Y}}{\frac{\Delta X}{X}} \tag{2.51}$$

where X is the parameter that influences Y [60].

The sensitivity of the estimated circuit parameters with respect to the experimental measurements for the differential and cummulative tests is then determined. The measurements are open-circuit rotor (OR), open-circuit stator (OS), cumulative, differential and short-circuit voltages, currents and power factors. It is with respect to these quantities that the circuit parameters are analysed.

The equations developed in this chapter for the circuit parameters using the various test methods are analysed using the sensitivity function and this yields the expressions given in Tables 2.5 and 2.6. By substituting the measured quantities into the equations from Sections 2.4 and 2.5 the effect of error in open-circuit-stator, open-circuit-rotor, cumulative, differential and short-circuit measurements on each of the parameters can be determined for the various test procedures.

By examining Tables 2.5 and 2.6 it can be seen that each equation refers to the sensitivity of each circuit parameter to the measured experimental quantities. If the first expression in Table 2.5 is considered this gives the sensitivity of parameter R_s to measured open-circuit rotor voltage V_{s-or}. This expression is determined by considering the equation for R_s shown in the second row of Table 2.3 and substituting the measured parameters into this expression. This gives the following equation:

$$R_s = \frac{(2n+1)\,\frac{V_{s-or}\,PF_{s-or}}{I_{s-or}} + \frac{V_{r-os}\,PF_{r-os}}{I_{r-os}} - \frac{V_{cum}\,PF_{cum}}{I_{cum}}}{2n}$$

Taking the partial derivative of this equation and multiplying it by V_{s-or}/R_s gives the sensitivity function:

$$S_{V_{s-or}R_s} = \left(1 + \frac{1}{2n}\right) \frac{PF_{s-or}}{I_{s-or}}\,\frac{V_{s-or}}{R_s}$$

The method for determining the sensitivity expressions shown in Tables 2.5 and 2.6 is explained in more detail in Appendix B.

Table 2.5: Equations for Induction Machine Parameter Sensitivity to Voltage

		Y					
X	$Test$	R_s	X_s	R_c	X_m	R_r	X_r
V_{s-or}	Cum	$\frac{PF(1+\frac{1}{2n})}{I}\frac{V}{R_s}$	$\frac{Sin\phi(1+\frac{1}{2n})}{I}\frac{V}{X_s}$	$-\frac{PF}{2n\times I}\frac{V}{R_c}$	$-\frac{Sin\phi}{2n\times I}\frac{V}{X_m}$	$\frac{n\times PF}{2\times I}\frac{V}{R_r}$	$\frac{n\times Sin\phi}{2\times I}\frac{V}{X_r}$
	Dif	$\frac{PF(1-\frac{1}{2n})}{I}\frac{V}{R_s}$	$\frac{Sin\phi(1-\frac{1}{2n})}{I}$	$\frac{PF}{2n\times I}\frac{V}{R_c}$	$\frac{Sin\phi}{2n\times I}\frac{V}{X_m}$	$-\frac{n\times PF}{2\times I}\frac{V}{R_r}$	$-\frac{n\times Sin\phi}{2\times I}\frac{V}{X_r}$
	Avg	$\frac{PF}{I}\frac{V}{R_s}$	$\frac{Sin\phi}{I}\frac{V}{X_s}$	0	0	0	0
	ESC	$Complex$	$Complex$	$Complex$	$Complex$	$Complex$	$Complex$
V_{r-os}	Cum	$\frac{PF}{2n\times I}\frac{V}{R_s}$	$\frac{Sin\phi}{2n\times I}\frac{V}{X_s}$	$-\frac{PF}{2n\times I}\frac{V}{R_c}$	$-\frac{Sin\phi}{2n\times I}\frac{V}{X_m}$	$\frac{PF(1+\frac{\pi}{2})}{I}\frac{V}{R_r}$	$\frac{Sin\phi(1+\frac{\pi}{2})}{I}\frac{V}{X_r}$
	Dif	$-\frac{PF}{2n\times I}\frac{V}{R_s}$	$-\frac{Sin\phi}{2n\times I}\frac{V}{X_s}$	$\frac{PF}{2n\times I}\frac{V}{R_c}$	$\frac{Sin\phi}{2n\times I}\frac{V}{X_m}$	$\frac{PF(1-\frac{\pi}{2})}{I}\frac{V}{R_r}$	$\frac{Sin\phi(1-\frac{\pi}{2})}{I}\frac{V}{X_r}$
	Avg	0	0	0	0	$\frac{PF}{I}\frac{V}{R_r}$	$\frac{Sin\phi}{I}\frac{V}{X_r}$
	ESC	$Complex$	$Complex$	$Complex$	$Complex$	$Complex$	$Complex$
V_{cum}	Cum	$-\frac{PF}{2n\times I}\frac{V}{R_s}$	$-\frac{Sin\phi}{2n\times I}\frac{V}{X_s}$	$\frac{PF}{2n\times I}\frac{V}{R_c}$	$\frac{Sin\phi}{2n\times I}\frac{V}{X_m}$	$-\frac{n\times PF}{2\times I}\frac{V}{R_r}$	$-\frac{n\times Sin\phi}{2\times I}\frac{V}{X_r}$
	Avg	$-\frac{PF}{4n\times I}\frac{V}{R_s}$	$-\frac{Sin\phi}{4n\times I}\frac{V}{X_s}$	$\frac{PF}{4n\times I}\frac{V}{R_c}$	$\frac{Sin\phi}{4n\times I}\frac{V}{X_m}$	$-\frac{n\times PF}{4\times I}\frac{V}{R_r}$	$-\frac{n\times Sin\phi}{4\times I}\frac{V}{X_r}$
V_{dif}	Dif	$\frac{PF}{2n\times I}\frac{V}{R_s}$	$\frac{Sin\phi}{2n\times I}\frac{V}{X_s}$	$-\frac{PF}{2n\times I}\frac{V}{R_c}$	$-\frac{Sin\phi}{2n\times I}\frac{V}{X_m}$	$\frac{n\times PF}{2\times I}\frac{V}{R_r}$	$\frac{n\times Sin\phi}{2\times I}\frac{V}{X_r}$
	Avg	$\frac{PF}{4n\times I}\frac{V}{R_s}$	$\frac{Sin\phi}{4n\times I}\frac{V}{X_s}$	$-\frac{PF}{4n\times I}\frac{V}{R_c}$	$-\frac{Sin\phi}{4n\times I}\frac{V}{X_m}$	$\frac{n\times PF}{4\times I}\frac{V}{R_r}$	$\frac{n\times Sin\phi}{4\times I}\frac{V}{X_r}$
V_{sc}	ESC	$Complex$	$Complex$	$Complex$	$Complex$	$Complex$	$Complex$

Table 2.6: Equations for Induction Machine Parameter Sensitivity Power Factor

		Y					
X	$Test$	R_s	X_s	R_c	X_m	R_r	X_r
PF_{s-or}	Cum	$\frac{V(1+\frac{1}{2n})}{I}\frac{PF}{R_s}$	$\frac{V\times PF(1+\frac{1}{2n})}{I\sqrt{1-PF^2}}\frac{PF}{X_s}$	$-\frac{V}{2n\times I}\frac{PF}{R_c}$	$-\frac{V\times PF}{2n\times I\sqrt{1-PF^2}}\frac{PF}{X_m}$	$\frac{n\times V}{2\times I}\frac{PF}{R_r}$	$\frac{n\times V\times PF}{2\times I\sqrt{1-PF^2}}\frac{PF}{X_r}$
	Dif	$\frac{V(1-\frac{1}{2n})}{I}\frac{PF}{R_s}$	$\frac{V\times PF(1-\frac{1}{2n})}{I\sqrt{1-PF^2}}\frac{PF}{X_s}$	$\frac{V}{2n\times I}\frac{PF}{R_c}$	$\frac{V\times PF}{2n\times I\sqrt{1-PF^2}}\frac{PF}{X_m}$	$-\frac{n\times V}{2\times I}\frac{PF}{R_r}$	$-\frac{n\times V\times PF}{2\times I\sqrt{1-PF^2}}\frac{PF}{X_r}$
	Avg	$\frac{PF}{I}\frac{V}{R_s}$	$-\frac{V\times PF}{I\sqrt{1-PF^2}}\frac{PF}{X_s}$	0	0	0	0
	ESC	$Complex$	$Complex$	$Complex$	$Complex$	$Complex$	$Complex$
PF_{r-os}	Cum	$\frac{V}{2n\times I}\frac{PF}{R_s}$	$-\frac{V\times PF}{2n\times I\sqrt{1-PF^2}}\frac{PF}{X_s}$	$-\frac{V}{2n\times I}\frac{PF}{R_c}$	$-\frac{V\times PF}{2n\times I\sqrt{1-PF^2}}\frac{PF}{X_m}$	$\frac{V(1+\frac{\pi}{2})}{I}\frac{PF}{R_r}$	$-\frac{V\times PF(1+\frac{\pi}{2})}{I\sqrt{1-PF^2}}\frac{PF}{X_r}$
	Dif	$-\frac{V}{2n\times I}\frac{PF}{R_s}$	$\frac{V\times PF}{2n\times I\sqrt{1-PF^2}}\frac{PF}{X_s}$	$\frac{V}{2n\times I}\frac{PF}{R_c}$	$-\frac{V\times PF}{2n\times I\sqrt{1-PF^2}}\frac{PF}{X_m}$	$\frac{V(1-\frac{\pi}{2})}{I}\frac{PF}{R_r}$	$-\frac{V\times PF(1-\frac{\pi}{2})}{I\sqrt{1-PF^2}}\frac{PF}{X_r}$
	Avg	0	0	0	0	$\frac{V}{I}\frac{PF}{R_r}$	$-\frac{V\times PF}{I\sqrt{1-PF^2}}\frac{PF}{X_r}$
	ESC	$Complex$	$Complex$	$Complex$	$Complex$	$Complex$	$Complex$
PF_{cum}	Cum	$-\frac{V}{2n\times I}\frac{PF}{R_s}$	$\frac{V\times PF}{2n\times I\sqrt{1-PF^2}}\frac{PF}{X_s}$	$\frac{V}{2n\times I}\frac{PF}{R_c}$	$-\frac{V\times PF}{2n\times I\sqrt{1-PF^2}}\frac{PF}{X_m}$	$-\frac{n\times V}{2\times I}\frac{PF}{R_r}$	$\frac{n\times V\times PF}{2\times I\sqrt{1-PF^2}}\frac{PF}{X_r}$
	Avg	$-\frac{V}{4n\times I}\frac{PF}{R_s}$	$\frac{V\times PF}{4n\times I\sqrt{1-PF^2}}\frac{PF}{X_s}$	$\frac{V}{4n\times I}\frac{PF}{R_c}$	$-\frac{V\times PF}{4n\times I\sqrt{1-PF^2}}\frac{PF}{X_m}$	$-\frac{n\times V}{4\times I}\frac{PF}{R_r}$	$\frac{n\times V\times PF}{4\times I\sqrt{1-PF^2}}\frac{PF}{X_r}$
PF_{dif}	Dif	$\frac{V}{2n\times I}\frac{PF}{R_s}$	$-\frac{V\times PF}{2n\times I\sqrt{1-PF^2}}\frac{PF}{X_s}$	$-\frac{V}{2n\times I}\frac{PF}{R_c}$	$\frac{V\times PF}{2n\times I\sqrt{1-PF^2}}\frac{PF}{X_m}$	$\frac{n\times V}{2\times I}\frac{PF}{R_r}$	$-\frac{n\times V\times PF}{2\times I\sqrt{1-PF^2}}\frac{PF}{X_r}$
	Avg	$\frac{V}{4n\times I}\frac{PF}{R_s}$	$-\frac{V\times PF}{4n\times I\sqrt{1-PF^2}}\frac{PF}{X_s}$	$-\frac{V}{4n\times I}\frac{PF}{R_c}$	$\frac{V\times PF}{4n\times I\sqrt{1-PF^2}}\frac{PF}{X_m}$	$\frac{n\times V}{4\times I}\frac{PF}{R_r}$	$-\frac{n\times V\times PF}{4\times I\sqrt{1-PF^2}}\frac{PF}{X_r}$
PF_{sc}	ESC	$Complex$	$Complex$	$Complex$	$Complex$	$Complex$	$Complex$

Table 2.5 shows the sensitivity of the circuit parameters to the experimental voltages in each test and Table 2.6 gives the sensitivity of the circuit parameters to the experimental power factors. For example, the first expression shown in Table 2.5, gives the sensitivity of stator resistance, R_s to open-circuit-rotor voltage, V_{s-or}, when R_s is determined using the cumulative test method, of which the open-circuit test is a component. Moving down this column gives the sensitivity of R_s to V_{s-or} for the other test procedures. The 'Test' column outlines the testing procedure being analysed in each case, i.e. cumulative (Cum), differential (Dif), average (Avg) or extended-short-circuit (ESC).

In these tables, ϕ is the inverse cosine of the power factor. It should also be noted that the sensitivity of parameters in the series-coupling tests to current measurements is given as:

$$S_{YI} = -S_{YV} \tag{2.52}$$

where S_{YV} is the sensitivity of parameters to voltage measurements. Hence, the sensitivity of parameters to measured currents can be easily determined using the results shown in Table 2.5.

The partial derivatives for the extended short-circuit tests are complex in nature and are not shown in Tables 2.5 and 2.6 due to the length of the expressions. These expressions have been solved using mathematical analysis software.

2.7 Conclusion

The characterisation of transformers, electrical machines and power inductors is important for predicting the performance of these devices when employed in electrical systems. In the characterisation of high-leakage transformers, inaccurate results can be obtained from the standard two-test approach. This has led to the novel series-coupling tests being developed to characterise these types of transformers. Another novel three-test approach, known as the extended short-circuit test, has also been employed in characterising high leakage transformers. Both testing procedures have been found to provide more accurate results than the standard two test approach.

The doubly-fed induction machine can be represented by a transformer-type equivalent circuit. Therefore, the application of the series-coupling tests and the extended-short-circuit tests is possible as an alternative to the IEEE Standard 112 test methods. The series-coupling tests consist of the cumulative and differential tests which occur when the rotor of the machine is locked at the maximum and minimum inductive points, respectively.

These tests are found to determine the leakage inductances independently, and do not make assumptions about these elements. This is a clear advantage of the series-coupling tests as the assumptions made in the IEEE Standard 112 tests can lead to inaccuracies in parameter estimation.

The extended-short-circuit test is a further method that can be used to determine the parameters in the equivalent circuit of the DFIM. This test uses the open-circuit tests in conjunction with a locked-rotor short-circuit test to determine the machine parameters. A drawback of this test method is that the flux levels in the machine are not controlled in the same manner as the series-coupling tests and this can lead to inaccuracies in the parameter estimation.

Sensitivity analysis is a method used to quantify how an output parameter is influenced by errors in an input measurement. This method was carried out on the different test procedures to quantify the effect experimental measurement error has on machine models. Expressions were developed in this chapter for the sensitivity functions for each circuit parameter for the series-coupling test methods.

3

Experimental Results and Sensitivity Analysis

3.1 Introduction

This chapter outlines the experimental testing of a unity turns-ratio PWB integrated transformer and two doubly-fed induction machines (DFIMs) using the testing methodologies outlined in Chapter 2. The PWB integrated transformer is a low power high-frequency device and is characterised using standard open and short (SOS) tests, series coupling and extended short circuit (ESC) tests. The DFIMs tested are a 1.1 kW, 2-pole pair, 50 Hz DFIM, [63], and also a 30kW, 2-pole pair, 50 Hz DFIM, [64]. The two machines are characterised initially and then the models are compared by predicting the torque versus speed characteristic of the two machines. As has

been mentioned previously, the DFIM is a high-leakage machine and high-leakage machines can be desirable in wind generation for fault ride-through. The 1.1 kW and 30 kW machine in this paper have leakages of 9% and 5.5%, respectively. Published leakages of MW scale DFIMs used in wind turbines range from 3%, [65], to 7%, [66]. Thus, the series-coupling tests can be used to characterise these relatively loosely-coupled machines.

The torque versus speed characteristic for the machine is determined using a dc machine to load the induction machine, with the rotor shorted, and this allows for different operating points to be obtained experimentally. Once the torque versus speed profile of the machine has been obtained experimentally, a calculated torque-speed curve is developed for each model using induction machine equations. The accuracy of each testing model is then determined based on its prediction of the torque versus speed characteristic of the DFIM.

Sensitivity analysis is presented as a method of determining the suitablity of each test method for the purposes of characterising each machine and the PWB transformer. This analysis is used to determine how sensitive the estimation of equivalent-circuit parameters in each procedure is to error in experimental measurements, and has been used previously in machine parameter characterisation and estimation exercises. This analysis is used in conjunction with the results obtained for the parameters to determine which of the tests were best suited for characterising each of the devices.

The variation of the parameters with machine flux conditions is also analysed. The series-coupling tests allow for the determination of equivalent-circuit parameters at controlled flux levels in the DFIM. Tests were carried out at various test flux conditions and the variation of the parameters at these various levels is also investigated in this chapter.

Initially, the procedure for determining the effective turns ratio of the two DFIMs is given in Section 3.2. Testing of the high-leakage PWB transformer is presented in Section 3.3. Experimental results for parameter measurement, the comparison of torque-speed profiles and sensitivity analysis are then presented for the 1.1 kW machine followed by a similar analysis for the 30 kW DFIM in Sections 3.4 and 3.5 respectively. Finally, the variation of equivalent-circuit parameters

with machine flux conditions is analysed in Section 3.6.

3.2 Determining the Effective Turns Ratio

As has been mentioned previously, for the series-coupling tests to be carried out the effective stator-to-rotor turns ratio of the machine must be known. In the case of most transformers the primary to secondary turns ratio is usually known. However, in the case of DFIMs this may not be the case. The effective turns ratio for the DFIM is determined by carrying out a locked-rotor open-circuit test. Initially, a voltage is applied to the stator coils and the input current is measured. The voltage equation in this case is given by the following expression:

$$V_s = E_s + I_s Z_s \tag{3.1}$$

where V_s is the applied stator voltage, E_s is the voltage across the magnetising branch, I_s is the applied stator current and Z_s is the stator impedance.

The applied stator current is assumed to be purely reactive as in the locked-rotor case, the current drawn is assumed to be the magnetising current. The voltage drop across the stator impedance is then estimated, and rearranging (3.1), gives the following expression for the voltage across the magnetising branch:

$$E_s = V_s - (-jI_s)(R_s + jX_s) \tag{3.2}$$

The magnitude of the voltage across the magnetising branch is then determined by taking the magnitude of (3.2) giving the following expression:

$$E_s = \sqrt{(V_s - I_s X_{ls})^2 + (I_s R_s)^2} \tag{3.3}$$

Using this equation with the results from the IEEE tests as an initial estimate of the stator impedance, the emf on the stator is found. A voltage is then applied to the rotor side with the stator in open-circuit configuration. The voltage applied to the rotor is increased until a voltage that is equal to E_s is measured on the open-circuit stator. The turns ratio of the machine is then the ratio of the stator to rotor current for this condition. The resulting turns ratios were 0.667 and 0.375 for the 1.1 kW and 30 kW DFIMs, respectively.

In the case of the 30 kW Marelli DFIM the turns ratio was also calculated using known information about the stator and rotor winding configurations, [67]. This method independently calculated the turns ratio at 0.375, validating the approach used in this chapter.

3.3 Testing of PWB-integrated transformer

This section investigates a low-power (1 W) high-frequency (1 MHz) transformer with high winding resistances, high leakage inductances, and low magnetizing inductance [33]. This transformer is an experimental prototype developed to investigate the use of electro-deposited Permalloy (80/20 nickel iron alloy) as the ferromagnetic material for magnetics integrated into a PWB. The construcion and operation of this transformer is described in [33, 68].

3.3.1 Equivalent-circuit parameter testing for PWB transformer

The transformer has a unity turns ratio with 26 turns on both the primary and secondary sides. The parameter measurements for each test were carried out on the HP 4284A Precision LCR meter [69]. The meter was tested and calibrated to ensure accurate measurements were obtained. The measurements were taken at a frequency of 100 kHz. As was mentioned in Chapter 2, the test current must be specified to ensure the flux levels in the transformer are controlled correctly for the series-coupling tests. From (2.44) the cumulative current will need to be a half of the specified open-circuit secondary (rotor) current. In the case of the differential current the equation suggests that an infinite current would be required. However, it has been found that there is a total flux

cancellation in this case meaning that the variation in parameters to test current is minimal. The differential current used was therefore set to the maximum permissible current, which was the same as the short-circuit current.

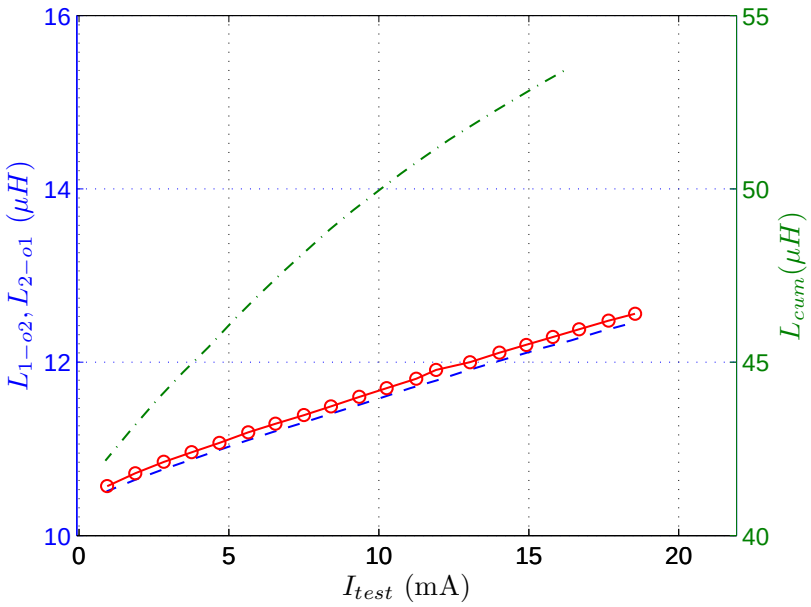

Figure 3.1: Plot of inductance vs. test current L_{1-o2} (- -), L_{2-o1} $(-o)$, L_{cum} $(-\cdot)$

The variation of open-circuit secondary L_{1-o2}, open-circuit primary L_{2-o1} and cumulative inductance L_{cum} and open-circuit secondary R_{1-o2}, open-circuit primary R_{2-o1} and cumulative resistance R_{cum} with applied test current are shown in Figure 3.1 and Figure 3.2 respectively.

It can be seen in these plots that the test current levels and the flux levels are important for the open-circuit and cumulative test measurements. In the case of the short-circuit secondary test, the variation of current is not found to vary the parameter measurements, as is shown in Figure 3.3. This was also found to be true in the case of the differential test for this transformer. As has been mentioned, in the case of the differential test there is a total flux cancellation due to the unity turns ratio and hence the parameters do not vary with flux excitation level.

These plots were used to determine the resistance and inductance at the particular test currents

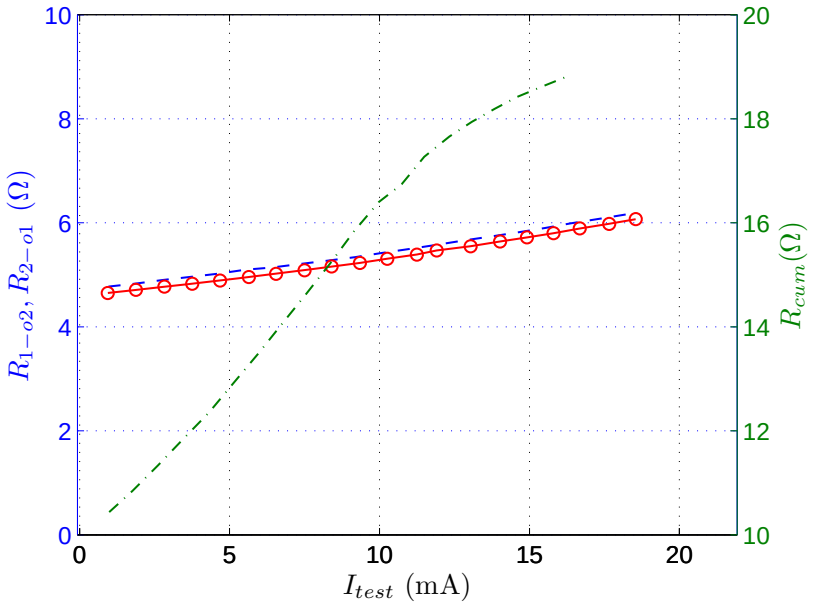

Figure 3.2: Plot of resistances vs. test current R_{1-o2} (- -), R_{2-o1} $(-o)$, R_{cum} $(-\cdot)$

required for each test through an interpolation method. The measurement values for the resistances and inductances for each method at a specified open-circuit current are shown in Table 3.1.

Table 3.1: Experimental measurements for the open-circuit, series-coupling and short-circuit tests for PWB transformer.

	Z_{1-o2}	Z_{2-o1}	Z_{sc}	Z_{cum}	Z_{dif}	Z_{dif}^{FEA}	% error
I(mA)	9	9	18	4.5	18	-	-
$R(\Omega)$	5.33	5.2	7.41	12.48	8.77	7.98	9.0
$L(\mu$H)	11.47	11.56	3.15	45.61	0.68	0.63	7.4

In this table Z_{1-o2} refers to the impedance seen at the primary when the secondary is an open circuit, Z_{2-o1} is the impedance seen at the secondary when the primary is an open circuit, Z_{sc} is the impedance at the primary when the secondary is short-circuited, Z_{cum} is the cumulative impedance, Z_{dif} is the differential impedance and Z_{dif}^{FEA} is the prediction of the differential impedance using a 3-D finite element analysis (FEA) software package. The final column of the table shows the percentage error between the differential measurements and the FEA simulation.

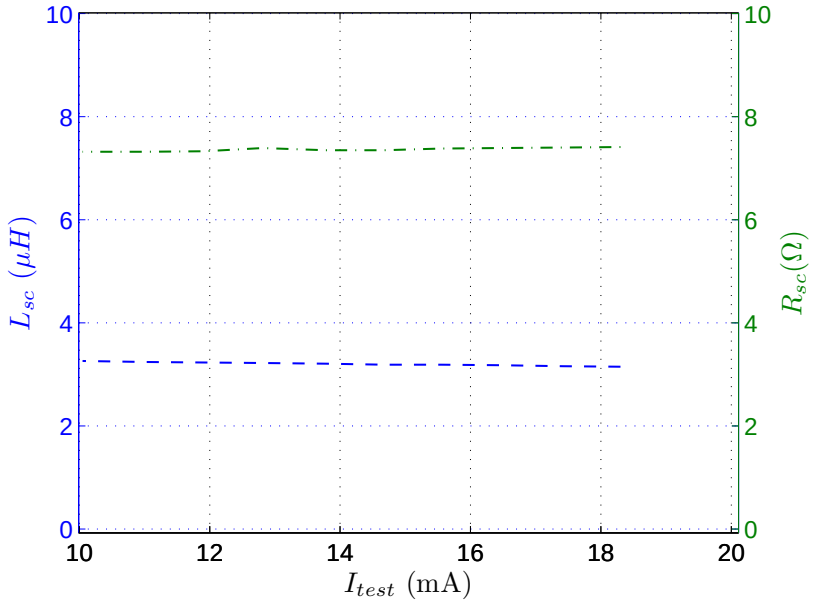

Figure 3.3: Plot of short-circuit resistance and inductance vs. test current L_{sc}(- -), R_{sc} (- ·)

The percentage error between the measurement and simulation is less than 10% for the resistance and inductance measurements. This demonstrates the correlation between the simulation predictions and differential test measurements.

A two-test method known as the standard open and short-circuit (SOS) test was used to characterise the transformer together with the series-coupling and extended short-circuit (ESC) test methods. The SOS test procedure uses the open-circuit secondary and short-circuit secondary tests to calculate the transformer inductances and resistances. For the short-circuit test the equivalent circuit shown in Figure 2.9(c) can be simplified by neglecting the magnetising branch of the transformer. The relationship between the primary and secondary elements are thus given by the following expressions assuming that the primary and reflected secondary series components are equal [70]:

$$R_1 = \frac{R_2}{n^2} = \frac{R_{sc}}{2} \tag{3.4}$$

$$L_1 = \frac{L_2}{n^2} = \frac{L_{sc}}{2} \tag{3.5}$$

By using equations (3.4) and (3.5) to determine the primary and secondary impedances, the open-circuit secondary impedance equation can be used to determine the magnetising branch impedance. The magnetising branch impedances can be found by examining Figure 2.9(a) and using (2.45).

The equivalent-circuit parameters of the transformer based on the measurements shown in Table 3.1 are presented in Table 3.2.

Table 3.2: Experimental results for the series-coupling, extended short-circuit and standard open-short tests.

Test	$R_1(\Omega)$	$L_{l1}(\mu\text{H})$	$R_c(\Omega)$	$L_m(\mu\text{H})$	$R_2(\Omega)$	$L_{l2}(\mu\text{H})$
Cum	4.34	0.18	0.98	11.3	4.23	0.27
Dif	4.45	0.30	0.88	11.2	4.32	0.39
Avg	4.40	0.24	0.93	11.2	4.27	0.33
ESC	4.47	0.27	0.86	11.2	4.34	0.36
SOS	3.71	1.58	1.62	9.9	3.71	1.58

The table shows equivalent-circuit parameters for the PWB transformer using the series-coupling, extended short-circuit (ESC) and standard open and short circuit (SOS) test procedures.

It can be seen in Table 3.2 that the results from the series-coupling tests and the extended short-circuit tests correlated well but the standard open and short-circuit test did not compare well with the other tests. The inaccuracies in the SOS test was to be expected as the simplifying assumptions made were not valid for the high-leakage PWB transformer.

The variation of magnetising inductance with test flux conditions is in Figure 3.4. The figure shows a plot of magnetizing inductance versus primary excitation current as predicted by the

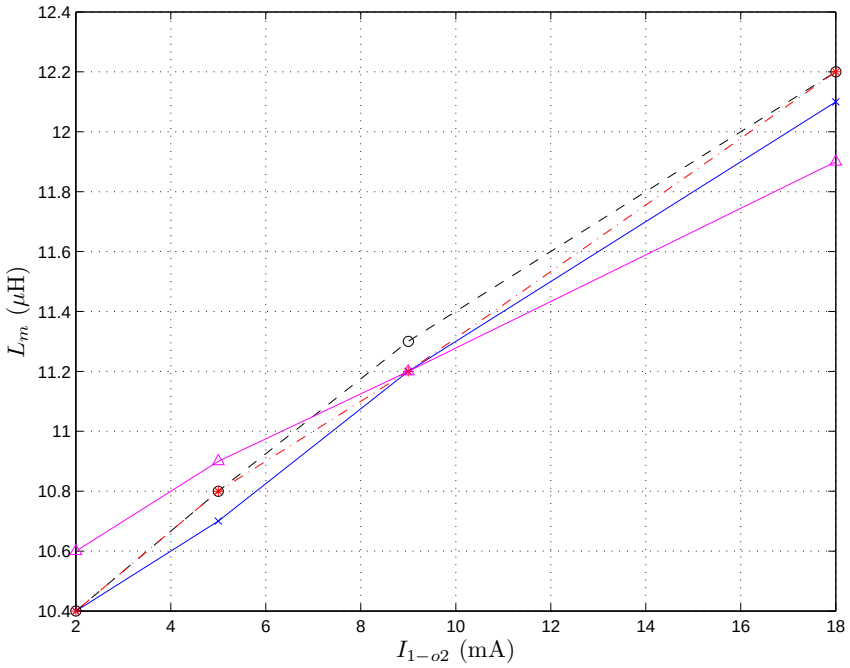

Figure 3.4: Plot of magnetising inductance vs. test current L_{m-dif}(- x), L_{m-cum} ($-\circ$), L_{m-avg} ($-*$), L_{m-ESC} ($-\triangleleft$)

various approaches. The series-coupling approaches have an excellent correlation over the current range. The estimation using the extended open- and short-circuit test skews away from the series-coupling results for the high and low currents. It can be seen for an excitation current of 18 mA, the differential and cumulative tests predict 12.1 and 12.2 μH, respectively, while the EOS prediction is 11.9 μH. This variation happens because the ESC test does not operate with controlled flux levels in the same manner as the series-coupling testing procedures do. This leads to the inaccuracies seen in Figure 3.4.

3.3.2 Sensitivity Analysis of PWB Transformer

As was mentioned in the previous chapter, sensitivity analysis can be used as a method of determining the effect of measurement error on the prediction of equivalent-circuit parameters for each test procedure. This analysis was carried out on each of the testing procedures for the PWB

transformer.

As has been mentioned previously, an LCR analyser was used in the experimental testing of the PWB transformer and thus the sensitivity functions for the measurements are simpler than in the DFIM case. The expressions shown in Tables 2.5 and 2.6 are simplified due to the direct measurement of resistance and inductance in each test. The mesurements taken were open-circuit secondary, open-circuit primary, cumulative, differential and short-circuit secondary resistances and inductances. The sensitivity values for the series-coupling extended-short circuit and standard open and short-circuit tests are shown in Table 3.3.

Table 3.3: Sensitivity analysis of PWB Transformer parameters.

		Y							Y					
$Test$	X	R_1	L_{l1}	R_c	L_m	R_2	L_{l2}	X	R_1	L_{l1}	R_c	L_m	R_2	L_{l2}
Cum	R_{1-o2}	1.8	-	-2.7	-	0.6	-	L_{1-o2}	-	95.6	-	-0.5	-	21.2
Dif		0.6	-	3	-	-0.6	-		-	19.1	-	0.5	-	-14.7
Avg		1.2	-	0	-	0	-		-	47.8	-	0	-	0
ESC		0.5	9.4	3.4	-0.2	-0.7	7.0		-0.5	19.1	2.5	0.6	-0.5	-17.3
SOS		-	-	3.3	-	-	-		-	-	-	1.15	-	-
Cum	R_{2-o1}	0.6	-	-2.7	-	1.8	-	L_{2-o1}	-	32.1	-	-0.5	-	64.2
Dif		-0.6	-	3.0	-	0.6	-		-	-19.3	-	0.5	-	14.8
Avg		0	-	0	-	1.2	-		-	0	-	0	-	35
ESC		-0.4	-5.8	2.1	0.1	0.8	-4.3		0.3	-14.9	-1.6	0.4	0.3	20.7
Cum	R_{cum}	-1.4	-	6.4	-	-1.5	-	L_{cum}	-	-127	-	2.0	-	-84.5
Avg		-0.7	0	3.2	-	-0.7	-		-	-47.5	-	1.0	-	-34.6
Dif	R_{dif}	1.0	-	-5.0	-	1.0	-	L_{dif}	-	1.1	-	0	-	0.9
Avg		0.5	-	-2.4	-	0.5	-		-	0.7	-	0	-	0.6
ESC	R_{sc}	0.9	-13.3	-4.8	0.3	0.9	-9.8	L_{sc}	0.1	6.5	-0.7	-0.2	0.1	4.8
SOS		1	-	-2.3	-	1.0	-		-	1.0	-	-0.2	-	1.0

The table shows that for all tests except the ESC test that the resistance measurements only affect the accuracy of the resistive elements in the equivalent circuit and similarly inductance measurements only affect the inductive elements. This is to be expected as the calculation process for these elements only involve the respective resistance or inductance measurements. In the case of the ESC this is not true as the calculation process involves using the full complex impedances to determine the equivalent-circuit parameters.

The values shown in Table 3.3 demonstrate that the resistances generally have low sensitivites across all methods. This is because this transformer is a relatively high-resistive element and therefore will be less sensitive to errors in resistive measurements. The inductance measurements have a much larger effect on the inductance parameters as demonstrated by the high sensitiviy numbers in the table. The cumulative test in particular is the most sensitive of the characterisation procedures whereas the differential and ESC tests have significantly lower sensitivities. This is demonstrated by examining the sensitivity of primary and secondary inductances to error in cumulative inductance measurements. A 1% error in the measurement of L_{cum} leads to a -127% error in L_{l1} and -84.5% error in L_{l2}. Conversely error in measurement of differential inductance L_{dif} leads to 1.1% error in L_{l1} and 0.9% error in L_{l2}. This difference in sensitivities is because of the nature of both tests. The cumulative test is carried out at a maximum inductance which directly leads to a more sensitive measurement than the minimum inductance measured in the differential test.

The SOS test can be seen to be robust from a sensitivity point of view. However, the inaccuracies in this method arise due to the simlifications made in the calculation process.

3.4 Testing of 1.1 kW Terco machine

3.4.1 Equivalent-circuit parameter testing for 1.1 kW DFIM

The IEEE standard procedures were carried out initially on both machines. Test methods 1, 3 and 4 were carried out on the 1.1 kW machine and are denoted IEEE1, IEEE3 and IEEE4. IEEE test method 2 was not considered for either test machine as this determines the equivalent-circuit parameters for a modified operating frequency.The operating frequency remained at 50 Hz throughout the testing the method outlined has been deemed redundant.

The results from each of the test procedures used in this section are based on the equivalent-circuit model shown in Fig. 2.1. Measurements from the no-load, locked-rotor and dc tests are shown in tables C.1, C.2 and C.3 in Appendix C.

The results obtained from the IEEE tests after five iterations are shown in the first three rows of Table 3.5. The stator resistance results from the dc tests do not account for the skin effect or effects due to temperature rise.

The accuracy of the results for the inductive components are dependent on a reasonable first estimate during the first iteration. It is also assumed that the stator leakage inductance is equal to the referred rotor leakage inductance. The limitation of this testing procedure is in the fact that these assumptions must be made in order to determine the equivalent-circuit values.

The series-coupling tests allow for these values to be obtained without making any such assumptions and also without carrying out an iterative process to improve the resolution of the parameters.

The series-coupling tests were carried out using the turns ratio of 0.667 and the measurements taken for the open-circuit stator, open-circuit rotor, differential, cumulative and short-circuit tests are seen in Table 3.4.

Table 3.4: Experimental measurements for the open-circuit, series-coupling and short-circuit tests for 1.1 kW DFIM.

	Z_{s-or}	Z_{r-os}	Z_{dif}	Z_{cum}	Z_{sc}
I(A)	1.05	1.57	3.14	0.63	3.14
$R(\Omega)$	13.7	7.4	6.4	35.9	7.6
L(mH)	381	169	65	1033	29

The results obtained for the equivalent-circuit parameters from these tests are shown in Table 3.5. The results shown in this table are for one particular test current specified in Table 3.4. Other test currents have also been examined leading to results that correlate well with those presented in Table 3.5. The measurements relating to the series-coupling tests are shown in tables C.4 - C.8 in Appendix C.

The machine parameters calculated for series-coupling tests, in Table 3.5, compare quite well with the IEEE tests. The stator and rotor reactances measured in the series-coupling tests are slightly higher than those of the standard IEEE tests and there is also a difference in how the

Table 3.5: Experimental results for the IEEE, series coupling and extended short circuit tests.

Test	I_{test}(A)	$R_s(\Omega)$	L_{ls}(mH)	$R_c(\Omega)$	L_m(mH)	$R'_r(\Omega)$	L'_{lr}(mH)
IEEE1	-	2.42	14.71	995.09	348.45	5.45	14.71
IEEE3	-	2.42	13.12	995.09	347.05	5.33	13.12
IEEE4	-	2.42	14.84	980.40	343.61	4.65	14.84
Dif	3.14	2.68	17.67	1190.23	366.67	5.57	16.84
Cum	0.63	2.64	18.76	1179.41	365.61	5.53	17.95
Avg	-	2.66	18.21	1184.81	366.14	5.55	17.04
ESC	-	2.54	15.08	1191.15	369.13	5.54	14.19

reactances were divided between the stator and the rotor. The magnetising branch elements are also predicted to be higher in the series-coupling tests.

It is seen that the extended-short-circuit tests produce results that correlate well with the series-coupling test results.

3.4.2 Determination of torque-versus-speed characteristic

Steady state testing was carried out to experimentally obtain the torque-versus-speed characteristic of the machine. The experimentally-obtained curve was then used with torque-versus-speed curves derived from the different equivalent-circuit models determined in the previous section.

The torque-versus-speed curve was obtained by coupling the induction machine to a dc machine and using the dc machine as a load for the induction machine. The rotor coils of the induction machine were shorted together and the stator was fed from a three-phase variable voltage source. The voltage supplied to the stator was reduced to allow for the machine to reach the peak-torque point at this operating condition.

The dc machine armature resistance R_a and constant k_t were known from previous experimental testing. These dc machine parameters are shown in Table C.9 in Appendix C. The dc machine was then connected to a variable external load resistance which allows for the loading of the induction machine at different torque points.

Initially, the induction machine was driven by the dc machine with the induction machine stator coils left on open circuit. The dc machine was supplied by a dc supply at a number of different

voltages. The rotational speed of the dc machine was recorded, as was the armature current drawn by the machine. Using the measurement of current with the machine constant it was possible to determine the friction and windage losses in the system.

The next step was to connect the three-phase variable voltage source to the induction machine and connect the dc machine terminals to the external variable resistance. The line-line stator voltage of the induction machine was set to 125V. The rotational speed of the system and the armature current drawn by the dc machine were measured at different values of external resistance applied to the machine. By using the dc machine torque equation it was possible to obtain the torque experienced in the system at various points. This allowed for the torque-versus-speed characteristic of the induction machine to be obtained. The measurements taken for this experiment are shown in Table C.10 in Appendix C.

The following equations are used to calculate the torque-versus-speed profile of the induction machine using the parameters in the equivalent-circuit models obtained by the various testing procedures [62]:

$$T_{em} = \frac{3}{\omega_{syn}} I_r'^2 \frac{R_r'}{s} \tag{3.6}$$

where ω_{syn} is synchronous speed, I_r' is the magnitude of the rotor current, R_r' is referred rotor resistance and s is slip. I_r' can be determined using the following expression:

$$I_r' = |\frac{E_s}{Z_r'}| \tag{3.7}$$

where E_s is the stator emf and is given by:

$$E_s = V_s - I_s Z_s \tag{3.8}$$

where V_s is the applied per-phase stator voltage and I_s is the stator current which is given by:

$$I_s = \frac{V_s}{Z_{th}} \tag{3.9}$$

where Z_{th} is the per-phase equivalent circuit Thevenin impedance:

$$Z_{th} = Z_s + \frac{Z_m Z'_r}{Z_m + Z'_r} \tag{3.10}$$

Impedance Z'_r is referred to the rotor and must also take into account the variation of slip in the circuit:

$$Z'_r = \frac{R'_r}{s} + jX'_{lr} \tag{3.11}$$

The friction and windage torque determined previously must be added to the measured torque from the experimental results to obtain the electromagnetic torque so that the results can be compared with equation (3.6).

The IEEE test models are shown with the experimental test results in Figure 3.5 while the series-coupling and extended-short-circuit test models are compared to the measured results in Figure 3.6. The results shown in Table 3.6 give the torque values obtained by the different test models at different slip points. The final row in the table shows the experimental data obtained.

The results from Figure 3.5, Figure 3.6 and Table 3.6 illustrate that the series-coupling models are more accurate than either the IEEE or ESC models in predicting machine performance. It can be seen that the IEEE and ESC models over-estimate the torque of the machine as the slip increases. The series-coupling tests are more accurate over the same range. At slips of between 0.5 to 0.4 the peak torque of the machine is seen to occur. It can be seen that the IEEE and ESC tests over-estimate the machines torque in this region, whereas the series-coupling tests provide a

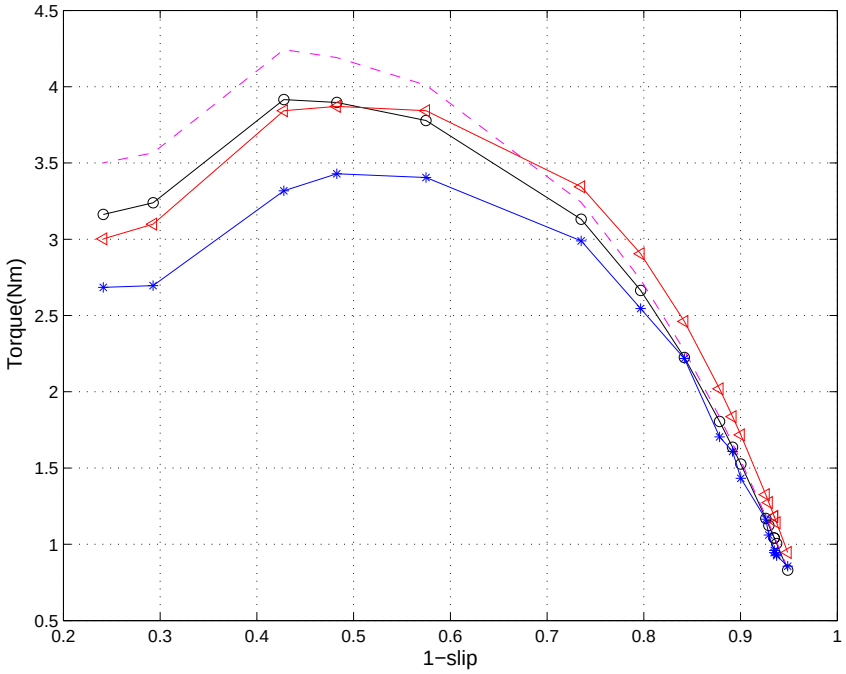

Figure 3.5: Plot of torque vs. slip based on measured ($-*$), IEEE1 ($-\circ$), IEEE3 (- -) and IEEE4 ($-\triangleleft$) models.

more realistic prediction of the machines performance.

The results shown here are for a particular test flux level for the series-coupling tests but tests at other flux levels have been carried out and these also demonstrate a greater accuracy than the IEEE tests. Furthermore the tests have also been carried out for different torque-versus-speed profiles for the machine by exciting it with higher stator voltages. The results for these conditions also show that the series-coupling tests have greater accuracy than the IEEE and ESC tests.

3.4.3 Sensitivity analysis of 1.1 kW Terco machine

The method presented in [60] was used with the induction machine equations for maximum torque, full-load mechanical power and full-load reactive power and, from [71], this leads to the results in Table 3.7. This table shows the sensitivity of the estimated maximum torque, full-load mechanical power and full-load reactive power with respect to the circuit parameters R_s, X_{ls}, R_r, X_{lr} and

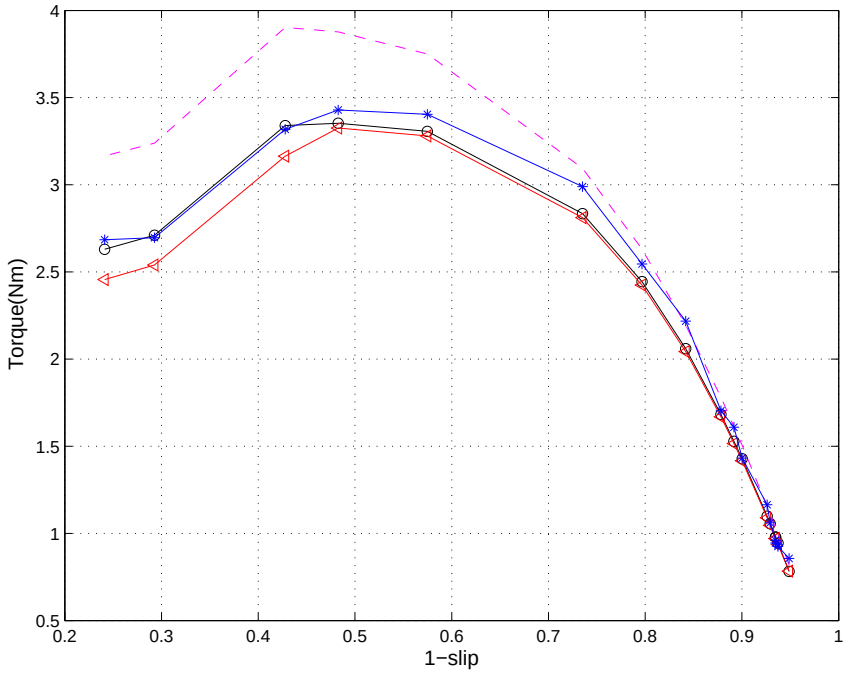

Figure 3.6: Plot of torque vs. slip based on measured ($-*$), dif. ($-\circ$), cum. ($-\triangleleft$) and ESC (- -) models.

X_m. The first three columns of the table represent the cumulative test model while the second three columns show the differential test model. The values given in the table are calculated on a per-unit basis.

Table 3.7 shows that X_{ls} and X_{lr} are the parameters that most influence the accuracy of the maximum torque prediction. This highlights the advantage of using the series-coupling tests as these tests do not make assumptions about the ratios of these reactances and therefore can determine them independantly. This analysis confirms the reasons behind differences in predictions of peak torque in the IEEE and series-coupling tests. It can also be seen from Table 3.7 that R_r and X_m are the parameters that most influence full-load mechanical power and reactive power respectively. Table 3.7 shows that the cumulative and differential tests have similar sensitivites however the sensitivities of equivalent-circuit parameters to experimental measurement has a direct influence on the maximum torque, full-load mechanical power and full-load reactive power

Table 3.6: Speed versus torque results for the series coupling and extended short circuit tests.

Test	$s = 0.1$	$s = 0.2$	$s = 0.43$	$s = 0.57$	$s = 0.76$
T IEEE1 (Nm)	1.53	2.67	3.78	3.92	3.16
T IEEE3 (Nm)	1.55	2.73	4.61	4.24	3.50
T IEEE4 (Nm)	1.72	2.91	3.84	3.83	3.00
T ESC (Nm)	1.51	2.63	3.75	3.90	3.17
T Dif (Nm)	1.43	2.45	3.31	3.34	2.63
T Cum (Nm)	1.42	2.43	3.28	3.16	2.46
T Avg (Nm)	1.43	2.44	3.26	3.27	2.56
T Exp. (Nm)	1.43	2.55	3.40	3.32	2.68

predictions.

Table 3.7: Sensitivity analysis of induction machine model for cumulative and differential tests

Test	Cumulative			Differential		
-	$\frac{\Delta T_m}{T_m}$	$\frac{\Delta P_{m-fl}}{P_{m-fl}}$	$\frac{\Delta Q_{fl}}{Q_{fl}}$	$\frac{\Delta T_m}{T_m}$	$\frac{\Delta P_{m-fl}}{P_{m-fl}}$	$\frac{\Delta Q_{fl}}{Q_{fl}}$
$\frac{\Delta R_s}{R_s}$	-0.66	-0.17	-0.008	-0.69	-0.17	-0.007
$\frac{\Delta X_{ls}}{X_{ls}}$	-0.56	-1.57	-0.05	-0.53	-1.50	-0.05
$\frac{\Delta R_r}{R_r}$	0	-15.87	0.002	0	-15.87	0.0023
$\frac{\Delta X_{lr}}{X_{lr}}$	-0.49	-0.001	0.0017	-0.46	-0.001	0.001
$\frac{\Delta X_m}{X_m}$	0.09	1.63	-0.942	0.87	1.56	-0.95

The next stage of the analysis was to examine at the sensitivity of parameter prediction to experimental error. Initially, the cumulative test is considered and the per unit sensitivity analysis results of this model are shown in Table 3.8. Sample calculations showing the method for determining the values in this table are shown in Appendix B.

It can be seen that the cumulative test model is very sensitive to error in measured experimental quantities. The circuit parameters are all seen to be influenced to a significant extent by the cumulative measurements. It can be seen from Table 3.8 that a 1% error in cumulative voltage measurement will lead to a -41.27% and -44.01% error in stator and leakage reactances respectively. The machines leakage reactances are found to be the most sensitive parameters to error in measurement in the cumulative test.

The sensitivity of machine parameters for the differential test is shown in Table 3.9 and it can

Table 3.8: Sensitivity analysis of induction machine parameters in cumulative tests for 1.1 kW machine.

-	$\frac{\Delta R_s}{R_s}$	$\frac{\Delta X_{ls}}{X_{ls}}$	$\frac{\Delta R_r}{R_r}$	$\frac{\Delta X_{lr}}{X_{lr}}$	$\frac{\Delta R_c}{R_c}$	$\frac{\Delta X_m}{X_m}$
$\frac{\Delta V_{s-or}}{V_{s-or}}$	9.08	35.52	1.86	16.24	-0.93	-0.79
$\frac{\Delta I_{s-or}}{I_{s-or}}$	-9.08	-35.52	-1.86	-16.24	0.93	0.79
$\frac{\Delta PF_{s-or}}{PF_{s-or}}$	9.08	-0.47	1.86	-0.214	-0.93	0.01
$\frac{\Delta V_{r-os}}{V_{r-os}}$	2.09	6.75	4.00	43.39	-0.50	-0.35
$\frac{\Delta I_{r-os}}{I_{r-os}}$	-2.09	-6.75	-4.00	-43.39	0.50	0.35
$\frac{\Delta PF_{r-os}}{PF_{r-os}}$	2.09	-0.13	4.00	-0.56	-0.5	0.01
$\frac{\Delta V_{cum}}{V_{cum}}$	-10.18	-41.27	-4.86	-44.01	2.43	2.14
$\frac{\Delta I_{cum}}{I_{cum}}$	10.18	41.27	4.86	44.01	-2.43	-2.14
$\frac{\Delta PF_{cum}}{PF_{cum}}$	-10.18	0.51	-4.86	0.54	2.43	-0.03

be seen that this test model is not as sensitive to errors in experimental measurements. It can be seen that in particular the sensitivities in the leakage reactances have been greatly reduced. In contrast to the cumulative test, a 1% error in the differential voltage measurement leads to a 2.77% and 2.97% error in stator and rotor leakage reactances respectively.

Table 3.9: Sensitivity analysis of induction machine parameters in differential tests for 1.1 kW machine.

-	$\frac{\Delta R_s}{R_s}$	$\frac{\Delta X_{ls}}{X_{ls}}$	$\frac{\Delta R_r}{R_r}$	$\frac{\Delta X_{lr}}{X_{lr}}$	$\frac{\Delta R_c}{R_c}$	$\frac{\Delta X_m}{X_m}$
$\frac{\Delta V_{s-or}}{V_{s-or}}$	1.28	5.39	-1.85	-17.30	0.93	0.79
$\frac{\Delta I_{s-or}}{I_{s-or}}$	-1.28	-5.39	1.85	17.30	-0.93	-0.79
$\frac{\Delta PF_{s-or}}{PF_{s-or}}$	1.28	-0.07	-1.85	0.23	0.93	-0.01
$\frac{\Delta V_{r-os}}{V_{r-os}}$	-2.07	-7.16	1.99	15.34	0.50	0.35
$\frac{\Delta I_{r-os}}{I_{r-os}}$	2.07	7.16	-1.99	-15.34	-0.50	-0.35
$\frac{\Delta PF_{r-os}}{PF_{r-os}}$	-2.07	0.139	1.99	-0.60	0.50	-0.01
$\frac{\Delta V_{dif}}{V_{dif}}$	1.79	2.77	0.86	2.97	-0.43	-0.14
$\frac{\Delta I_{dif}}{I_{dif}}$	-1.79	-2.77	-0.86	-2.97	0.43	0.14
$\frac{\Delta PF_{dif}}{PF_{dif}}$	1.79	-0.27	0.86	-0.29	-0.43	0.013

The contrast between the sensitivity of the cumulative and differential test models to error in experimental measurements can be explained by the nature of both tests. The cumulative test is carried out at the maximum inductive point of the machine, and therefore errors in measurement

at this point will largely affect the estimated circuit parameters. Conversely, the differential test is carried out at the minimum inductive point. Therefore, errors in experimental measurements are not as critical as in the cumulative test model.

Table 3.10: Sensitivity Analysis of Induction Machine Parameters In Average Tests

_	$\frac{\Delta R_s}{R_s}$	$\frac{\Delta X_{ls}}{X_{ls}}$	$\frac{\Delta R_r}{R_r}$	$\frac{\Delta X_{lr}}{X_{lr}}$	$\frac{\Delta R_c}{R_c}$	$\frac{\Delta X_m}{X_m}$
$\frac{\Delta V_{s-or}}{V_{s-or}}$	5.29	19.77	0	0	0	0
$\frac{\Delta I_{s-or}}{I_{s-or}}$	-5.29	-19.77	0	0	0	0
$\frac{\Delta PF_{s-or}}{PF_{s-or}}$	5.29	-0.28	0	0	0	0
$\frac{\Delta V_{r-os}}{V_{r-os}}$	0	0	3.30	20.96	0	0
$\frac{\Delta I_{r-os}}{I_{r-os}}$	0	0	-3.30	-20.96	0	0
$\frac{\Delta PF_{r-os}}{PF_{r-os}}$	0	0	3.30	-0.41	0	0
$\frac{\Delta V_{cum}}{V_{cum}}$	-5.18	-20.04	-2.81	-21.31	1.21	1.067
$\frac{\Delta I_{cum}}{I_{cum}}$	5.18	20.04	2.81	21.31	-1.21	-1.067
$\frac{\Delta PF_{cum}}{PF_{cum}}$	-5.18	0.27	-2.81	0.29	1.21	-0.014
$\frac{\Delta V_{dif}}{V_{dif}}$	0.89	1.27	0.48	1.35	-0.21	-0.068
$\frac{\Delta I_{dif}}{I_{dif}}$	-0.89	-1.27	-0.48	-1.35	0.21	0.068
$\frac{\Delta PF_{dif}}{PF_{dif}}$	0.89	-0.12	0.48	-0.13	-0.21	-0.007

The benefit of averaging these two methods can be seen in Table 3.10. It can be seen that the average technique has reduced the sensitivity of the circuit parameters to measurements when compared to the cumulative test. For example, the sensitivity of stator and rotor leakage reactances to cumulative voltage is now only -20.04 and -21.31 respectively. A drawback is that the average test is more sensitive to error for these leakage reactances than the differential test due to the effect of the highly-sensitive cumulative test. Therefore the differential test remains the least sensitive of the three series-coupling tests.

3.5 Testing of 30 kW Marelli machine

This doubly-fed induction machine has had the stator re-wound to allow for the coils in each phase to be individually accessed for specific simulation of open- and short-circuit fault conditions, [61]. The machine therefore has different parameters to those that appear in the data given in [64]. The

machine has two pole pairs and is rated at 30 kW, 240 V and 50 Hz. The rated stator current is 59 A and the rotor is rated at 56 A. The stator has 48 slots, 7 turns per coil and there are 16 coils in each phase when the stator windings are connected in series. The rotor has 36 slots, 14 turns per coil and 3 coils in each winding. The steel in the machine is M530 material, [67].

3.5.1 Equivalent-circuit parameter testing

The test results from the IEEE standard procedures use five iterations of the procedure described in method 1. IEEE method 1 was the only one of the four methods presented previously that was carried out on this machine and it is denoted IEEE in this section. The measurements taken for the no-load, locked-rotor and dc tests are shown in Appendix C in Tables C.11, C.12 and C.13 respectively.

The turns ratio of the machine was found to be 0.375 using the method outlined in section 3.2. This number can be validated by noting that the stator has 7 turns per coil and 16 coils giving 112 turns and the rotor has 14 turns per coil and 3 coils giving 42 turns which gives a stator to rotor turns ratio of 0.375.

The results recorded for the open-circuit, differential and the short-circuit tests are shown in Table 3.11. The results shown in this table are for one particular test current. The cumulative test has not been considered due to the highly sensitive nature of this test, as has been shown earlier. Measurements for the open-circuit, differential and the short-circuit are shown in Appendix C in tables C.14, C.15, C.16 and C.17, respectively.

Table 3.11: Experimental measurements for the open-circuit, series-coupling and short-circuit tests for 30 kW DFIM.

	Z_{s-or}	Z_{r-os}	Z_{dif}	Z_{sc}
I(A)	2.94	7.84	4.703	4.703
$R(\Omega)$	4.47	0.64	2.07	1.02
$X(\Omega)$	57.08	8.06	23.43	2.84

Table 3.12 shows the equivalent-circuit parameters determined using each of the characteri-

Table 3.12: Experimental results for the IEEE, differential and extended short-circuit tests for 30 kW DFIM.

Test	$R_s(\Omega)$	L_{ls}(mH)	$R_c(\Omega)$	L_m(mH)	$R'_r(\Omega)$	L'_{lr}(mH)
IEEE	0.41	5.07	606.5	177	0.49	5.07
Dif	0.42	4.65	767.5	178	0.48	5.5
ESC	0.50	4.15	786	178	0.55	5.0
Calc	0.36	5.38	606.5	177	0.47	5.38

sation procedures. The machine parameters calculated for differential and extended-short-circuit tests, in Table 3.12, compare quite well with the IEEE tests. The stator and rotor inductances measured in the differential tests sum together to give approximately the same value as that of the standard IEEE tests. The main difference is again due to how the reactances were divided between the stator and the rotor. Stator resistance measurements from the dc test do not account for the skin effect or temperature rise effects.

The extended-short-circuit test provides a model that compares well with the other two methods. Discrepancies exist between the ESC and differential test method for some of the parameters as the ESC method cannot control the flux level in the same manner as the series-coupling tests.

The final row of Table 3.12 shows the calculated machine parameters from the work carried out in [67]. The resistive elements in this model are based on dc measurements of the stator and rotor circuits with the core-loss resistance assumed to be the value obtained from the IEEE testing. The leakage reactances were calculated using a theoretical approach that takes into account various components such as leakages due to skew, slot leakage, end-winding leakage, zig-zag and belt-leakage reactances. This approach was validated using a standard locked-rotor approach. The magnetising inductance was calculated using the self and mutual inductances obtained for the coils in the stator and rotor circuitry. Again the result obtained was validated experimentally.

The values calculated through this process compared well with the other test procedures outlined in this paper although the leakage reactances were found to be higher than those predicted through the other test procedures. This is because the calculation process makes assumptions that overestimate the leakages in the machine. There are also many degrees of freedom in the leakage

inductance evaluation process that can lead to error being introduced.

3.5.2 Sensitivity analysis of 30 kW Marelli machine

The main difficulty in characterising this machine using the series-coupling tests is in the sensitivity of the tests to error. As has been mentioned, the highly sensitive cumulative test was not considered for this machine as it was found that large errors could occur due to minor errors in measurements. The sensitivity of the differential test is presented in Table 3.13.

Table 3.13: Sensitivity analysis of induction machine parameters in differential tests for 30 kW machine.

–	$\frac{\Delta R_s}{R_s}$	$\frac{\Delta X_{ls}}{X_{ls}}$	$\frac{\Delta R_r}{R_r}$	$\frac{\Delta X_{lr}}{X_{lr}}$	$\frac{\Delta R_c}{R_c}$	$\frac{\Delta X_m}{X_m}$
$\frac{\Delta V_{s-or}}{V_{s-or}}$	-3.58	-13.58	-11.95	-38.46	1.47	1.37
$\frac{\Delta I_{s-or}}{I_{s-or}}$	3.58	13.58	11.95	38.46	-1.47	-1.37
$\frac{\Delta PF_{s-or}}{PF_{s-or}}$	-3.58	0.08	-11.95	0.24	1.47	-0.01
$\frac{\Delta V_{r-os}}{V_{r-os}}$	-2.37	-7.73	8.54	23.73	0.24	0.19
$\frac{\Delta I_{r-os}}{I_{r-os}}$	2.37	7.73	-8.54	-23.73	-0.24	-0.19
$\frac{\Delta PF_{r-os}}{PF_{r-os}}$	-2.37	0.06	8.54	-0.20	0.24	-0.01
$\frac{\Delta V_{dif}}{V_{dif}}$	6.64	22.29	5.53	15.79	-0.68	-0.56
$\frac{\Delta I_{dif}}{I_{dif}}$	-6.64	-22.29	-5.53	-15.79	0.68	0.56
$\frac{\Delta PF_{dif}}{PF_{dif}}$	6.64	-0.17	5.53	-0.12	-0.68	0.02

The sensitivities in this table show that the parameters in the machine can be largely affected by certain measurement errors. These sensitivities, coupled with the low turns ratio of 0.375, and the small absolute values of resistances, particularly on the rotor, can lead to problems in accurately obtaining the correct machine model. The rotor resistance was a small value and was found to be affected by errors in the open-circuit stator test. This is due to the impedance being measured in the open-circuit stator test being small relative to the other tests used, as shown in Table 3.11. For example, the resistance measured in the open-circuit rotor test was 0.64 Ω whereas the resistance in the open-circuit rotor and differential tests were 4.47 Ω and 2.07 Ω respectively. Also, because the turns ratio of the machine is low, the reflection of any error to the stator frame is magnified and significantly affects the overall accuracy of the series-coupling test procedure.

These issues were not as significant for the machine tested in the previous section as the absolute values for the resistances in that machine were significantly higher and the sensitivities of each parameter to measurement error was lower. Also, as the turns ratio in that case was closer to unity, minor errors that were reflected were not overly detrimental to the end result of the test.

Extra precautions must be taken during the testing of the 30 kW machine with the series-coupling tests. Measurement equipment and connecting cables and terminals must be calibrated in order to minimise the effect of measurement sensitivity.

The sensitivity analysis that has been carried out on the differential test was also carried out on the extended-short-circuit (ESC) tests and the IEEE tests. The sensitivity of the parameters obtained from the ESC tests to errors in experimental measurement have a similar sensitivity to error as the differential test. This is because the differential test current is applied to the short-circuit test in the ESC procedure and also that the open-circuit stator impedance is again used in this procedure. The main source of error in this testing procedure lies in the fact that the flux conditions in the ESC test cannot be controlled in the same manner as is done in the series-coupling tests.

The IEEE test models are found not to be as sensitive to error in measurement as the series-coupling test. Again, the major influence in error in the model is therefore not due to measurement error but due to the assumptions made in the procedure.

3.5.3 Determination of torque-versus-speed characteristic for 30 kW Marelli machine

A torque verus speed characteristic was determined for the 30 kW Marelli machine in a similar fashion to the 1.1 kW Terco machine. Once again the parameters of the dc machine coupled to the induction machine were known from previous experimental testing. These parameters are shown in Table C.9 of Appendix C. The friction and windage torque is again determined for the coupled system.

For the testing the line-line voltage applied to the stator terminals was 110 V. The experimental

results obtained are compared with those predicted by the parameters of the equivalent-circuit models from the various test methods. The experimental measurements for this test are shown in Table C.18 of Appendix C. Again equation (3.6) is used to calculate the electromagnetic torque.

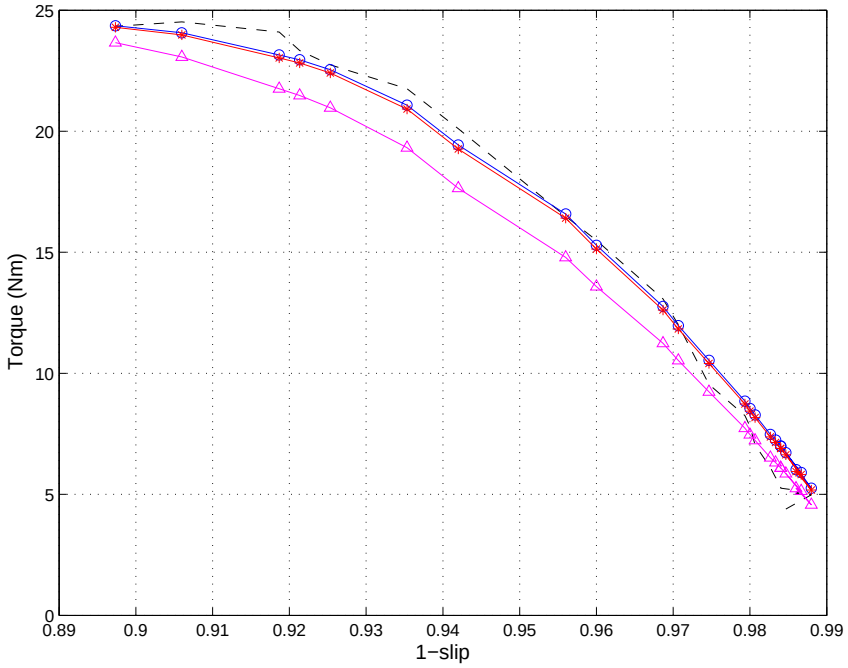

Figure 3.7: Plot of speed vs. torque based on measured (- -) and dif.($-\circ$), IEEE($-*$) and ESC($-\triangleleft$) models.

The results shown in Table 3.14 are shown graphically in Fig.3.7. The values in the table give the torque values calculated from the different test models at different slip points. The final row in the table shows the experimental data obtained.

Table 3.14: Speed vs. torque results for the series-coupling and extended-short-circuit-tests.

Test	$s = 0.016$	$s = 0.02$	$s = 0.04$	$s = 0.08$	$s = 0.1$
T IEEE (Nm)	6.90	8.43	16.41	22.40	24.30
T Dif (Nm)	6.99	8.55	16.58	22.54	24.36
T ESC (Nm)	6.10	7.46	14.79	20.97	23.66
T Exp. (Nm)	5.26	7.82	16.48	22.74	24.34

The table shows the accuracy of the IEEE and differential test models in predicting the mea-

sured torques at different slip levels. Both tests follow the measured torque closely over the slip range shown. The ESC model has less accuracy in predicting the torque-versus-slip characteristic of the machine. This can also be seen graphically in Fig. 3.7.

A theoretical torque versus slip curve for rated conditions is also calculated. The curve is calculated over the full slip range for the differential, IEEE, ESC and calculated model from [67]. The torque versus slip profiles predicted by each model are shown in Fig. 3.8.

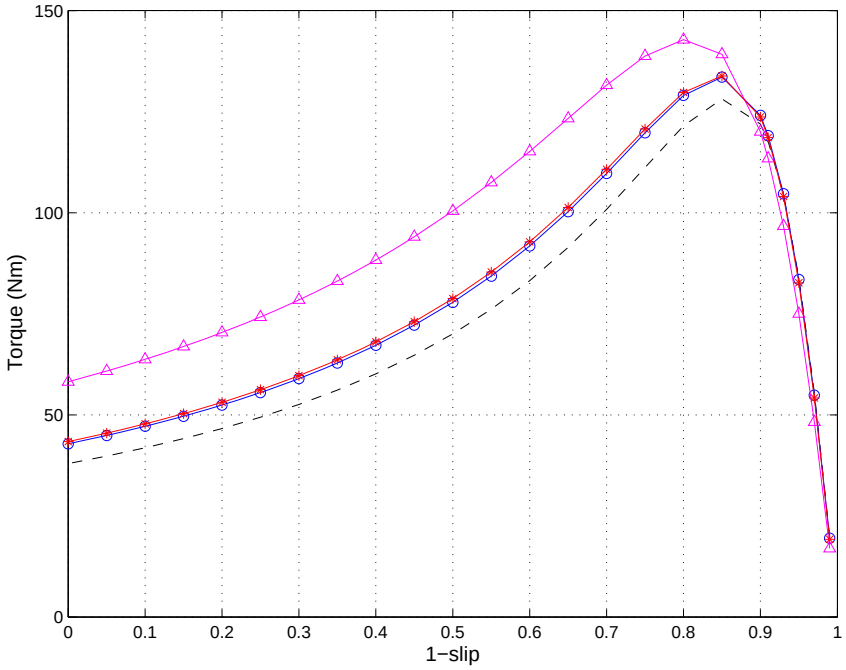

Figure 3.8: Plot of speed vs. torque based on dif.($-\circ$), IEEE($-*$), ESC($-\triangleleft$) and Calc.(- -) models.

The plot shown in Figure 3.8 demonstrates that the models all predict a similar performance in the linear operation of the machine. Differences do occur at the peak torque point at a slip of 0.15 and beyond to the standstill torque. It can be seen that the ESC overestimates these points relative to the IEEE and differential models whereas the calculated model underestimates the torques. This is because the different values of leakages obtained from these models as the leakages are the parameters that become dominant when predicting the torque beyond its peak value.

3.6 Variation of Parameters with Machine Flux Levels

An important attribute of the series-coupling tests is their ability to maintain the machine flux at a controlled level. It is therefore possible to monitor how the machine parameters vary with flux conditions when measured using the series-coupling test methods, as has been shown earlier in the case of the PWB transformer. The parameters can be determined at particular flux levels by applying the specified currents to the open-circuit, cumulative and differential tests as specified in Table 2.1 and equation (2.44) from the previous chapter. By applying these specific currents a controlled flux level is maintained across all the tests. This is a significant advantage over the IEEE and extended-short-circuit tests as these tests do not control the machine flux conditions in the same manner. It has been seen that in the case of the ESC test that inaccuracies occured in both the PWB and the DFIMs tested. The IEEE tests can only operate at one particular flux condition as rated current is required in the locked-rotor test. The ESC test cannot maintain controlled flux levels due to the locked rotor short-circuit test. The curves shown in Figure 3.9 illustrate the variation of resistance and inductance for the open-circuit rotor, open-circuit stator, differential and short-circuit tests to applied open-circuit rotor current levels for the 30 kW Marelli DFIM.

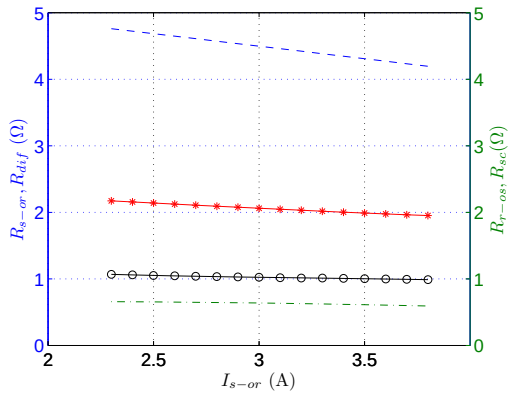

(a) R_{sor}(- -), R_{ros}(- ·), R_{sc} (−○)and R_{dif} (−∗)) resistance.

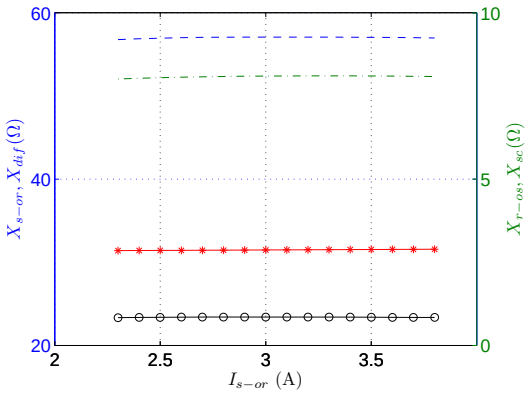

(b) X_{sor}(- -), X_{ros}(- ·), X_{sc} (−○)and X_{dif} (−∗)

Figure 3.9: Measured per-phase resistances and reactances vs. applied open-circuit rotor current for 30 kW DFIM.

It can be seen in these plots that a slight variation is seen in the parameters with varying current levels. Although the variation appears slight the correct measurements at the correct flux levels are vital for accurate characterisation. This is particularly true for the relatively small absolute values of resistances and inductances seen in the 30 kW DFIM. An expanded view of the parameter variations are shown in Figure 3.10.

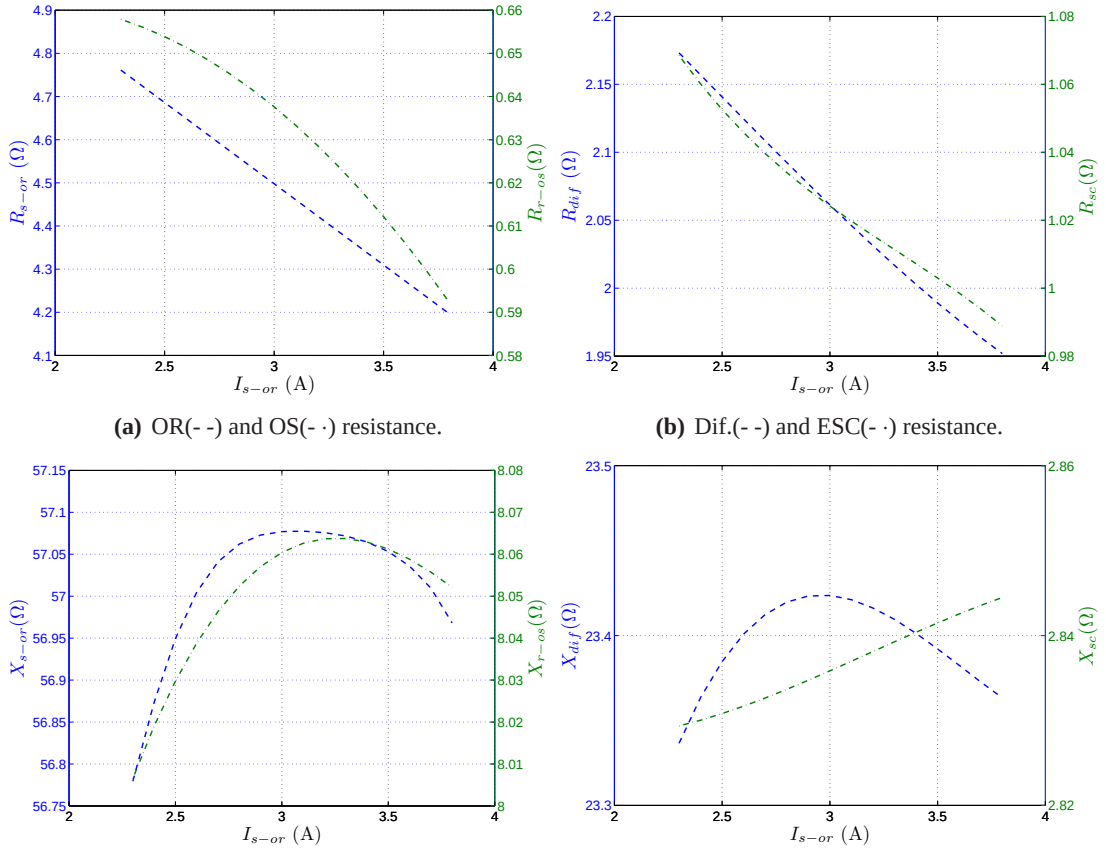

(a) OR(- -) and OS(- ·) resistance.

(b) Dif.(- -) and ESC(- ·) resistance.

(c) OR(- -) and OS(- ·) reactance.

(d) Dif(- -) and ESC(- ·) reactance.

Figure 3.10: Measured per-phase resistances and reactances vs. applied open-circuit rotor current 30 kW DFIM.

The plots show that the variation in resistances due to applied current is approximately linear for each of the different tests. The reactance variation is seen to follow a similar trend for the open-circuit stator and rotor tests. The differential test also shows a similar variation in reactance.

The ESC test has a different variation. This can be explained by the fact that this test operates at a reduced flux condition that is not controlled like the other tests. This confirms the uncontrolled nature of the test in comparison to the series-coupling tests, leading to the inaccuracies in the torque-versus-speed curves for both the 1.1 kW and 30 kW machines.

The variation of machine parameters with the applied open-circuit rotor current for the 30 kW DFIM is shown in Figure 3.11. These figures show the IEEE, ESC and differential tests over a range of currents. The IEEE test values are assumed to be constant over the range of conditions.

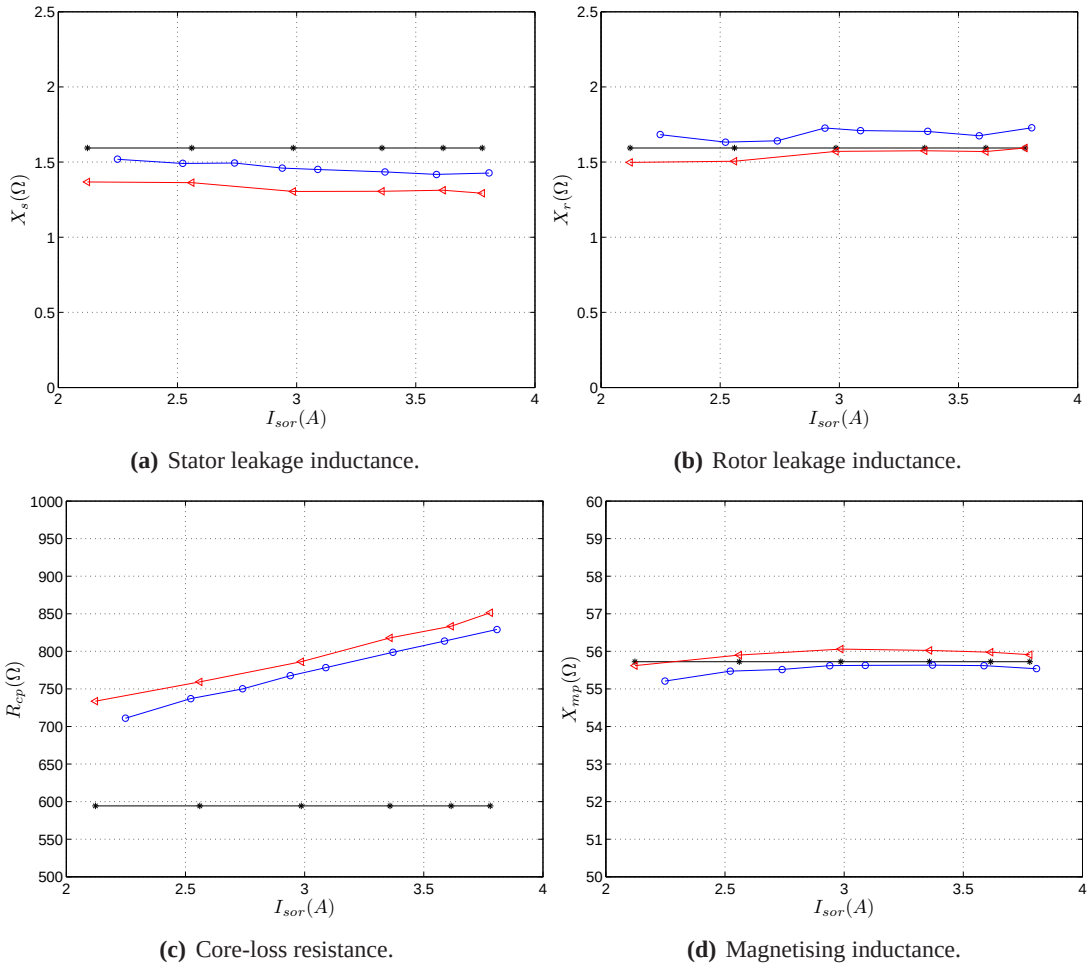

(a) Stator leakage inductance.

(b) Rotor leakage inductance.

(c) Core-loss resistance.

(d) Magnetising inductance.

Figure 3.11: Measured per-phase equivalent-circuit parameters for Dif. (-o), IEEE(-$*$) and ESC (-$\triangleleft$) vs. varying open-circuit rotor current for 30 kW DFIM.

It can be seen from these plots that the reactance values remain approximately constant over the various conditions. The distribution of the stator and rotor reactance can be seen to be different to the fifty-fifty split of the IEEE tests over the range of flux condtions but that the sum of the reactances in both cases compare well over the range of conditions. The core-loss resistance is seen to increase linearly with the increasing current levels. This is because the power level in the core is increasing and the core-loss resistance value needs to change accordingly to reflect this change. This variation of core-loss resistance is not seen in the IEEE test and cannot be analysed through the IEEE approach due to the nature of the tests.

The corresponding analysis of the variation of parameters in the 1.1 kW Terco machine shows a similar variation of parameters with changing flux conditions. Figure 3.12 shows the variation of stator and rotor leakage reactance, core-loss resistance and magnetising inductance of the machine against the open-circuit rotor current for the differential and extended short-circuit tests. The parameters from IEEE Method 1 are also shown.

These plots show that for the 1.1 kW Terco machine, the stator and rotor leakage reactances for the ESC and IEEE tests are seen to be lower than the differential test over the range of conditions. The variation of core-loss reactance and magnetising reactance for the differential and ESC tests correlate well. A similarity between the parameter variation in the 1.1 kW Terco machine and the 30 kW Marelli machine can also be identified in Figures 3.11 and 3.12.

3.7 Conclusion

In this section the characterisation of a PWB integrated transformer, a 1.1 kW Terco DFIM and a 30 kW Marelli machine was carried out using the characterisation test methods presented in Chapter 2. The test methods used for characterising the DFIMs were the IEEE, series-coupling and extended short-circuit tests. As well as the series-coupling tests and the extended short-circuit test, the standard open and short-circuit tests were also used to characterise the PWB tranformer. The results from these methods were compared using experimental steady-state testing and sensitivity

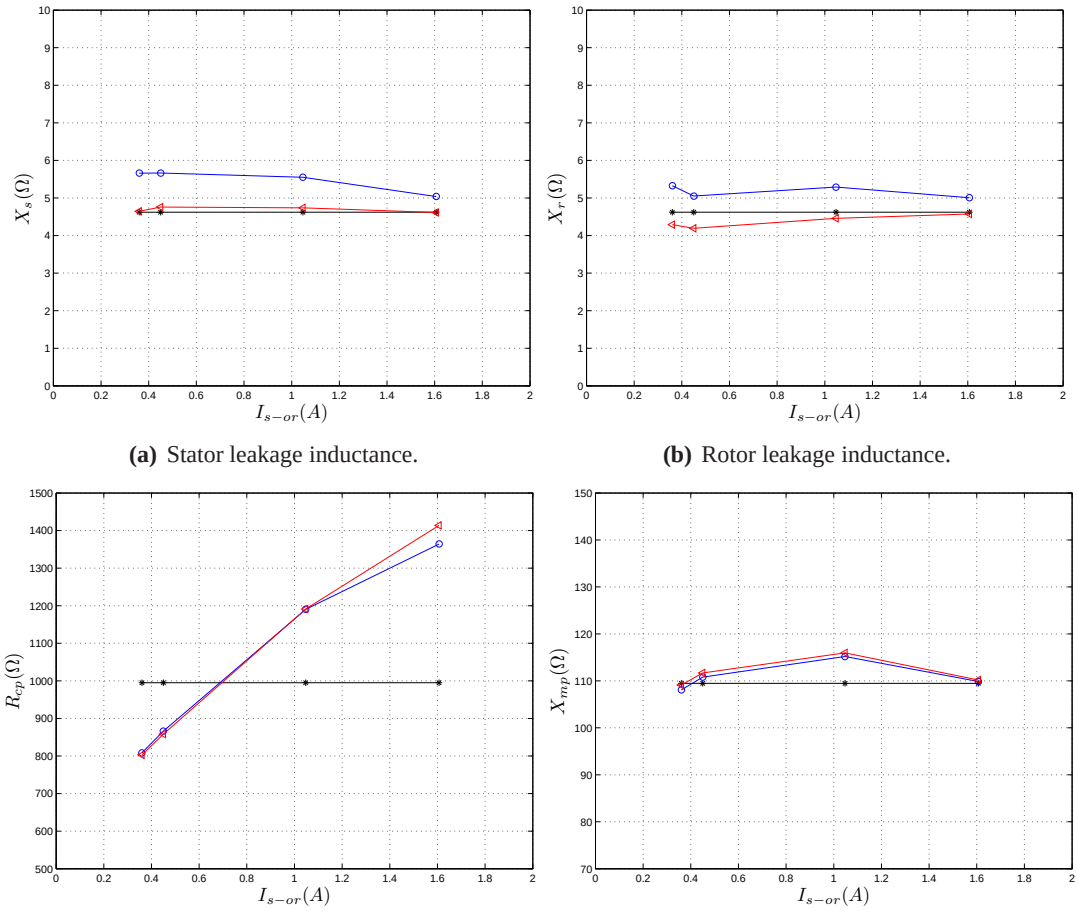

(a) Stator leakage inductance.

(b) Rotor leakage inductance.

(c) Core-loss resistance.

(d) Magnetising inductance.

Figure 3.12: Measured per-phase equivalent-circuit parameters for Dif. (-o), IEEE(-$*$) and ESC (-$\triangleleft$) vs. varying open-circuit rotor current for 1.1 kW DFIM.

analysis.

The series-coupling tests and the extended-short circuit (ESC) tests were found to characterise the PWB transformer with greater accuracy than the standard open- and short-circuit tests. The differential and cumulative tests were found to provide more accuracy in predicting the magnetising inductance than the ESC test as the flux levels within the machine for the ESC test were not controlled leading to inaccuracies.

The series-coupling tests were found to be a more direct method for characterising the two doubly-fed induction machines tested and were best suited for characterising the 1.1 kW DFIM. The predicted machine parameters were found to correlate well with the IEEE and ESC tests for the 1.1 kW machine. The differential test was found to predict the torque-versus-speed characteristic of this machine with a high level of accuracy. The series-coupling tests were found to be more accurate than the IEEE tests at predicting the machines' peak torque and stall torque. A discrepancy between measured torque and the predicted torque existed in the ESC test method. This is because the ESC test does not control flux conditions unlike the differential test.

The results obtained for the characterisation of the 30 kW DFIM showed that series-coupling tests and IEEE tests correlated well. The performance of the differential and IEEE tests in predicting the torque-versus-speed curve for this machine were very similar. In the case of the 30 kW DFIM the parasitic elements are lower than for the 1.1 kW machine, and therefore the IEEE test model is seen to predict the torque profile of the machine with a higher level of accuracy than for the 1.1 kW DFIM. A theoretical torque-versus-speed curve is also shown for the full slip range of the 30 kW machine. This curve showed that the IEEE and series-coupling tests follow each other closely throughout but that there were inaccuracies seen in the ESC test.

Sensitivity analysis is a method used to quantify how an output parameter is influenced by errors in an input measurement. This method was carried out on the different test procedures to quantify the effect experimental measurement error has on the equivalent-circuit models. The series-coupling tests were found to be very sensitive to measurement errors. The cumulative test method was found to be more sensitive to errors in measurement than the differential test due to the

nature of both tests. The sensitivity analysis also highlighted that it is critically important to ensure that all measurements are taken with correctly calibrated equipment to ensure that measurement errors are minimised. This was particularly important for the 30 kW machine tested in this chapter, as due to the relatively small values of resistance and the low turns ratio, a small measurement error can cause large errors in parameter estimation. In the case of the PWB transformer, the calibration of test equipment was also vital to ensure that accurate characterisation was achieved.

The series-coupling tests have the ability to determine the machine parameters at different operating flux conditions by applying the currents that control the flux levels in the test at the required point. The variation of these parameters with applied flux level was investigated. The analysis was carried out on the 30 kW machine and it was seen that the parameter that varied most was the core-loss resistance and that the inductances remained approximately constant for the different operating conditions. A drawback of the IEEE test procedure was that the variation in core-loss resistance could not be quantified using this test method. Differences between the leakages measured for the IEEE tests and the series-coupling tests were seen throughout but it was also seen that the sum of the leakages in both test methods compared well over the range of flux conditions.

In conclusion, it has been demonstrated that the series-coupling tests can provide enhanced per-phase equivalent-circuit model of the doubly-fed induction machine and high-leakage transformers, provided that flux conditions are maintained correctly and that measurement errors are kept as minimal as possible.

4

Modelling of a Wells Turbine for an Oscillating Water Column Wave Energy Converter

4.1 Introduction

The oscillating water column (OWC) wave energy converter (WEC) is currently one of the most advanced wave energy technologies. Operational shore-based devices have been thoroughly tested over a long period and there is currently a drive towards developing offshore devices as the potential for power capture is higher.

Considerable challenges exist for the electrical conversion system in an offshore OWC WEC. Some of the key problems faced are the oscillatory nature of the power profile of the sea and also

the harsh conditions that exist in this environment. Unlike the over-topping and floating hinge devices there are no built in power smoothing components apart from the inertia of the shaft. In [72–74] the reduction of large power fluctuations feeding to the grid is explored by adding storage to the system.

In [72, 73] the use of increased system inertia and variable speed are suggested as methods of smoothing the power supplied to the grid. The paper employs an extra permanent manent magnet generator in the drive-train to provide for variable speed operation. The findings from the paper demonstrate that increased inertia and variable speed operation significantly reduced the peak to average electrical power supplied by the system.

The introduction of battery storage to smooth out short-term variations and superconducting magnetic energy storage (SMES) to deal with longer term storage is investigated in [74]. The requirement of energy storage for these elements are investigated in this paper in the case of standard system inertia and increased system inertia. The combination of the various energy storage options was seen to improve the system performance.

The application of supercapacitor energy storage has also been invesigated for the OWC WEC application in [75]. In this paper the supercapacitor energy storage is investigated for use in low-voltage ride-through scenarios and device start-up as well as minimisation of output electrical power variations. The paper found that the liftime of the supercapacitors was too short to handle the short-term storage requirements of the OWC WEC but was suitable for the device start-up and low-voltage ride-through applications.

The selection of the electrical generator is crucial for any successful WEC to be developed. The advantages and disadvantages of each of the main generator types are investigated in [28]. In [28] the challenges faced for each generator type are investigated and the most appropriate electrical machines for an offshore OWC WEC are presented. These include the synchronous generator (SG), the squirrel cage induction generator (SCIG), the doubly-fed induction generator (DFIG) and the permanent magnet ac generator (PMAC).

This chapter presents the OWC WEC and the Wells turbine which is used in the device power

take-off (PTO). The chapter discusses the development of a software model of the turbine that can be used for analysis of the device. Actual experimental data obtained from a 1:2.5 scale prototype device is used to develop the characteristic non-dimensional torque curve for the device. Simulations of the device coupled to an electrical generation system are carried out with the results compared to the actual experimental prototype data for validation purposes.

Initially an outline of the system operation is given and this is followed by a description of the mathematical model of the air turbine used in the device. The experimental test system is outlined and the development of a software simulation model for the device is presented. Finally simulated results obtained from the software model are compared to the experimental results from the prototype system for various sea conditions.

4.2 The Wells turbine equipped OWC wave energy converters

As was discussed in Chapter 1, the OWC WEC utilises a three step power take-off (PTO) conversion process. Energy in the sea is firstly converted to aerodynamic energy which is then transformed to mechanical energy via an air turbine. The mechanical energy is converted in turn to electrical power via a rotary electrical generator.

The conversion of the reciprocating airflow to mechanical power is carried out using the bi-directional turbine known as the Wells turbine. The Wells turbine is suited to the OWC WEC application as it produces a rectified mechanical power from the reciprocating airflow. The turbine itself has no moving parts other than the rotor as its blades are generally fixed to the rotor structure making it attractive from a maintenance point of view. A drawback of the Wells turbine is that it has a narrow efficiency band meaning its aerodynamic performance drops off significantly outside a particular range of airflows. For this reason a number of solutions have been proposed.

Pitching blade Wells turbines are available to increase efficiency and have been investigated in [76] but are not widely used due to the maintenance concerns associated with them. Variable speed devices have also been proposed but due to the inertia of the system it is generally unfeasible

to vary the speed on a wave-by-wave manner. A third method involves using blow-off or venting valves to release any excess pneumatic power thus preventing the Wells turbine from entering its stall region [77].

In [78] the concept of using guide vanes and blow off valves to improve the operation of the Wells turbine is investigated. It was found that using blade profiles that increase peak efficiency but have a narrow operation range are a good option when used in conjunction with a blow off valve. Conversely if a blow off valve is not used blades with lower peak efficiency but a wider range of operation are preferable.

Other bi-directional turbines have also been investigated to convert the pneumatic power into mechanical form. The impulse turbine has been suggested as an alternative to the Wells turbine. A comparison between the two turbines is presented in [79] and it was found that the Wells turbine produced more power than the impulse turbine and is also smaller in size. Also the impulse turbine was found to suffer from high running losses at low flow values, [80].

A second option using two impulse turbines coupled to a generator on a single shaft is proposed, [81]. This twin topology operates by having one turbine functional for the intake and the second turbine operate during the exhaust. Thus the turbines will each work for a half cycle of the wave period. This operation is analogous to the operation of an electrical full wave recifier using a centre tap transformer and two diodes. The drawback of this system is in the cost associated with employing an extra turbine.

4.3 Wells turbine modelling

This section gives an overview of testing procedures that have been used in characterising the Wells turbine. This is followed by an outline of the theory used to characterise the Wells turbine and its operation used in this study.

4.3.1 Wells turbine testing procedures

As has been mentioned previously, the Wells turbine is well suited to OWC applications due to its bi-directional characteristic. The Wells turbine has been tested variously to determine its operating characteristics. In [82] a contra-rotating Wells turbine is tested. Initially constant flow testing is carried out on the turbine. Linear theory of the Wells turbine is used and quasi-steady state flow assumptions are made. These assumptions mean that effects such as hysteresis in the turbine and damping differences during instroke and outstroke are not modelled. It is found that the constant flow model predicts a higher turbine efficiency than what was experienced when the turbine was used in a reciprocating airflow application.

A model developed using computational fluid dynamics (CFD) is presented in [83]. The CFD model allows for the conversion of pneumatic power to mechanical power to be determined. The pressure inside the chamber and the water level are recorded and these are used to predict the pneumatic power through the turbine. CFD then allows for the flow rate through the turbine to be calculated and this allows for the non-dimensional (ND) torque versus flow coefficient relationship to be determined. The results from this model are compared to the actual results from the system and the predicted results were found to correlate with experimental results to a satisfactory level.

In [84–86] testing of a 1:10 scale OWC device is carried out. The testing involved examining the response of the Wells turbine under the reciprocating flow that is experienced under sea conditions. In [84,85] the performance of the turbine is again determined by investigating the pneumatic power input and the mechanical power output. The pressure in the chamber is recorded and the airflow is derived from the change in water level in the OWC WEC. The mechanical power is derived using the electrical power measurements and dc machine equations. The non-dimensional flow and torque are determined to obtain the devices characteristic curve. Physical phenomena such as aerodynamic stall and hysteresis are observed in the turbine. It is noted that hysteresis mostly occurs during the stall region of the device. In order to characterise the hysteresis correctly the time derivatives of the flow coefficient are taken so that the accelerating and decelerating flows can be viewed.

In [86] a stochastic model of the OWC is used to predict the power output from the device. The model assumes that the Wells turbine has a linear characteristic and linear wave theory is also assumed. Losses due to reciprocating airflow and compressibility of air are also neglected. The paper finds that the model predicts the efficiency profile of the device with a reasonable degree of accuracy. The simplifying assumptions made were found to be reasonable and did not cause the model to be overly inaccurate.

In [87] the Wells turbine torque versus pressure and pressure versus flow profiles are analysed. Electrical output power is used to derive the mechanical torque and a thermodynamic model for the chamber is used with measured water height and pressure to derive the flow of air in the device. Again issues such as hysteresis and stall in the turbine are investigated. It was found that larger peak pressure leads to larger hysteresis being experienced. The differences in the turbine performance is seen in the inflow and outflow conditions for the OWC WEC. It could be seen that the pressure versus flow regimes for the turbine were different for the two modes of operation.

4.3.2 Wells turbine theory

This section outlines the simplified Wells turbine theory which is used in the following section to experimentally develop the Wells turbine model.

The Wells turbine is generally represented in non-dimensional form as this is a more convenient manner of characterising its aerodynamic properties. Aerodynamic quantities pressure, flow and power can be transformed into non-dimensional form using expressions from [88] and [80]:

$$\Psi = \frac{p_c}{\rho_a N^2 D^2} \tag{4.1}$$

$$\Phi = \frac{Q}{A_a U_t} \tag{4.2}$$

$$\Pi = \frac{P_t}{\rho_a N^3 D^5} \tag{4.3}$$

where Ψ is the ND pressure coefficient, p_c is pressure head in the buoy chamber, ρ_a is air density, N is the rotational speed, D is the turbine diameter, Φ is the ND flow coefficient, Q is the axial flowrate, A_a is the annular area, Π is the ND power coefficient and P_t is the turbine power. U_t is the tip velocity of the turbine and is given by:

$$U_t = \frac{D}{2} N \tag{4.4}$$

It has been shown in [88, 89] that Ψ has a linear relationship with Φ for a fixed turbine speed N. The slope of this line is known as the damping ratio and this is denoted B_r. If an electrical analogy is used B_r could be considered the resistance, Ψ would be applied voltage and Φ would be current.

In [80] an efficiency characteristic of the Wells turbine as a function of flow coefficient Φ is given. This characteristic was determined using CFD and is plotted in Figure 4.1. It can be seen from the plot that a peak efficiency of 56% is achieved at a flow coefficient of approximately 0.15. This point corresponds to when the WEC operates with an optimal flow regime. The narrow efficiency band of the turbine as a function of flow coefficient can be seen in Figure 4.1.

As the flow coefficient increases from the optimal point aerodynamic stall occurs in the turbine and its efficiency rolls off significantly. Finally at lower flow rates the efficiency initially drops off slowly before a significant drop off occurs at very low flow coefficient. It can be seen from Figure 4.1 that zero efficiency does not correspond to zero flow.

At flow coefficients close to zero the efficiency of the turbine is negative due to frictional and stiction losses. This highlights the characteristic that the Wells Turbine is non-self starting. The turbine can start up under very light loaded conditions however it is essentially a non-self starting device. The turbine must therefore be spun by an external torque source up to a threshold speed before it can begin converting pneumatic power to mechanical power.

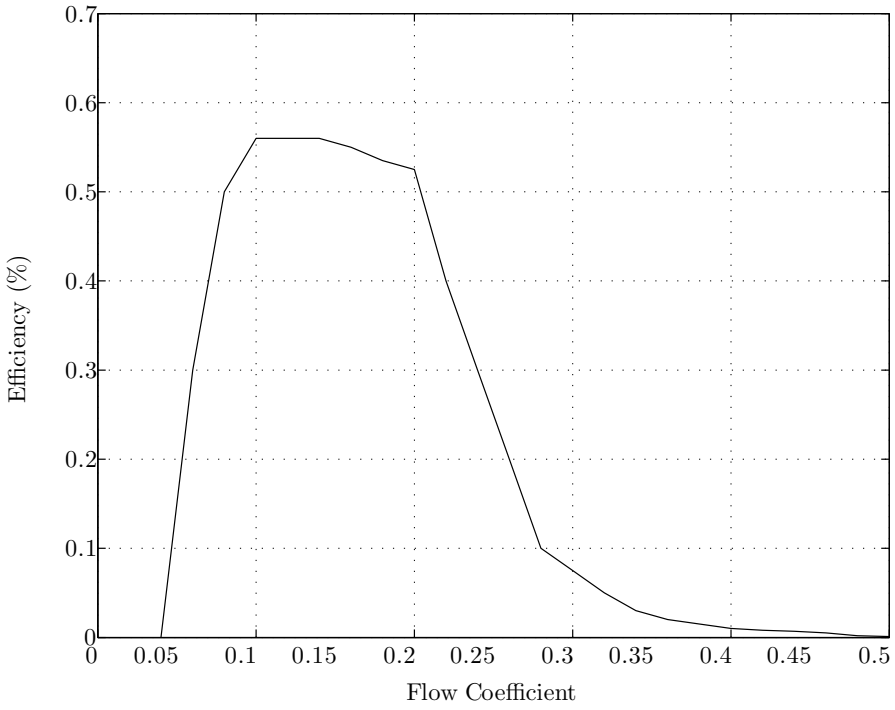

Figure 4.1: Wells Turbine Efficiency Characteristic

Taking the efficiency characteristic shown in Figure 4.1 it is possible to develop a non-dimensional torque characteristic for the Wells turbine. This characteristic fully predicts the turbine's performance from low flow rates to stall. The ND Torque equation can be derived using (4.3) by dividing above and below by the rotational speed:

$$T_{ND} = \frac{T}{\rho_a N^2 D^5} \tag{4.5}$$

where T is the turbine torque. The development of the non-dimensional torque characteristic for the Wells turbine is discussed in a later section.

4.4 Experimental Test System Description

The development of the turbine model was based on experimental data obtained from a 1:2.5 scale offshore OWC WEC located at the Irish test site. The system consists of a Wells turbine coupled to a dc electrical generator. The electrical generator output was controlled by means of a dc-dc converter and resistive load. The PWM duty cycle of the dc-dc converter was controlled to maintain the speed of the system at a specified value. The controller could only control deviation above the setpoint value and below the setpoint no control existed. Finally a load resistance is connected to the system to dissipate the electrical power generated from the system. A block diagram of the system is depicted in Figure 4.2.

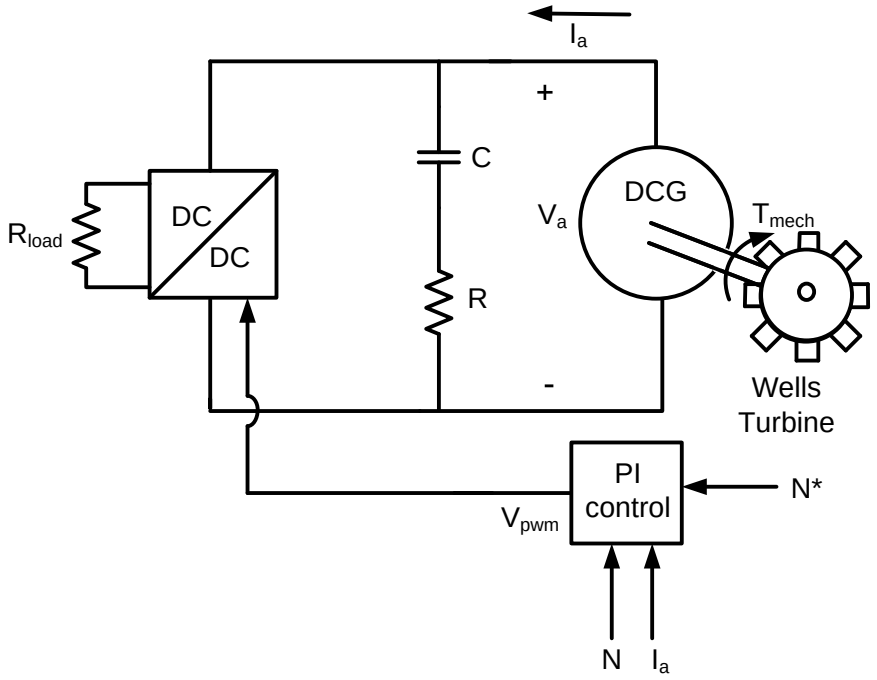

Figure 4.2: Electrical Generation System for OWC WEC

In Figure 4.2 R_{load} is the load resistance, V_{PWM} is the commanded PWM voltage to be applied by the DC-DC converter and N^* is the reference speed.

4.4.1 Acquiring mechanical torque measurement

The electrical system used was tested on-site and the key parameters of the dc generator were established. These parameters included total machine and turbine inertia, J, machine friction factor, B_m, machine constant, k_t and machine armature resistance R_a. The electrical parameters R_a and k_t were determined using through dc and no-load tests respectively. The turbine inertia was obtained through computational fluid dynamics and B_m was determined by means of a free-deceleration test.

The data acquisition system monitored machine voltage, V_a, current, I_a and rotational speed, N, at a sampling time of 0.2 s. By using these measured electrical parameters at each time interval it was possible to estimate the mechanical shaft torque delivered to the system from the Wells turbine. The mechanical torque is given by the following equation:

$$T_{mech}(t) = T_{em}(t) + T_f(t) + T_j(t) \tag{4.6}$$

where T_{em}, T_f and T_j are the generated electromagnetic, frictional and inertial torques respectively. These torques can be obtained at each time sample using the following equations:

$$T_{em}(t) = \frac{P_{elec}(t) + P_{eloss}(t)}{N(t)} \tag{4.7}$$

$$T_f(t) = B_m N(t) \tag{4.8}$$

$$T_j(t) = J\frac{dN(t)}{dt} \tag{4.9}$$

where P_{elec} is the generated output electrical power and P_{eloss} is the machine electrical losses and are given by the following equations:

$$P_{elec}(t) = V_a(t)I_a(t) \tag{4.10}$$

$$P_{eloss}(t) = I_a^2(t)R_a \tag{4.11}$$

Once the mechanical torque produced by the turbine was determined it was possible to obtain the non-dimensional torque by using (4.5). The non-dimensional torque equation can be expressed in terms of measured quantities and system parameters by using equations (4.6)-(4.11) and (4.5).

$$T_{ND}(t) = \frac{V_a(t)I_a(t) + I_a^2(t)R_a + B_m N(t) + J\frac{dN(t)}{dt}}{\rho_a N^3(t) D^5} \tag{4.12}$$

where $T_{ND}(t)$ is the non-dimensional torque determined at each sample time t.

This method is similar to the procedure used in [84, 85] to determine the non-dimensional torque.

4.4.2 Measurement of pneumatic Parameters

In a similar method to that which has been discussed for the torque, by using the measured pressure within the OWC chamber and turbine damping ratio it is possible to derive the non-dimensional flow. The pressure within the chamber was measured using a calibrated +/- 200 mbar vented guage pressure sensor and was again sampled at a rate of 0.2 s. The flow inside the chamber was derived using turbine damping from the following equation:

$$Q(t) = \frac{p_c(t)}{B_t(t)} \tag{4.13}$$

where the applied damping B_t is given by the following expression:

$$B_t(t) = \frac{2\rho_a D N(t) B_r}{A_a} \tag{4.14}$$

in which B_r is the damping ratio of the turbine and is defined as:

$$B_r = \frac{\Psi}{\Phi} \tag{4.15}$$

The damping ratio was calculated from complex fluid dynamic analysis based on turbine design specifications.

Once the flow and applied damping were determined using equations (4.13) and (4.14) it was possible to determine the flow coefficient using (4.2).

4.5 Development of ND torque profile

As has been discussed previously the Wells turbine can be modelled using an efficiency curve that denotes the regions of operation for the turbine. This can be further developed to give a non-dimensional torque profile that predicts the mechanical torque output from the turbine based on the flow conditions it experiences.

With the instantaneous non-dimensional flow and torque of the system defined from the method described in the previous section it is then possible to develop the non-dimensional characterisic curve.

Data from a commonly occurring sea state at the Irish test site was examined to determine the non-dimensional turbine data. A scatter diagram of ND torque versus flow coefficient, Φ, was determined from the sea state data.

Initially the data was seperated between inflow and outflow from the chamber based on the sign of Φ. The equations for non-dimensional quantities assume that the speed of the system was

constant and therefore the data was sorted into a series of speed bins such that the speed can be assumed to be constant. The variation of the speed in the full sea state data was in the range of 1500 RPM to 1900 RPM, However it was found that the majority of the data from the sea state was when the turbine was operating in the range of 1710 RPM to 1890 RPM. The analysis of the data within this range was carried out by dividing the data up into speed bins of 20 RPM intervals. This technique has been used previously in [87].

A family of scatter diagrams for non-dimensional torque versus non-dimensional flow for the various speed profiles were then developed. These scatter diagrams are assumed to be unaffected by changes in speed in the turbine due to the grouping of data in the speed bins.

The non-dimensional torque data was then divided into groups in intervals of 0.02 in flow coefficient. The mean of the non-dimensional torque in each group was taken. This allows for a non-dimensional torque versus flow coefficient curve to be drawn that will contain much less scatter than previously observed.

Characteristic curves of non-dimensional torque versus flow coefficient for the Wells turbine can now be seen for the different speed groupings. A sample of the results are shown in Figure 4.3 where the speed range is 1790-1890 RPM. The different colour curves in Figure 4.3 correspond to the different speed bins. Each point on the curves corresponds to a mean non-dimensional torque from the flow coefficient groups.

Some variation in the curves was still found to exist and therefore a best fit curve was produced through the points to produce the characteristic curve for the Wells turbine operation. Taking a full data set, the curve shown in Figure 4.4 was obtained.

The solid black line shows the experimental curve while the dashed red line shows the ND torque profile based on the efficiency curve in Figure 4.1. A more in-depth description of the development of the non-dimensional torque curve is presented in Appendix D.

It can be seen from Figure 4.1 that the curve that has been developed has a similar profile to that which is predicted from the CFD produced efficiency plot shown in Figure 4.1. The peak torque is predicted to occur when Φ is equal to 0.2 and after this point aerodynamic stall in the

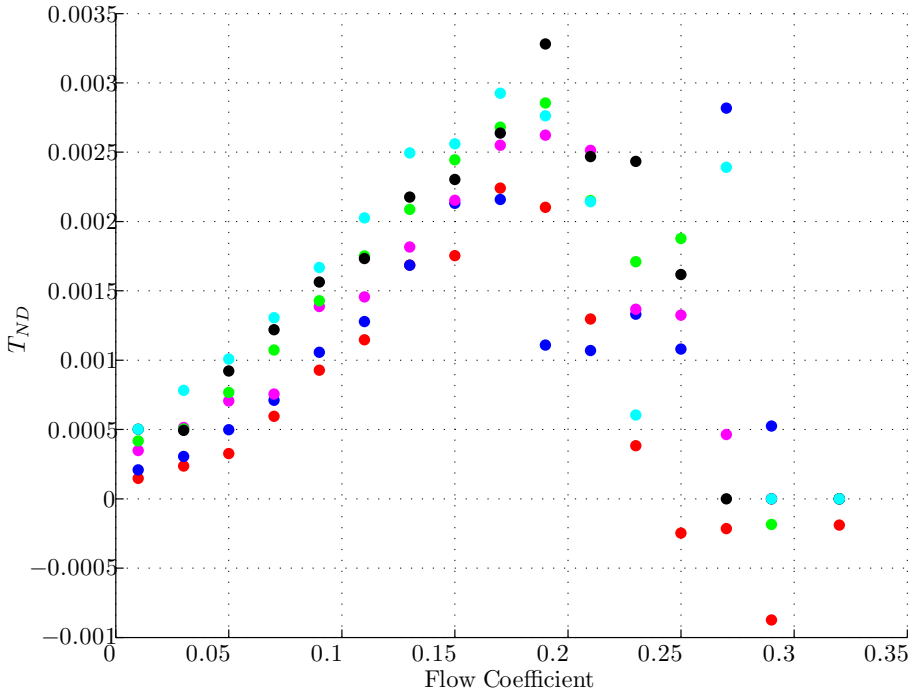

Figure 4.3: Scatter Plot of ND Torque vs Flow coefficient

turbine is predicted. Also it can be seen that at low flows a negative torque will be experienced by the turbine which is again predicted in the efficiency plot. This negative torque is due to the friction and stiction losses and demonstrates the non-self starting nature of the turbine mentioned earlier.

The scatter plot shown in Figure 4.3 and the curve fit in Figure 4.4 are for the outflow data set. A similar set of scatter plots were obtained for the inflow data and the assumption that the outflow data can be used to approximate by the inflow case is made. Hysteresis effects in the turbine are not accounted for in this characteristic curve.

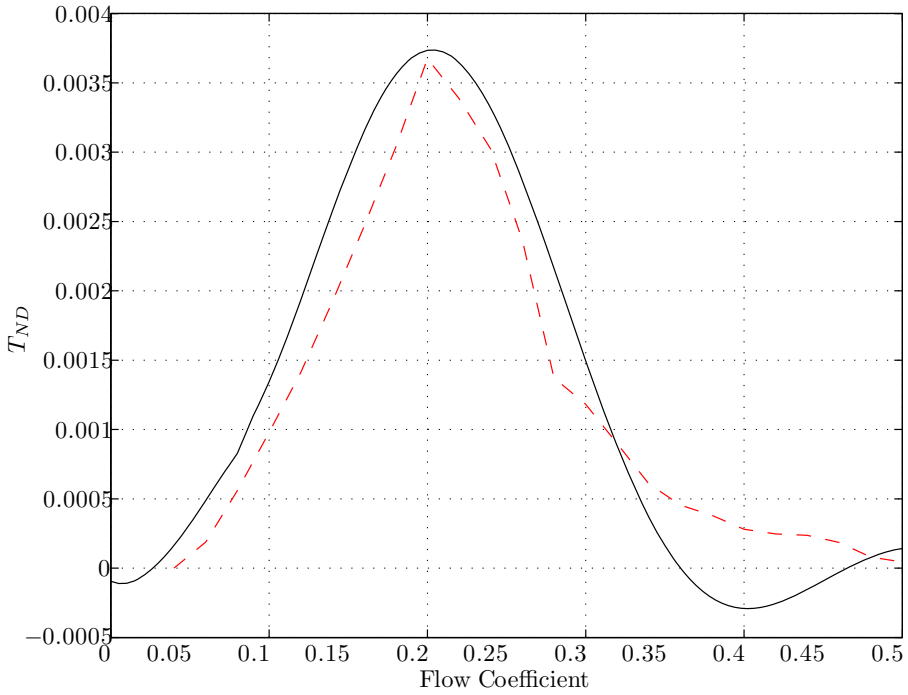

Figure 4.4: Characteristic ND Torque vs Flow coefficient curve for tested data (black) and efficiency data (dashed red)

4.6 Comparison of simulation and experimental test results

This section investigates the simulation of the electrical system shown described in Section 4.4 and the characteristic curve shown in Figure 4.4 is used to represent the Wells turbine. A block diagram of the simulation model is shown in Figure 4.5. The figure illustrates the method of obtaining the mechanical torque developed from the Wells turbine. The model takes a measured pneumatic power time series from the prototype offshore device which was recorded at the Irish test site. The airflow Q is determined by using the turbine damping B_t and from this the flow coefficient Φ can also be determined. The Wells turbine characteristic curve is then utilised to obtain the non-dimensional torque which is in turn used to determine the mechanical torque. This torque is then applied to the controlled DC generator which allows for the electrical output quantities to be

obtained. The speed of the DC generator is fed back into the turbine model for the calculation process.

The results from the 1:2.5 scale device model are then compared to actual recorded electrical data from the scale OWC WEC prototype device.

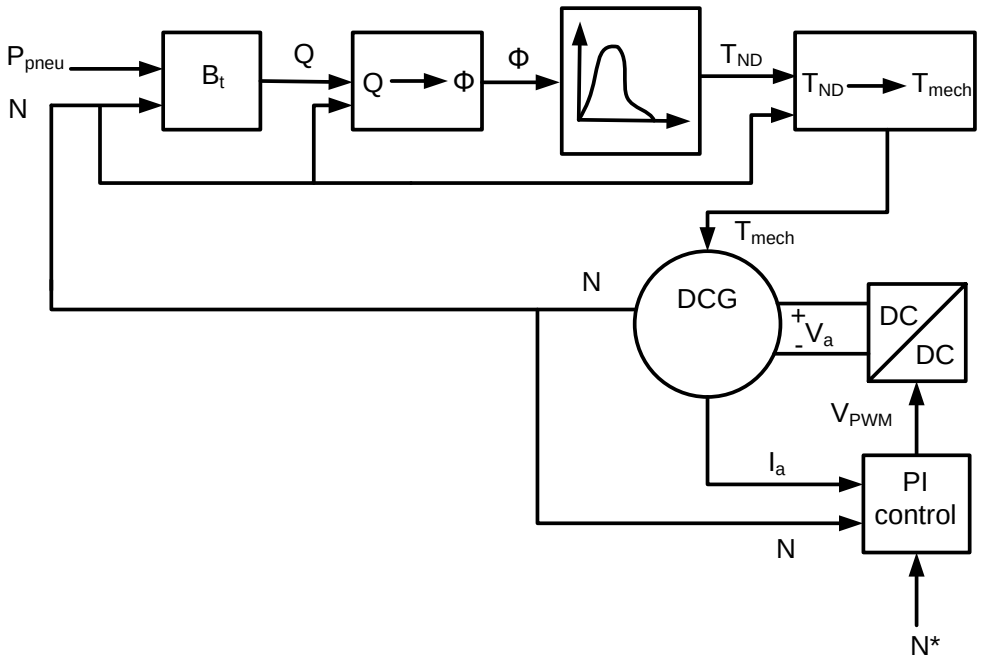

Figure 4.5: Block Diagram of Software Simulation System

The Wells turbine used in the system is a monoplane configuration and uses a NACA-015 blade profile. The PI controller in Figure 4.5 consists of a cascaded PI structure with an outer speed loop and a higher bandwidth inner current loop. The output of the PI controller provides the duty ratio for the DC-DC power electronic converter. In the simulations carried out the DC-DC converter was assumed to be ideal. This assumption was made because the losses of the converter do not affect the comparison of the simulation results and the experimental results, since electrical power is measured before the dc-dc converter.

In the study three different sea state conditions were investigated, a high power state, a medium state and a low state. The performance of the model was analysed under each of the three condi-

tions. The plots used to demonstrate the results are all given on a per unit basis.

4.6.1 High power sea state

The pneumatic power profile applied to the model is shown in Figure 4.6. This profile is a higher power profile at the location where the device is situated. The ratio of the maximum peak power to the average sea state power is 11.62.

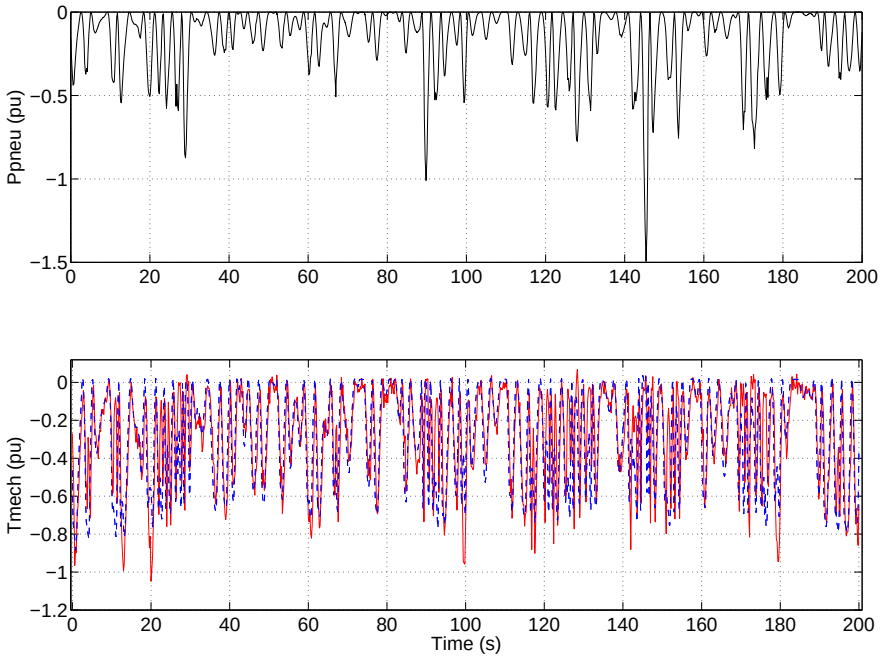

Figure 4.6: pneumatic power profile with simulated (blue dashed) and measured (red) torques for high level sea state

The mechanical torque produced by the Wells turbine is also seen in this plot. The simulated torque (dashed line) is seen to track the measured torque (solid red line) with a reasonable level of accuracy.

The stall region of the turbine can be shown in more detail in Figure 4.7 and this highlights that the model predicts this region of operation with a satisfactory degree of accuracy within the limits

of the data sampling. The sampling rate of the system was 0.2 s and it can be seen that a higher sampling rate would have led to an increased correlation between the measured and simulated plots. Thus some of the error seen in the system can clearly be attributed to the sampling rate.

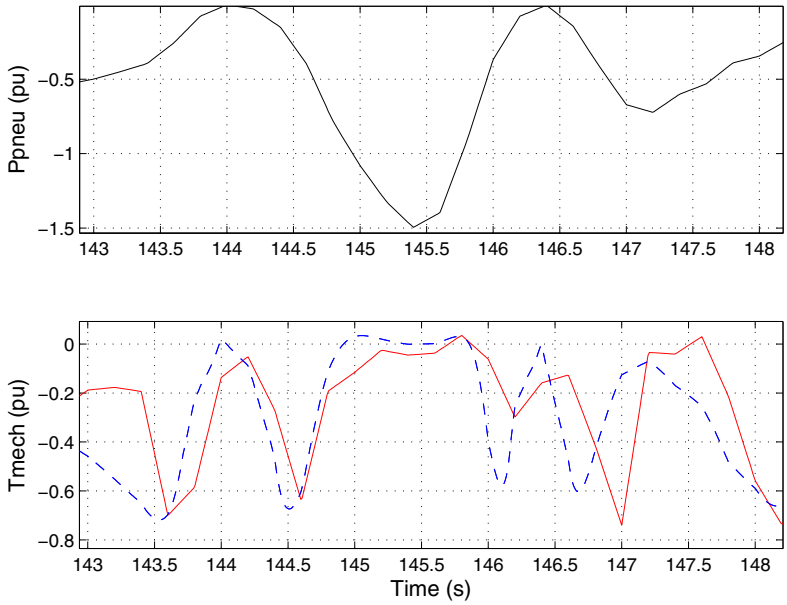

Figure 4.7: Examination of stall charcteristic of Wells turbine with simulated (blue dashed) and measured (red) torques

Figure 4.7 shows that a large pneumatic power was experienced between 144 s and 146.5 s leading to severe stall occurring in the Wells turbine. This is demonstrated by the large drop off in mechanical torque measured from the system as seen in the figure.

A histogram of occurences of error between predicted torque and measured torque is shown in Figure 4.8. This plot shows the per unit torque errors and the occurrences of these errors which help indicate the degree of accuracy of the model.

It can be seen that errors of between $\pm$ 0.05 per unit(pu) torque occur most frequently and that error of between $\pm$0.05 and $\pm$0.1 pu occurring half as frequently. It can also be seen that as the degree of error increases then the occurrances of these errors drop off significantly. The model is

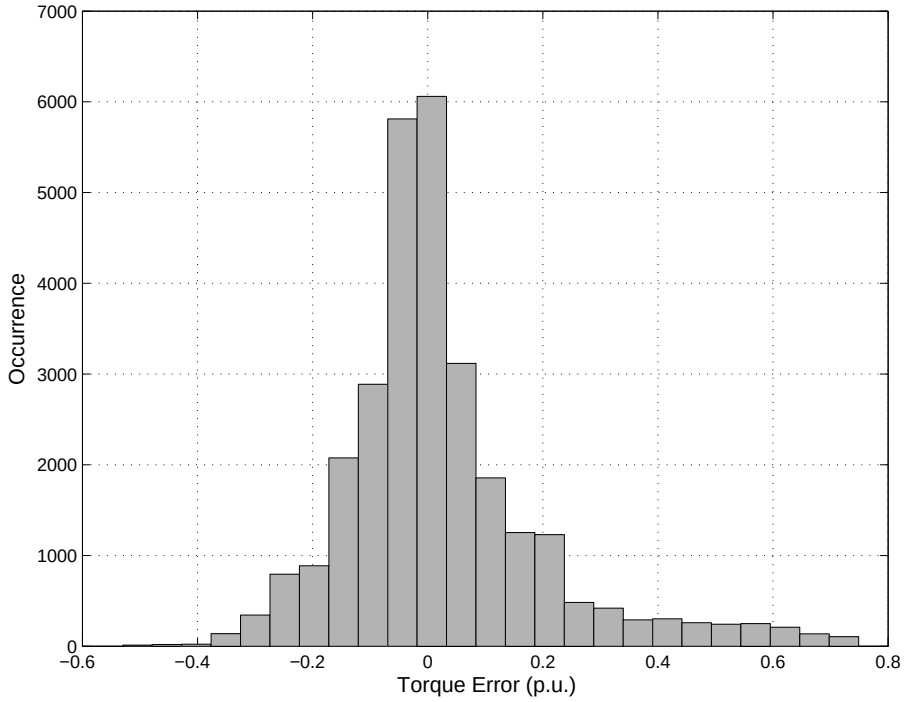

Figure 4.8: Histogram of occurences of error between simulated and measured torque

therefore seen to perform to a satisfactory level accuracy over the simulation time considering the assumptions made.

The occurrences of error in the model can be attributed to a number of factors. One of the reasons for instantaneous errors occurring is due to a phase difference between the measured and simulated torques. This can be seen in Figure 4.7 where the measured torque (solid red line) lags the simulated torque. This phase difference has been introduced by the fact that the model is first-order and does not take into account higher order aerodynamic effects, for example compressibility of air and hysteresis in the turbine.

Hysteresis is particularly an issue during stall and also when the airflow is changing from an accelerating flow to a decelerating flow. It can be seen in Figure 4.3 that after the peak torque point the curve becomes more scattered. The scattering in the stall region can be attributed to hysteresis effects where there is a loop in non-dimensional torque versus flow coefficient. The degree of the

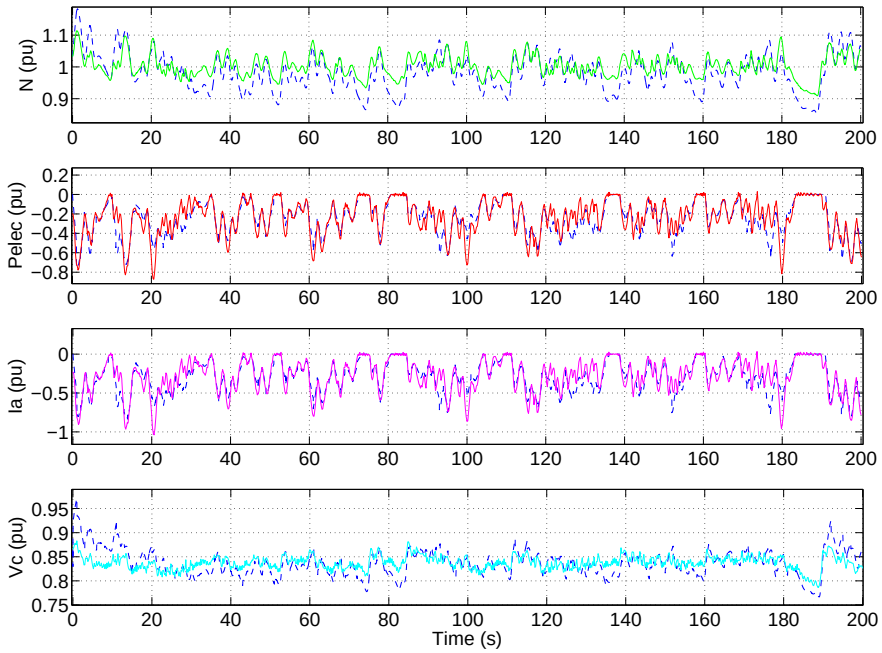

Figure 4.9: Electrical parameters simulated (blue dashed) and measured (green,red,magenta,cyan) for high level sea state

hysteresis and the size of the loop are dependant on the rate of change of the flow [85, 87]. The hysteresis in this region implies that at a particular flow coefficient the non-dimensional torque may have several values and this contributes to the scattering of points in Figure 4.3 beyond the peak torque. This scatter highlights the difficulty in pedicting the exact non-dimensional torque at given instances when the turbine enters the stall region.

Also the differences in device performance on inflow and outflow would affect the models accuracy particularly in the stall region. Differences in the device damping and performance curves can exist between inflow and outflow and this variation has not been modelled in the characteristic curve.

Another cause of inaccuracy that should be noted is that this curve was formulated by taking a mean torque at each flow coefficient which will lead to imprecision in prediction of instantaneous

torque. There is also imprecision caused due to the sampling rate in the device this can be seen clearly to have an effect on the models accuracy in Figure 4.7. Also the fact that a differentiaion of the speed signal is required when determining the inertial torque leads to errors in the measured torque.

Considering the assumptions mentioned, the time series data and the error occurence histogram, the accuracy of the torque prediciton is seen to be of a reasonable level.

Further analysis of the system performance is also seen to be reasonable to a first-order approximation with the model seen to predict speed, generated electrical power, armature current and voltage quite accurately throughout. This data can be seen in Figure 4.9.

The figure shows the simulated data in the blue dashed curve while the measured data for speed is in green, generated electrical power is in red, armature current is in magenta and voltage is in cyan. The simulated results are seen to track the experimental results with reasonable accuracy and provide an acceptable representation of the actual systems performance.

4.6.2 Medium power sea state

In order to investigate the accuracy of the model under various sea state conditions further inveti-gation of the expeimental sea state data set was carried out. The following sea state has a power level of medium intensity for the test site with a peak to average ratio of 12.7. This profile would be of medium level in its intensity. Figure 4.10 shows the pneumatic profile applied in this case along with the predicted and measured mechanical torques.

The figure again shows that the model can predict the torque generated by the turbine to a sufficient level of accuracy. As before, certain inaccuracies exist in the prediction of torque due to unmodelled aerodynamic effects. For example, inaccuracies in the torque predictions can be seen between 80 and 90s and also between 120 and 140s. The model is seen to overestimate the torque provided by the turbine and this is due to difficulties in accurately predicting the torque in the stall region as mentioned earlier.

The prediction of electrical parameters was also found to be reasonably accurate. These results

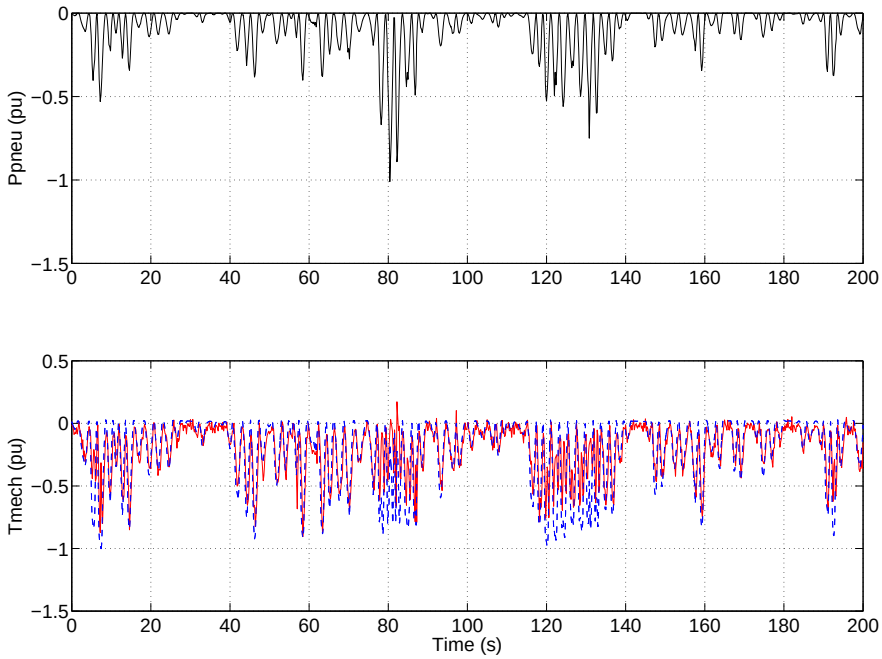

Figure 4.10: pneumatic power profile with simulated (blue dashed) and measured (red) torques for medium level sea state

are shown in Figure 4.11. The overestimation of the mechanical torque between 80 s and 90 s and also between 120 s and 140 s in Figure 4.10 can be seen to directly affect the prediction of generated electrical power in Figure 4.11 with the model overestimating this quantity. Overall the performance of the model is seen to be reasonably accurate and are in line with the results shown for the high power sea state.

4.6.3 Low power sea state

The final sea state that is tested is a low power sea state. This sea state has a peak to average ratio of 11.3. The pneumatic profile of the sea state along with the turbine torque response in this case is shown in Figure 4.12.

The results for the electrical measurements are illustrated in Figure 4.13. The results can again

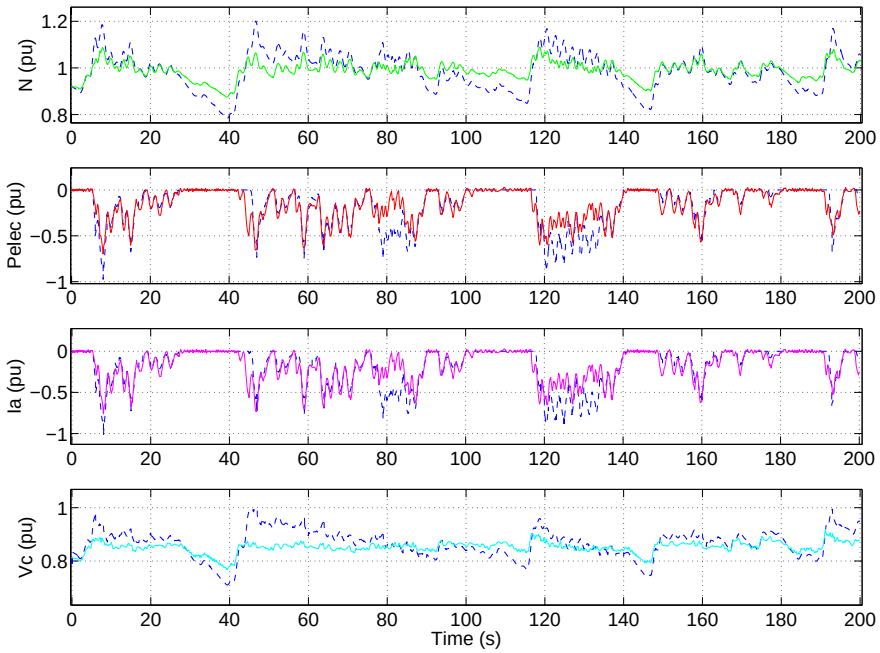

Figure 4.11: Electrical parameters simulated (blue dashed) and measured (green,red,magenta,cyan) for medium level sea state

be seen to have a reasonable level of accuracy in this sea state taking into account the simplicity of the model. In this sea state, noise on measurements undoubtedly contribute more to inaccuracies. An example of this noise can be seen in the torque plot of Figure 4.12 where spikes in the measured torque are seen. This is due to the time derivative of speed that is used in the calculation process for mechanical torque.

These results over various sea states highlight that the characteristic curve developed in this chapter provides a very simple approximate, yet appropriate model for the Wells turbine despite yet all of the simplifying assumptions. The OWC WEC can therefore be modelled with a reasonable degree of confidence.

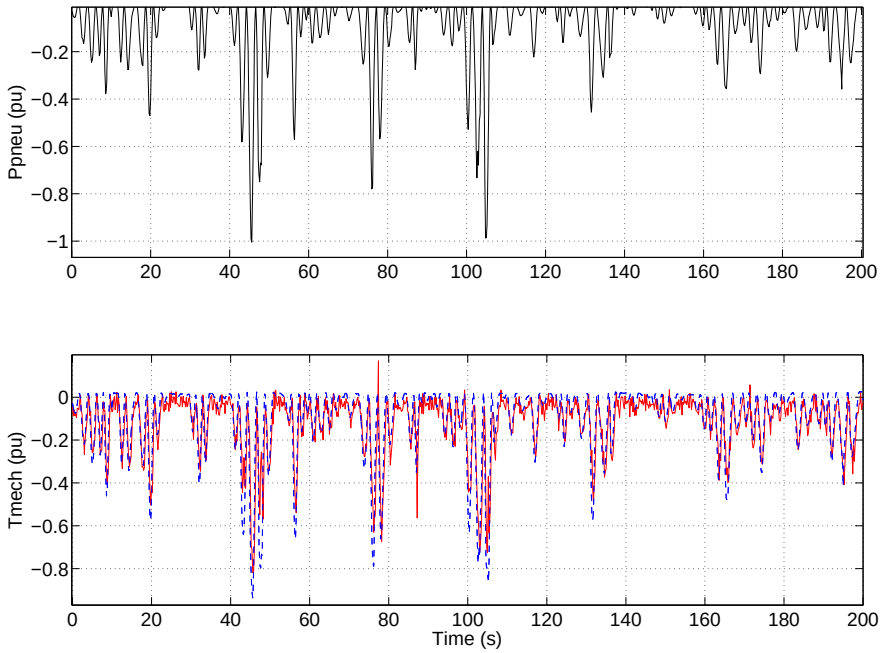

Figure 4.12: pneumatic power profile with simulated (blue dashed) and measured (red) torques for low level sea state

4.6.4 Comparison of energy data

A final test and vindication of the model was to analyse the predicted and measured electrical output energies on a per unit basis. These results are shown in normalised form in Table 4.1.

Table 4.1: Generated electrical energy for various sea states

State	High	Medium	Low
Sim. E_{elec} (p.u.)	1.0	0.67	0.14
Meas. E_{elec} (p.u)	0.89	0.58	0.17

The prediction of electrical energies quantifies the level of accuracy of the model of the system over a period of time. The results shown in Table 4.1 demonstrate that the model can predict the electrical energy generated from the system to within 20% of the actual experimental value. Differences between these values can be put down to the simplifying assumptions mentioned earlier

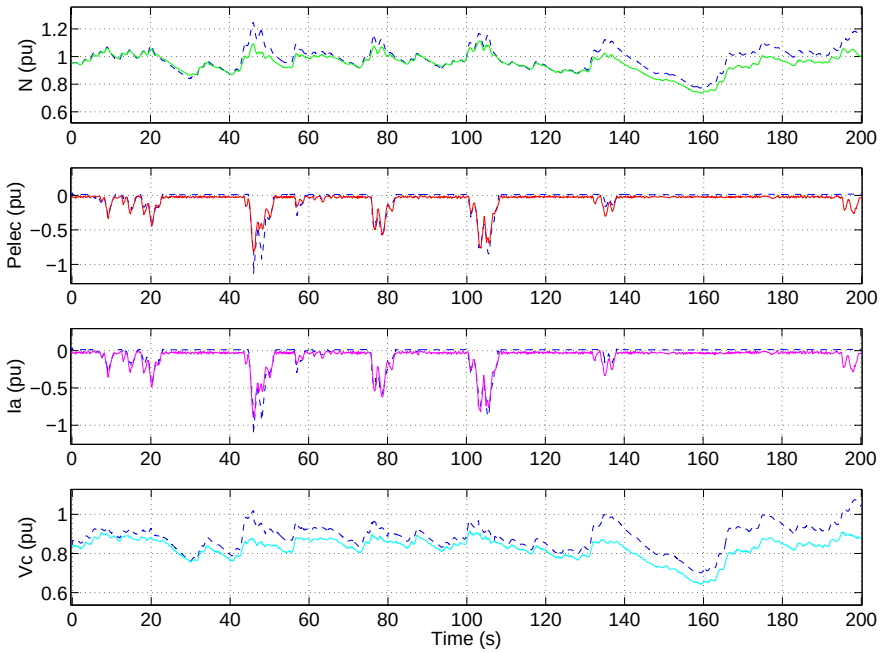

Figure 4.13: Electrical parameters simulated (blue dashed) and measured (green,red,magenta,cyan) for low level sea state

coupled with inevitable experimenal errors. Examples of such error are in measuring machine frictional coefficient, B_m, inertia, J and also noise that is introduced due to the time derivative of speed which is used in the calculation process.

Improvements in the model and its performance could be achieved by considering the differences in inflow and outflow in the device. As has been mentioned different turbine damping exists depending on the intake of air or exhaust of air from the column. This has been investigated in previous studies such as [84, 85] and could be considered in future work on this model. The model could for example, contain two seperate non-dimensional torque curves with one for the inflow case and the other for the outflow case.

Furthermore the effect of hysteresis in the stall region could also be considered. Hysteresis is a difficult aspect to model without increasing the complexity of the model as the degree of hysteresis

is dependant on the peak pressures experienced. By accounting for differences in accelerating and decelerating airflows improvement in the accuracy of the model may also be achieved [87]. Taking all of these effects into account would improve the accuracy of the turbine model presented.

Whilst a certain degree of error exists in the model the results obtained gives a satisfactory level of prediction of system performance and the model is found to compare favourably with work that has previously been presented on OWC modelling such as in [83].

4.7 Conclusion

The oscillating water column (OWC) wave energy converter (WEC) is the most advanced wave energy device to date. The device utilises a bi-directional air turbine to convert pneumatic power to mechanical power. The testing and experimental validation of a model for a Wells turbine coupled to a dc generator for a 1:2.5 scale offshore OWC WEC prototype is presented. The theory behind the operation of the Wells turbine is discussed initially and this theory is then used to model the system. Actual test data from an experimental 1:2.5 scale prototype device was used to develop a characteristic curve for the performance of the turbine.

A model of the system was developed and the simulated results from this model were compared with actual experimental data from the system for validation purposes. The model was tested under three different types of sea conditions, one of high power density, one of medium power density and one of low power density. Despite simplifying assumptions and experimental error the model was found to predict the mechanical and electrical performance of the system to a satisfactory level of accuracy. This was further demonstrated by examining the measured and predicted electrical energies. Analysis of the model over the three different sea states allowed for confidence in the accuracy of the model over a range of sea conditions to be developed.

One of the main sources of error was due to the sampling of the system and improvement in the model predictions could be made by increasing the sampling rate. Another major source of error was due to simplifying assumptions made in the development of the model. The model was a first-

order model and did not consider higher order aerodynamic effects. Other effects such as turbine hysteresis, differences in accelerating and decelerating flows and differences in damping of the column during inflow and outflow were not considered in the existing model. Future work could be carried out in refining the model and improving its accuracy by taking into account turbine hysteresis and also the different flow regimes that occur in both inflow and outflow conditions, albeit at the increase of complexity.

The existing model is satisfactory in its accuracy and compares well with similar models developed in other studies. The developed model could be used to analyse the system as a whole predicting results from pneumatic power to generated electrical power. The turbine model could be used to aid in electrical system design and testing for the OWC WEC application.

5

Electrical Machine Rating and Thermal Analysis through Simulation

5.1 Introduction

Considerable challenges exist for the electrial conversion system in an offshore OWC WEC. Some of the key problems faced are the oscillatory nature of the power profile of the sea and also the harsh conditions that exist in this environment. The fundamental difference between wind power generation and wave power generation exists in the profile of the power supplied to the device. In the case of wind energy there are variations in power around a mean value due to gusts in wind speed. Conversely, in the case of the pneumatic power produced by the OWC WEC, the profile is

oscillatory and varies between a maximum value to zero twice every wave cycle. This means that the peak-to-average ratio of power in the OWC WEC case is much higher than a wind application.

These high pulsations of power lead to challenges for the electrical system including electrical machine selection and rating. Generator selection has been investigated in [28]. The paper discusses the challenges faced for each generator type. The generators investigated include the synchronous generator (SG), the squirrel-cage induction generator (SCIG), the doubly-fed induction generator (DFIG) and the permanent-magnet ac generator (PMAC).

In previous shore-based OWC devices a wound-rotor induction generator (WRIG) has been used, [19–21]. In [19] the WRIG is operated with an inverter-fed stator and a rotor configured with a variable external resistance. The rating of the machine was chosen conservatively and this caused a significant overrating of the machine with respect to the electrical power actually being handled.

In [21] a WRIG is used in a doubly-fed induction generator (DFIG) configuration. The rotor-side converter is rated at 100% of the rated machine power allowing for the machine to run in super-synchronous mode at double the synchronous frequency. This allowed for a 200 kW rated machine to operate and handle the peak mechanical shaft power delivered from the OWC WEC of 525 kW.

This chapter investigates the application of the 30 kW Marelli induction machine to an offshore OWC WEC through simulation. The sea state data from the previous chapter is scaled up to determine the OWC WEC device rating that can be used with the 30 kW Marelli machine studied earlier in the thesis. The motivation of the study is to determine the device rating that the Marrelli DFIM can operate with before it becomes thermally stressed.

The 30 kW machine is operated in two modes: (1) a volts-hertz controlled inverter-fed stator with rotor-shorted configuration and (2) a vector controlled doubly-fed inverter configuration. The latter configuration is denoted DFIG and the former is denoted SCIG as it resembles a classical squirrel-cage induction generator when the rotor is shorted.

Thermal modelling of the two machine configurations is carried out when the machines are

subjected to the torque pulsations from a high-power-density sea state. Simulations of the two configurations are carried out to determine the overall temperature rise in the system. This temperature rise is used to determine the OWC WEC rating which is compatible with the 30 kW machine. The study therefore gives an insight into the elecrical device ratings for an OWC WEC application.

5.1.1 Thermal modelling procedures overview

A first-order lumped parameter thermal model is used in the analysis of the machine based on the model presented in [90]. The first-order model is suitable for systems where start-up losses do not have a large impact on the overall losses measured for the system operation. The effective thermal time constant was determined by taking the best fit to the thermal rise curve for the different modes of operation. Therefore the thermal time constant should be chosen depending on the machine loading and operation time. A second-order model was introduced to take into account the start-up thermal losses when start-up conditions are found to influence overall temperature rise.

More detailed thermal models for induction machine analysis exist which consist of multiple lumped thermal resistances and thermal capacities. In [91–93] complex thermal models containing a large number of thermal elements were used to represent the thermal performance of totally enclosed fan cooled (TEFC) type induction machines. In [91] a commercial software package that takes in parameters such as machine geometry was used to compile a thermal model that contains thermal resistances, capacitances and thermal heat sources. The software models developed were then compared to experimental tests carried out on the machines.

The results from the standard commercial package were enhanced by considering more complex issues such as convection cooling from the housing, airgap heating, end space cooling and heat transfer through element interface gaps. Computational fluid dynamics (CFD) used in the software package were used in conjunction with experimental data to improve the thermal predicitons, [92]. CFD was found to be a useful tool in predicting fluid flow around the machine.

In [93] the calibration of thermal models for the induction machine is investigated. Issues such as thermal parameter sensitivities and their overall influence on the thermal model are examined. It was found that housing finish and fin channels are the areas most sensitive to affecting the thermal operation of the machine. It is therefore important to have more information on these areas to ensure accuracy in the results.

Finite element analysis (FEA) methods are popular for determining the thermal performance of induction machines. FEA is useful in predicting the thermal conductivity through solid elements in the machine. However, these methods generally involve complex calculation procedures. Examples of some of the methods used are given in [94–96].

More simplified lumped parameter models are presented in [97, 98]. In these papers, the number of thermal resistances were reduced to represent the major thermal paths in the machine such as stator windings, stator teeth, rotor-to-airgap resistance and shaft resistance. The simplifications allowed for the machine to be modelled as a series of hollow cylindars where thermal resistances exist for heat transfer in the radial and axial directions.

The model presented in [97] was a 15-node thermal model comprising of 8 differential equations. From these differential equations the thermal resistances and capacitances are determined. All thermal resistances are determined using machine dimensions, physical properties and heat transfer data. The only thermal quantity determined by test is the ambient thermal resistance.

In [98] the model presented in [97] was simplified further by neglecting thermal capacities. This model is used to calculate the over-temperature of the machine in steady state. However, utilising this simplified model in a transient situation may cause inaccurate results to be obtained.

Further simplification of the induction machine thermal model to a Π-equivalent circuit containing thermal resistances and capacities is presented in [99, 100]. The model used in both papers is a three-node model consisting of stator and rotor conductances and capacitances, a common conductance between the stator and rotor and two heat sources based on stator and rotor losses. This Π-equivalent model allows for the temperature rise of the machine to be determined but does not allow for specific hot-spot temperatures to be determined.

The procedure required to determine these thermal equivalent parameters for the thermal model is presented in [100]. The method includes two DC tests, blocked rotor tests and two load-tests at different frequencies. The two DC tests are used to determine the standstill conductances for the machine. The locked-rotor tests are carried out at two low-frequency points. The results from these tests are used with the standstill conductances to determine the iron and hysteresis loss factors for both the stator and the rotor. Finally, the variation coefficients are determined for the machine at different rotational frequencies. With all the parameters determined the Π-equivalent circuit model can be finalised.

For the study carried out in this chapter, a first-order thermal model is sufficient as the average temperature rise of the machine over a time period is required to illustrate the machines performance under the pulsating load. The thermal model is developed using the datasheet information provided on the Marelli machine. Hot-spot temperatures and specific temperature rises in particaular machine components are not considered. The analysis aims to give a general insight into the required machine ratings for a typical high energy sea state.

5.2 Thermal modelling

The electrical machine used for this study is the 4-pole 30 kW, 50 Hz wound-rotor induction machine, from Marelli with machine number E4F225MA, as presented earlier, [64]. The thermal model for the machine is represented as a first-order thermal model based on an equivalent RC circuit, [90]. A schematic diagram of the model is shown in Fig. 5.1 where Q_{Th} is the equivalent thermal heat source which is equal to the machine power losses, R_{Th} is the equivalent lumped thermal resistance and C_{Th} is the equivalent lumped thermal capacitance. The extra branch containing the cooling heat source Q_c is used to model forced cooling in the machine. Forced cooling was not considered in this study and therefore that extra branch can be neglected.

The equivalent parameters are determined by investigating the thermal information given on the machine in the data sheet, [64]. The machine has an IEC thermal class F rating meaning

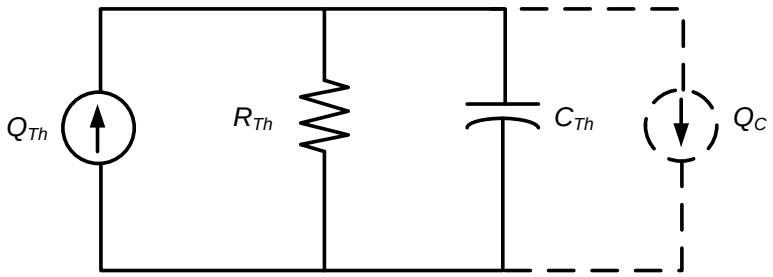

Figure 5.1: First-order thermal model.

that the maximum temperature rise allowed for the machine is 105-110^{o}C, [101]. The datasheet outlines the machine ratings for different modes of operation based on the IEC standard 60034-1, [102]. The data used for determining the thermal parameters of the machine is summarised in Table 5.1.

Table 5.1: Duty cycle data for E4F 225 MA induction machine

Duty	Output (kW)	Time Functioning (mins)	$\eta(\%)$
S1	30	Continuous	91
S2	40	30	91

Duty cycle S1 is defined as constant load for a duration that achieves thermal equilibrium. Duty S2 is defined as operating at constant load for a period of time lower than achieving thermal equilibrium followed by a rest period of sufficient length to re-stabilise the machine thermal equilibrium at ambient temperature. Ambient temperature for all duties is assumed to be 40^{o}C as specified in the IEC standard.

5.2.1 Determining thermal resistance

The first step in determining the first-order lumped-parameter model in Figure 5.1 is to determine the thermal resistance. The thermal resistance of the machine is given by the following expression, [103]:

$$R_{Th} = \frac{\Delta\theta}{P_{loss}} \tag{5.1}$$

where R_{Th} is the thermal resistance, $\Delta\theta$ is the change in machine temperature and P_{loss} is the electrical power losses in the machine and is analogous to Q_{Th} from Figure 5.1.

By taking the data for duty cycle S1 and noting that the change in temperature to reach thermal equilibium is 110^oC. The calculation of the thermal resistance is given below.

$$R_{Th} = \frac{110}{(1-0.91)\,30 \times 10^3}$$

$$R_{Th} = 0.0407\,^oC/W \tag{5.2}$$

5.2.2 Determine thermal capacity and time constant

By using the result for thermal resistance obtained above with the data for duty S2 given in Table 5.1 it is possible to determine the thermal time constant of the machine.

By rearranging equation (5.1) the following equation can be determined for the maximum temperature of the machine under a continuous load:

$$\theta_{max} = P_{loss}R_{Th} + \theta_{amb} \tag{5.3}$$

where θ_{max} is the maximum temperature and θ_{amb} is the ambient temperature. Using the data from duty S2 it can be shown that the maximum temperature under a continuous 40 kW load is 187^oC as shown below:

$$\theta_{max} = 0.0407\left((1-0.91)\,40 \times 10^3\right) + 40$$

$$\Theta_{max} = 187\,^{o}C$$

The expression for temperature rise in a heated body is given by the following expression:

$$\Delta\theta(t) = \Delta\theta_{max}(1 - e^{-t/\tau}) \tag{5.4}$$

where $\Delta\theta(t)$ is the temperature rise at time, t, $\Delta\theta_{max}$ is the maximum temperature rise and τ is the thermal time constant.

Rearranging equation (5.4) gives the following expression for thermal time constant, τ:

$$\tau = \frac{-t}{ln\left(1 - \frac{\Delta\theta(t)}{\Delta\theta_{max}}\right)} \tag{5.5}$$

Using the data for duty S2 from Table 5.1 with the maximum temperature value from above and noting that $\Delta\theta(t)$ is given as 110 ^{o}C the thermal time constant is determined below:

$$\tau = \frac{-1800}{ln\left(1 - \frac{110}{187-40}\right)}$$

$$\tau = 1298.43\,s^{-1}$$

The thermal capacity can be determined from the following expression and the value of this parameter was 31.9$\times 10^3$ J/^{o}C.

$$\tau = R_{Th}\,C_{Th} \tag{5.6}$$

A summary of the thermal parameters for the 30 kW induction machine can be seen in Table 5.2.

With the values of thermal resistance and capactiance determined for the machine it is possible to carry out a first-order thermal analysis of the machine.

Table 5.2: Calculated thermal parameters for E4F 225 MA induction machine

R_{Th}(^{o}C/W)	θ_{max}(^{o}C)	τ(s)	C_{Th}(J/^{o}C)
0.0407	187	1298.43	31.9×10^3

5.3 Wave energy converter and sea state scaling

The oscillating water column (OWC) wave energy converter (WEC) and high-density sea state data presented in the previous chapter are used in the study of the transient power capability of the system in this chapter. The characteristic curve developed in the previous chapter is used to represent the Wells turbine in the simulations in this chapter.

The original measured sea state data corresponds to a 1:2.5 scale device. In order to determine the size of device that the 30 kW induction machine is capable of operating with, it is required that a scaling function is used. A method known as Froude scaling can be used to scale the dimensions, pneumatic power and rotational speed of the device to allow for a consistent analysis at different scales.

Froude scaling allows for physical quantities to be scaled so that a common ratio exists between a full-scale prototype and a scaled model [104, 105]. The scale factor is given by the following relationship between the scales of the prototype and the scaled model:

$$\mu = \frac{Scale_{m1}}{Scale_{m2}} \tag{5.7}$$

where μ is the scaling ratio, $Scale_{m1}$ is the scale of the original model and $Scale_{m2}$ is the scale of the desired model. The theory behind this is explained in Appendix E.

Physical quantites can then be scaled according to the scaling ratio. Table 5.3 gives the scaling ratios for some basic physical quantities.

Using the scaling factors of the above physical quantities it is possible to develop scale ratios for the quantities that are related to the Wells turbine and OWC WEC. The turbine related

quantities are shown in Table 5.4.

Table 5.3: Froude scaling ratios for selected physical quantities

Quantity	Scaling Ratio
Length (m)	μ
Volume (m^3)	μ^3
Mass (kg)	μ^3
Time (s)	$\sqrt{\mu}$
Velocity ($m.s^{-1}$)	$\sqrt{\mu}$
Acceleration ($m.s^{-2}$)	1
Force (N)	μ^3
Power (W)	$\mu^{3.5}$

Table 5.4: Froude scaling ratios for OWC WEC and turbine related quantities

Quantity	Scaling Ratio
D (m)	μ
A_a (m^2)	μ^2
N ($rad.s^{-1}$)	$\mu^{-1/2}$
J ($kg.m^2.rad^{-1}$)	μ^5
T (Nm)	μ^4
ρ_a ($kg.m^{-3}$)	1
p_c (Pa)	μ
Q ($m^3.s^{-1}$)	$\mu^{2.5}$

D is the turbine diameter, A_a is annular area, N is rotational speed, J is inertia, T is torque, ρ_a is air density, p_c is chamber pressure and Q is axial flowrate.

The non-dimensional quantities such as Φ and T_{ND} are unaffected by the scaling ratio as they have no physical units associated to them. This allows for the non-dimensional curve developed in the previous chapter to be used at any scale.

5.4 Electrical system

The 30 kW induction machine was employed as the generator in the modelled WEC system. Two generator configurations were investigated, a Volts/Hertz (V/Hz) controlled squirrel-cage induction generator (SCIG) and a vector-controlled doubly-fed induction generator (DFIG). The SCIG topology was realised by short-circuiting the rotor coils.

Both topologies were controlled to operate at a specified fixed speed to ensure that the pneumatic power series used in each case was consistent with the series used in the previous chapter. Fixed rotational speed also ensured that the mechanical power supplied to the generator shaft from the turbine was consistent in both cases. The non-dimensional torque versus flow coefficient curve is dependant on rotational speed and therefore to ensure consistent results across both topologies a fixed rotational speed set.

The electrical losses in each topology were used as inputs to the thermal model developed earlier to determine the temperature rise of the machine over the simulation period.

Each of the generator topologies are explained in more detail below.

5.4.1 V/Hz Controlled Squirrel Cage Induction Generator

A common application of the SCIG is to operate it in variable-speed mode by using a back-to-back ac-dc-ac power electronics converter and controller. This generator topology is shown in Figure 5.2.

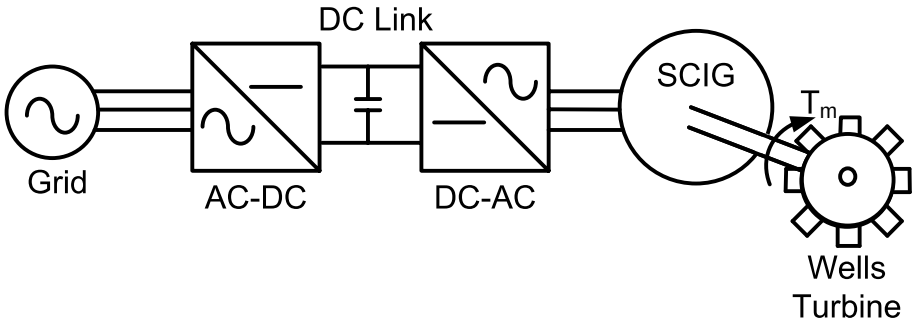

Figure 5.2: Volts/Hertz controlled squirrel cage induction generator configuration.

The V/Hz controller operates on the fact that the speed of the SCIG can be controlled by varying both the voltage and frequency of the supply voltage in a fixed ratio. In order to produce the most efficient operation of the machine and to avoid saturation, the flux density in the machine is kept constant at its rated value. This is achieved by using a linear volts-to-Hertz (V/Hz) relationship. The V/Hz law used in this paper is based on the theory presented in [106]. The slope of the V/Hz linear relationship is given as:

$$Slope = \frac{V_{s-rated} - R_s I'_{r-rated}}{f_{rated}} \tag{5.8}$$

where V_s is the stator voltage, I'_r is the referred rotor current and f is the supply frequency. A voltage boost factor is also included for operation at low frequencies in order to overcome resistance voltage drop effects. This boost factor is added to the voltage obtained from the V/Hz slope factor and is given by:

$$V_{boost} = R_s \left(\frac{T_{em}}{T_{em-rated}} \times I'_{r-rated} \right) \tag{5.9}$$

The concept of the V/Hz controller is depicted in Figure 5.3. In this figure the torque-versus-speed curve for the induction machine is shown for two different supply frequencies. The curve $T_{em}(f_0)$ shows the torque profile for a supply frequency of f_0. The corresponding synchronous frequency is denoted ω_{syn0}. If a torque T is applied to the machine the rotational speed of ω_{r0} occurs in the machine with a slip frequency of ω_{slip0}. If a rotational speed of ω_{r1} is required at the same operating torque the supply frequency needs to be increased to f_1. This gives the torque profile labelled $T_{em}(f_1)$. The corresponding synchronous and slip frequencies are denoted ω_{syn1} and ω_{slip1}, respectively.

Various desired machine rotational speeds can therefore be achived using the V/Hz control law providing the desired voltages and frequencies remain below the rated values that correspond to

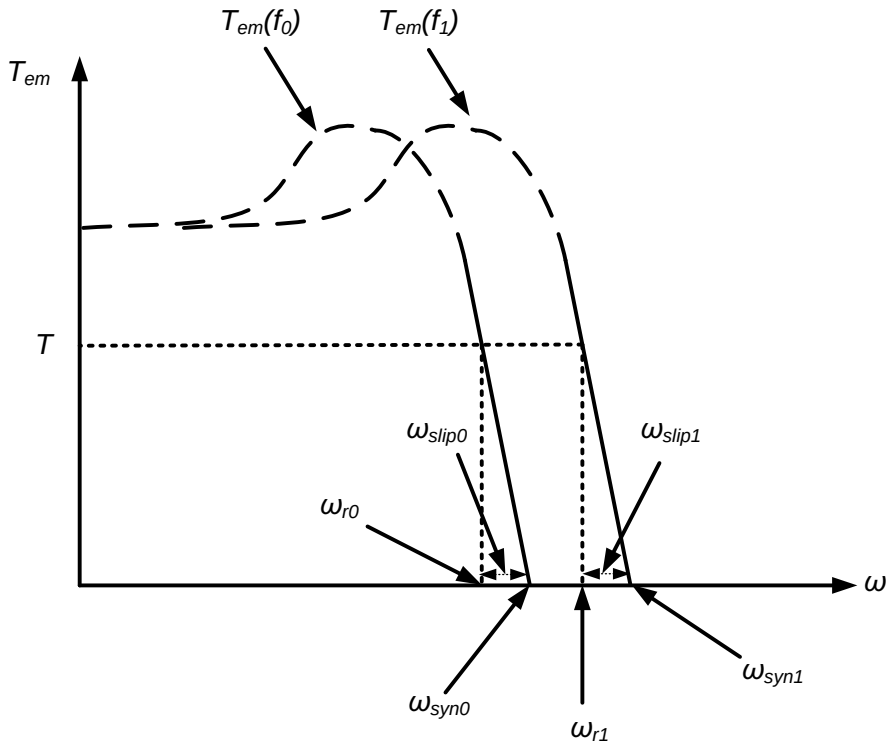

Figure 5.3: Torque-versus-speed curve under Volts/Hertz control.

the rated magnetic flux density. Beyond the rated values the machine will become saturated which is undesirable.

The controller structure contains a PI speed error loop followed by the V/Hz command law. The speed is measured and compared to the reference value with this error equal to the desired slip of the machine. This error is then added to the current rotational speed value to obtain the input value to the V/Hz equation. A block diagram of this is shown in Fig 5.4.

In the model presented in this chapter only the machine side converter and control were taken into account, and the grid side converter and DC-link controller were not considered. The power electronics converter was modelled as an ideal device with losses in the converter being neglected. These assumptions were made because only the losses within the machine and therefore its rise in temperature were of interest.

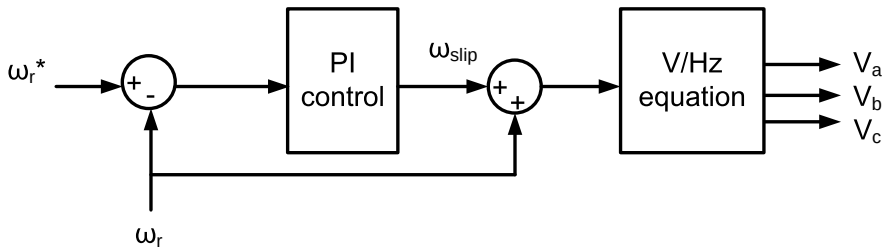

Figure 5.4: Volts/Hertz controller block diagram.

The total losses for the SCIG in the V/Hz configuration include the stator copper loss, rotor resistance loss, the core-loss resistance loss and the frictional loss. The total losses are given in the equation below:

$$P_{loss} = 3(I_s^2 R_s + I_r^2 R_r + I_m^2 R_c) + B_m \omega_r^2 \tag{5.10}$$

where I_s, I_r and I_m are the per-phase stator, rotor and magnetising currents respectively. Similarly R_s, R_r and R_c are the stator, rotor and core-loss resistances. B_m is the frictional factor and ω_r is the rotational speed.

This power loss was then fed into the thermal model developed in the previous section to determine the temperature rise in the machine over the simulation period.

5.4.2 Vector Controlled Doubly-Fed Induction Generator

In this configuration the rotor is no longer shorted and is instead fed by a back-to-back converter. The stator is fed directly from the grid as shown in Figure 5.5. The rotor converter injects voltages at slip frequency to achieve the desired speed of rotation.

The DFIG vector control used in this study follows the theory presented in [107]. In this type of control scheme the DFIG is represented in the d-q reference frame by using the Parks transformation presented in [71]. The controller operates so that the d-axis is aligned to the synchronously

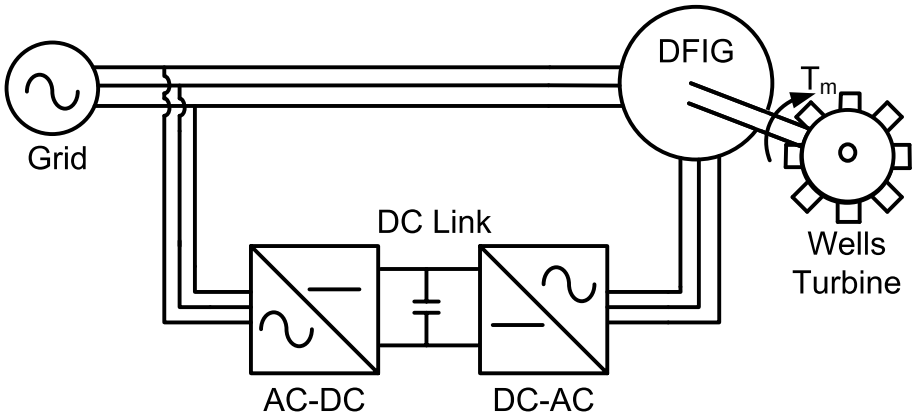

Figure 5.5: Vector controlled doubly-fed induction generator.

rotating stator flux vector. This allows for a de-coupled control between the electrical torque and the rotor excitation current to be obtained. The q-axis rotor current, i_{rq}, is used to control the torque command for the machine while d-axis current, i_{rd}, is used to control the reactive power in the machine. Reactive power control is an important attribute of the DFIG configuration. In this study it is assumed that the machine operates with zero reactive power demand apart from the reactive power supplied to the machine to provide for its magnetising current.

The q-axis current control involves a cascade PI structure where the outer-loop controls the rotational speed of the generator and the faster inner-loop controls the q-axis current. A block diagram of both the d- and q-axis controllers are shown in Figure 5.6.

In both cases the demand of the d-axis and q-axis voltages from the PI loops requires compensation terms to be added to ensure stable and accurate performance.

$$v_{rd}^{*} = v_{rd}^{\prime} - \omega_{slip}\,\sigma L_r i_{rq} \tag{5.11}$$

$$v_{rq}^{*} = v_{rq}^{\prime} + \omega_{slip}(L_m i_{ms} + \sigma L_r i_{rd}) \tag{5.12}$$

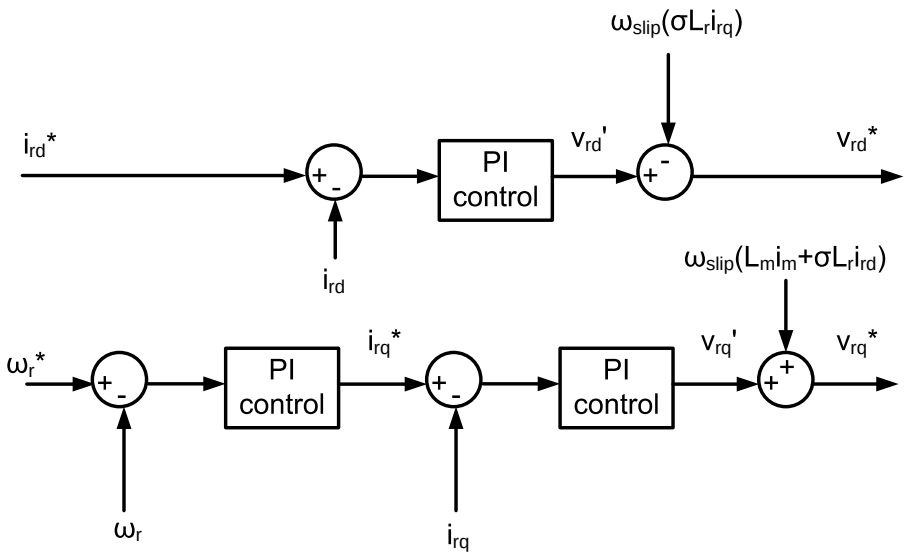

Figure 5.6: Control loops for vector controlled doubly-fed induction generator.

where σ is given by:

$$\sigma = 1 - \frac{L_m^2}{L_s L_r} \tag{5.13}$$

L_s and L_r are stator and rotor self inductances respectively and are given by the following expressions:

$$L_s = L_{ls} + L_m \tag{5.14}$$

$$L_r = L_{lr} + L_m \tag{5.15}$$

The dq voltages can then be converted to abc quantities by using the inverse Park transformation.

The losses of the DFIG drive when the machine operates under vector control are discussed in [108, 109]. The dq equivalent circuit of the DFIG, including core-loss is shown in Figure 5.7.

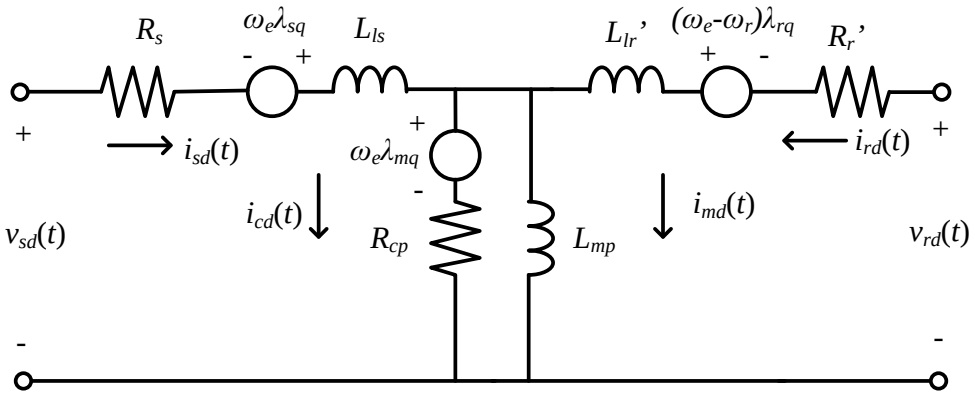

(a) d-axis Equivalent Circuit

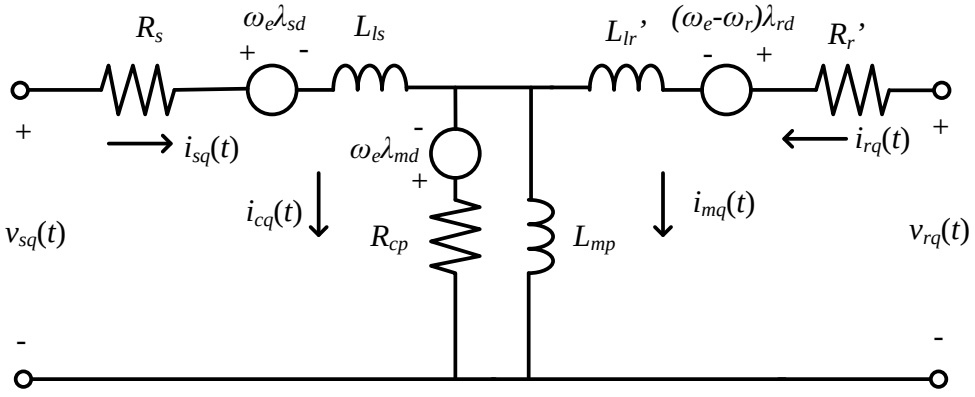

(b) q-axis Equivalent Circuit

Figure 5.7: dq Equivalent Circuit of doubly-fed induction machine

In this equivalent circuit ω_e is the electrical frequency, λ_{sq}, λ_{rq}, λ_{mq} is the q-axis flux linkage for the stator, rotor and magnetising branches, respectively. The parameters are labelled similarly for the d-axis equivalent circuit. From this equivalent circuit the losses in the DFIG are separated into copper and core-losses and are given by:

$$P_{cu-loss} = 1.5(i_{sd}^2 + i_{sq}^2)R_s + 1.5(i_{rd}^2 + i_{rq}^2)R_r \tag{5.16}$$

$$P_{core-loss} = 1.5(i_{cd}^2 + i_{cq}^2)R_c \tag{5.17}$$

where i_{cd} and i_{cq} are the core-loss dq currents and these are given by:

$$i_{cd} = \frac{\omega_e L_{ls} i_{sq}}{R_i} \tag{5.18}$$

$$i_{cq} = \frac{\omega_e(\lambda_{sd} - L_{ls} i_{ds})}{R_i} \tag{5.19}$$

where ω_e is the electrical frequency and λ_{sd} is the d-axis stator-flux linkage given by:

$$\lambda_{sd} = \int (v_{sd} - R_s i_{sd})dt \tag{5.20}$$

Taking the sum of the copper-losses and core losses and also taking the frictional losses into account gives the total losses in the DFIG. The total losses are then fed into the thermal model to determine the temperature rise of the machine.

5.5 Simulation results

The simulations were carried out in Matlab Simulink using the SimPowerSystems package. The simulations involve investigating the two electrical generator topologies presented in the previous section when excited by a high-density sea state based on data from the Irish test site. The sea state data and OWC WEC were scaled according to the Froude scaling method presented previously. The original data is scaled to determine the optimal scale for the device based on the thermal capabilities of the 30 kW generator for the three generator topologies.

The electrical parameters of the 30 kW generator are given in the following table. These results are obtained from the manufacturer's test data and are presented in [67].

Table 5.5: 30 kW induction machine equivalent circuit parameters

$R_s(\Omega)$	L_{ls}(mH)	$R_c(\Omega)$	L_m(mH)	$R'_r(\Omega)$	L'_{lr}(mH)
0.077	0.854	246	29.98	0.089	1.214

The machine ratings for friction coefficient, B_m, rated speed, ω_{rated}, rated torque, T_{rated} and maximum torque, T_m are given in Table 5.6.

Table 5.6: 30 kW induction machine mechanical parameters

B_m(Nms)	$\omega_{rated}(rad.s^{-1})$	T_{rated}(Nm)	T_m(Nm)
0.022	157	191	680

A theoretical torque-speed curve based on the electrical parameters shown in Table 5.5 is shown in Figure 5.8. The peak torque in this plot corresponds to the value of 680 Nm given in Table 5.6.

The use of the 30 kW generator for the original 1:2.5 scaled device would be excessive as the average power rating of this device does not match the induction generator. The peak-to-average pneumatic power ratio in this sea state was 11.5:1. However, due to aerodynamic stall occurring in the Wells turbine the mechanical shaft power peak to average ratio came down to 3.4:1. This

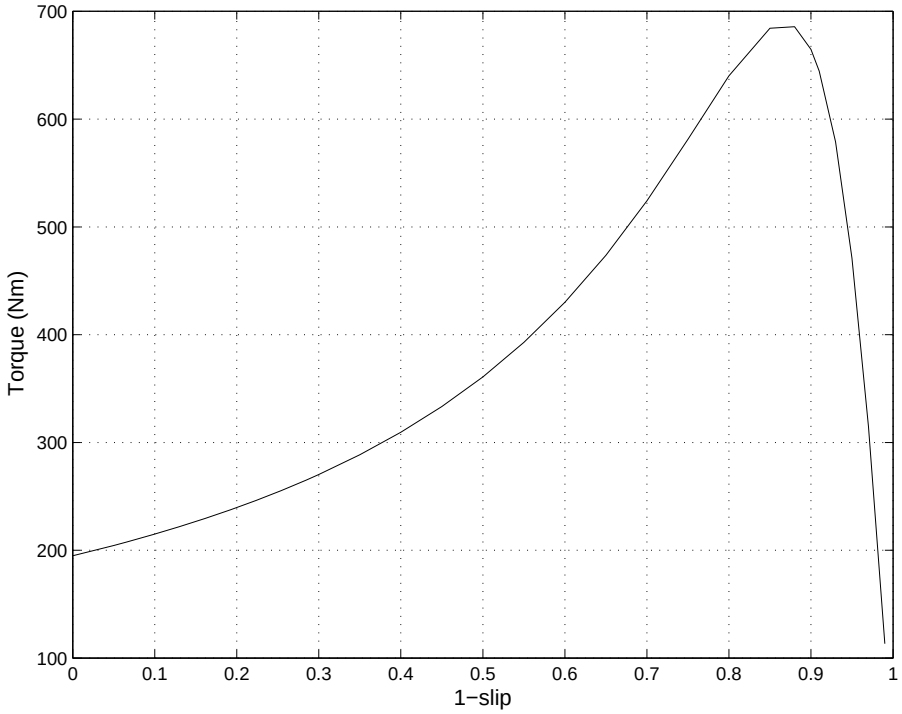

Figure 5.8: Theoretical torque versus speed curve of 30 kW induction machine.

ratio was close to that of the peak to average torque ratio of the induction generator. Therefore, the WEC device could be scaled to a level where the average mechanical power delivered from the device was 30 kW. A device scaling that corresponds to 30 kW average mechanical power was determined. The data relating to this scaled device is shown in the final column of Table 5.7 and is denoted 1: μ_1. The thermal stress on the machine is dependent on the topology used and therefore the sea state scale may need to be de-rated from 1: μ_1 depending on the thermal performance of each generation topology. Scale 1: μ_2 shown in Table 5.7 is a de-rated scale that corresponds to 27 kW average mechanical power.

The first-order thermal model presented previously was used to model the machines thermal response to the scaled sea state used as the generation source. The simulation was run for a time period of 3500 s which is close to 3 thermal time constants. The machine should therefore reach thermal stability in this time indicating the temperature rise to be expected in the machine.

Table 5.7: Froude scaling data for OWC WEC

Quantity	Scale	
-	1:μ_1	1:μ_2
D (m)	1.5	1.45
A_a (m^2)	0.99	0.93
N (rated) ($rad.s^{-1}$)	114	116
J ($kg.m^2.rad^{-1}$)	33.29	28.14
T (Nm)	609	532
P_m (rated) (kW)	109	97
P_m (avg) (kW)	30	27

5.5.1 V/Hz SCIG configuration

The first configuration considered was the V/Hz controlled SCIG. As mentioned earlier, the speed control employed was to maintain a fixed speed to ensure that the pneumatic power in the system was consistent with the measued test data. The speed of the generator was also controlled such that the speed would not run above the turbines rated level and maintaining the mechanical torque within specifed levels. The 1: μ_2 scale sea state in Table 5.7 was considered for this topology.

The temperature rise in the generator can be seen in Fig 5.9. It can be seen in this figure that the temperature was 142 ^{o}C. This is below the specified temperature rise of 110 ^{o}C and is within the thermal specifications of the machine from [101].

A section of the time domain speed and torque profile of the machine is shown in Fig 5.10. It can be seen in this profile that the speed of the machine was largely kept around the set point speed of 132 rad/s. The speed was controlled to a fixed value to ensure that the pneumatic power series used from the previous chapter remains valid in the scaled data used in this chapter. It also ensures that the mechanical power applied to the shaft in both topologies investigated is consistent at particular sea state scales, allowing for a valid comparison.

In this profile the peak torque experienced by the device is 450 Nm which is below the pull-out torque of the machine. Beyond the peak torque the machine would not be capable of providing enough counter torque to keep the speed of the system within its rated range, leading to unstable

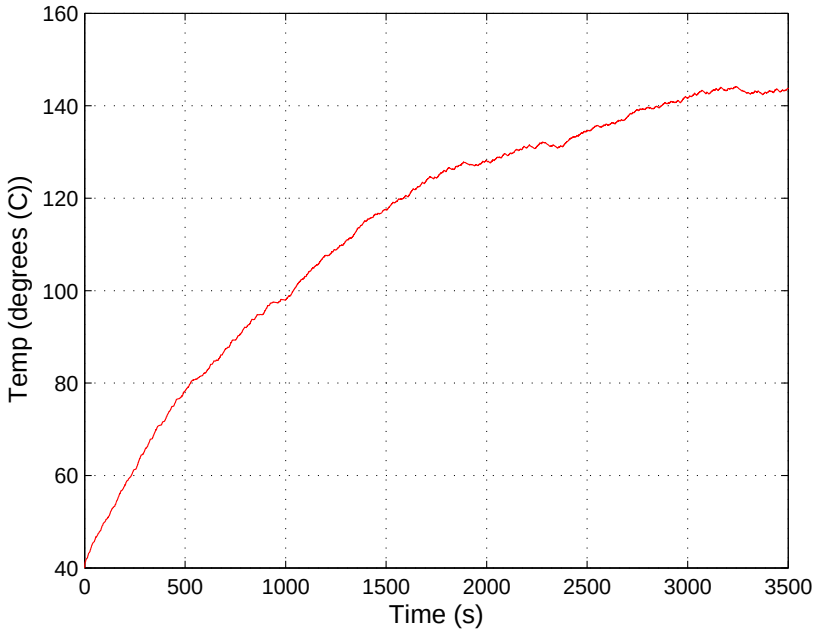

Figure 5.9: Temperaute rise in V/Hz SCIG topology.

operation of the system. Therefore, the machine rating is limited by both its thermal and its mechanical capabilities.

5.5.2 Vector controlled DFIG topology

The DFIG topology is also used with the 1: μ_2 scale sea state data. Like the SCIG topology the DFIG is controlled to have a fixed speed of 132 rad/s. This ensures consistent conditions to compare both topologies. The thermal rise in the machine is shown in Figure 5.11.

It can be seen from this figure that the temperature rise in the DFIG was close to the limit of 110 ^{o}C. The DFIG temperature reaches 148.2 ^{o}C. The DFIG therefore had a higher temperature rise than that of the SCIG. This is because the DFIG had higher losses than the SCIG. The stator and rotor copper losses in both topologies are comparible but the DFIG core-losses were higher than those of the SCIG and this lead to the higher temperature rise in the DFIG case.

One reason for this would be that both machines operate at different slip frequencies and

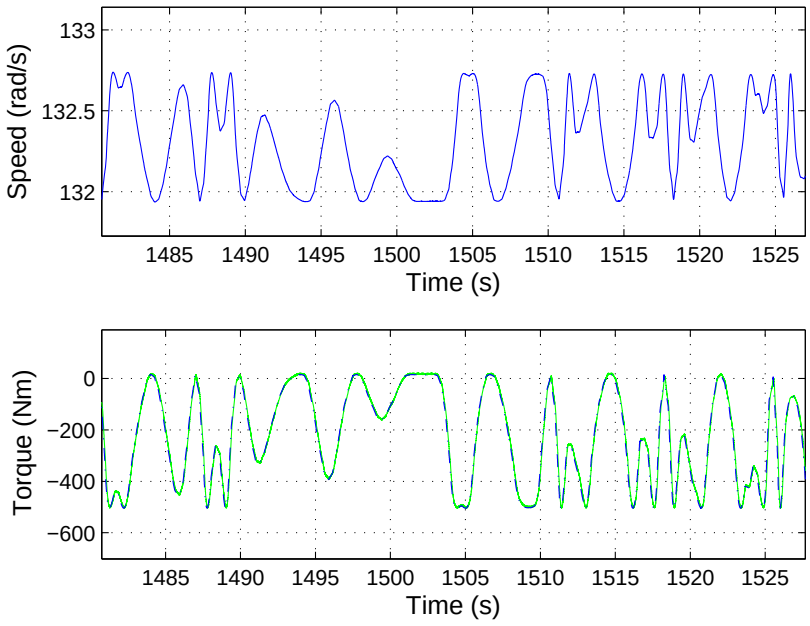

Figure 5.10: Speed (blue) and load torque (blue -·) and electromagnetic torque (green) versus time for V/Hz SCIG.

therefore the currents in the two topologies are at different frequencies. The SCIG is supplied by the V/Hz controller that supplies the stator at a frequency that allows the rotor speed to match the desired frequency. Conversely, in the DFIG topology the stator is supplied at grid frequency and the rotor is supplied with a frequency that results in the desired mechanical speed for the generator. The fact that the currents in each topology are operated at different frequencies would lead to different losses being observed.

The torque and speed profiles for the DFIG are shown in Figure 5.12. It can be seen that the electromagnetic torque and speed variations were very similar to that of the SCIG. This highlights the consistency in the conditions of both topologies. Slight differences between the plots in Figure 5.10 and Figure 5.12 are seen due to differences in the control loops of both topologies.

Forced cooling can be used on both the DFIG and SCIG to increase the rating of the WEC that can be used with the machine. However, the mechanical limit of the machine dictated by its

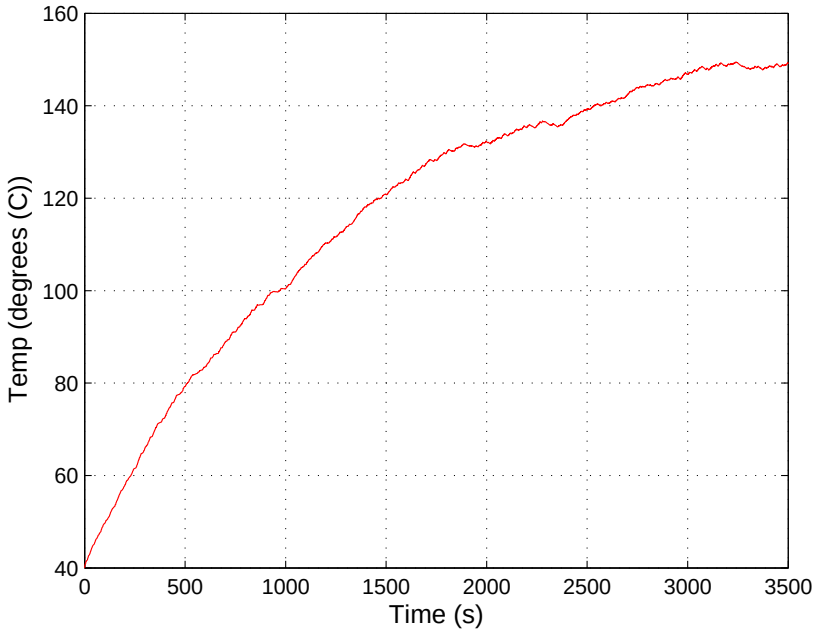

Figure 5.11: Temperature rise in vector-controlled DFIG topology.

pull-out torque would still need to be respected. Should the peak torque delivered by the Wells turbine exceed the pull-out torque of the induction machine, then the system will become unstable.

In the DFIG topology, a DC link and grid converter exists on the rotor circuit to de-couple the generator from the grid. The DFIG has a similar capability to the SCIG by having the option of power smoothing by using a variable speed system or employing energy storage to improve the power quality supplied to the grid. An advantage the DFIG has over the SCIG is that the converter only needs to be rated for the slip power and not the full rating of the machine. The DFIG can also operate in sub-synchronous and super-synchronous modes of operation with the speed range of operation above and below synchronism determined by the rotor converter rating.

A major drawback of the DFIG is that it is a brushed machine, which from a maintenance perspective is undesireable. The brush wear in the OWC WEC application is likely to be high due to the highly pulsating power profile experienced. In [28] the issue of brush wear is discussed and it is concluded that brushes would likely need to be changed twice annually under the oscillating

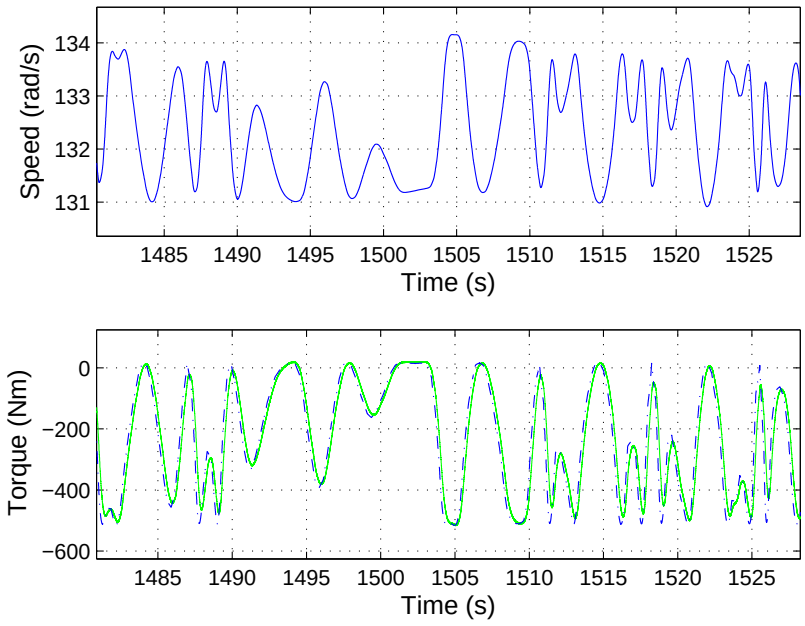

Figure 5.12: Speed (blue) and load torque (blue -·) and electromagnetic torque (green) versus time for vector controlled DFIG.

power delivered from the WEC. Due to the high cost of maintenance associated with these offshore devices it is generally perceived that a required maintenance regime to be performed bi-annually is unacceptable. This makes the DFIG less attractive for an offshore WEC.

In the case of a shore-based OWC WEC, the maintenance costs are significantly less and access to the electrical generator will be less problematic. This makes the DFIG a more viable option than in the case of the offshore device. As has been mentioned, brushed generators have been used in the shore-based OWC devices in Islay and the Azores [19–21].

In the case of the offshore OWC WEC, the SCIG is considered a more suitable option as it does not require brushes making it a more robust option. The application of forced cooling on the machine can also increase its range of operation beyond the device scale presented in this chapter.

5.6 Conclusion

The investigation of the thermal requirements and rating of an induction machine, when applied to an oscillating water column (OWC) type wave energy converter (WEC) through simulation, was presented. A first-order thermal model of the electrical machine was developed using datasheet parameters. This thermal model was then used to predict the overall temperature rise in the machine when the genertator was loaded with a typical high-energy sea state profile from the Irish test site. The Wells turbine model developed from Chapter 4 is used with the high-density pneumatic power data to represent the OWC WEC.

In order to investigate the machine for different WEC ratings the sea state pneumatic power data was scaled up using a method known as Froude scaling. This method allowed for consistent analysis to be carried out at various device scales.

Two generator topologies were investigated using the 30 kW induction generator and these were a Volts-to-Hertz (V/Hz) controlled squirrel cage induction generator (SCIG) and a vector controlled doubly-fed induction generator (DFIG). It was found that the 30 kW generator could be used with a sea state of average mechanical power of 27 kW. The V/Hz SCIG and DFIG both utilised speed control to maintain the speed and torque of the machine within rated specifications. Both the SCIG and DFIG topologies were found to remain within the thermal limits of the machine. The SCIG had a slightly better thermal performance than the DFIG as it had less losses than the DFIG.

The most suitable generation topology was the V/Hz SCIG as this generator was a robust option that had less maintenance concerns than the DFIG. The DFIG has the disadvantage of being a brushed machine making it an unsuitable option for offshore WECs.

The thermal capabilities of the machine could be extended through using forced cooling techniques. However, the mechanical ratings of the machine are likely to limit the machine as the torque supplied to the machine from the Wells turbine can exceed the pull-out torque of the machine. Thermal analysis of the generator can be carried out using more in-depth thermal models to determine hot-spot temperatures and conductivity within the machine.

6

Conclusions

This chapter summarises the thesis and the results obtained. A discussion of potential future work based on the findings of the thesis is also presented.

6.1 Thesis Summary

The doubly-fed induction machine (DFIM) is a popular choice for renewable generation technologies. The DFIM is widely used in the wind industry and has also been considered in wave energy converters. Various WEC technologies currently exist with the OWC WEC currently one of the most advanced. The DFIM has been employed in shore-based OWC WECs previously. The aim of the thesis is to present a novel method to characterise the doubly-fed induction machine, to val-

idate the characterisation procedures through experimental testing of the machines speed-torque curve and sensitivity analysis, to develop a software model to represent the power take-off of an OWC WEC and to provide analysis of the thermal requirements of an electrical generator when applied in an OWC.

The characterisation of the DFIM was presented initially. Chapter 2 introduces the test procedures employed to characterise the DFIM. These test procedures included IEEE Standard 112 tests, the series-coupling tests and the extended short-circuit (ESC) tests. The standard IEEE tests were initially presented and it was found that these tests made assumptions about the equivalent-circuit parameters in order to determine the parameters.

The series-coupling tests were introduced as a more direct method of determining the DFIM equivalent circuit. Three test models were obtained from these tests namely, cumulative, differential and average test models. The series-coupling methods involved a three-test procedure to realise the equivalent circuit of the machine these tests included the open-circuit rotor test, open-circuit stator test and the series-coupling tests. The series-coupling procedure was found to directly measure the machines parameters without requiring the assumptions made during the IEEE standard testing procedure. The extended short-circuit tests were used as a further three-test procedure to characterise the machine.

Chapter 3 presented the experimental testing of a PWB high-leakage transformer and two doubly-fed induction machines using the characterisation procedures discussed in Chapter 2. The characterisation of the PWB transformer highlights the strength of the series-coupling tests in predicting the equivalent circuit parameters of high-leakage devices when compared to the standard open- and short-circuit transformer tests.

The two DFIMs tested were a 1.1 kW DFIM from Terco and a 30 kW DFIM from Marelli. The series-coupling and extended short-circuit tests were found to produce equivalent circuit models that correlated well with the IEEE tests. In the case of the loosely coupled 1.1 kW DFIM, the series-coupling tests were found to perform best in predicting the torque-versus-speed curve of the machine. The IEEE and ESC tests were found to be less accurate around the peak torque of

the machine.

In the case of the well-coupled 30 kW DFIM, the IEEE and the differential test were found to produce comparible results in both equivalent circuit parameter measurement and torque-versus-speed curve predictions. The ESC tests were again found to be less accurate and this was because the flux conditions under test were not controlled, leading to error in parmater estimation.

Sensitivity analysis was carried out on the various testing procedures and it was found that the series-coupling tests were sensitive to measurement error. The cumulative test, in particular, was found to be highly sensitive to experimental measurement error because the test was carried out at the peak inductance point, whereas the differential test was found to be less sensitive due to it being carried out at the minimum inductance point. Due to the sensitivities of these tests it was important to ensure that the experimental set-up was correctly calibrated.

Chapter 4 focussed on the oscillating water column WEC and the Wells turbine. The Wells turbine was employed in the OWC WEC as part of the device power take-off. A scaled prototype OWC WEC situated at the Irish test site was analysed in this chapter. A characteristic curve depicting the non-dimensional torque-versus-flow coefficient characteristic of the turbine was developed using experimental data from a prototype device. Measurements from the device were taken and from these measurements the mechanical torque and airflow were derived. These parameters were then converted to non-dimensional quantities allowing for the development of a first-order non-dimensional characteristic curve for the turbine.

The non-dimensional curve was then included in a software model of the system. The model was validated by comparing the experimental measurements from three common sea states with the predicted output from the software model. The measured and predicted electrical output energies for each sea state were also compared to further validate the model.

Chapter 5 investigates the thermal rating and requirements of an induction generator coupled to a Wells turbine equipped OWC WEC. The non-dimensional Wells turbine model developed in Chapter 4 was utilised with the high power sea state data. The device sizing and rating as well as the sea state data were scaled using a method known as Froude scaling.

A first-order thermal model was used to determine the temperature rise within the machine. The simplified model was used to determine the overall temperature rise of the machine rather than specific hot-spot temperatures. The induction machine was configured in a Voltz-to-Hertz controlled squirrel cage induction generator configuration and also as a vector controlled doubly-fed induction generator.

The maximum device scale that the specified 30 kW induction generator could operate with, whilst remaining within its thermal limits, was determined through simulation and both topologies are compared on their thermal rise profiles.

It was found that a device rating with a mechanical power rating of 27 kW was suited to the 30 kW induction generator. Both generation topologies had similar temperature rises but the DFIG was found to have a higher temperature rise. The DFIG also had the disadvantage of being a brushed machine and therefore had more maintenance concerns than the SCIG. The SCIG was therefore proposed as the more suitable generation configuration for the offshore OWC WEC.

6.2 Suggestions for Future Work

The thesis develops a number of novel areas which can be developed further beyond the research carried out in this thesis. The first area of research that could be developed would be to further study the variation of parameters with controlled flux levels within the machine during the series-coupling tests. By setting the flux in the machine such that the machine enters magnetic saturation may lead to an enhanced model that would account for saturation in the core of the machine.

Secondly the implementation of a three test approach to the squirrel cage induction machine (SCIM) may also be of interest. The SCIM does not allow for access to the rotor in the same way as the DFIM and therefore the series-coupling tests would not be applicable as described in this thesis. An investigation into other connection configurations may lead to test procedures that improve parameter estimation for the SCIM.

Further development of the Wells turbine model may also be carried out. The model presented

was based on outflow data only and as has been mentioned the damping of the device may be different during inflow conditions. Therfore, by considering inflow data a second curve may be developed to more accurately represent the turbines performance under these conditions.

Furthermore, the data may be split into accelerating and decelerating flows. This would allow for the differences in the reciprocating flows to be modelled. This would open the possibility of modelling turbine hysteresis which would improve the predictions of the model in the stall regions.

Similarly the first-order thermal model used to represent the machine could be made more complex by utilising some of the methodologies described in Section 5.1.1. Increasing the model complexity would allow for a more in depth study of temperature rise within the machine and may also allow for thermal hot-spots to be detected. Experimental testing of a 30 kW induction generator would be required to determine the thermal parameters for the model.

An experimental test rig could also be developed to represent the system simulated in Chapter 5. A controlled machine could provide the required driving torque for an induction generator and thermal measurements to determine the rating of the device could also be carried out.

6.3 Thesis Contributions

The series-coupling tests have been demonstrated to be a more direct method of measuring the equivalent circuit parameters and thus develop a more enhanced model of the doubly-fed induction machine. Although the tests can be sensitive to measurement error they have been found to accurately characterise loosely-coupled machines. The differential test is the least sensitive of the series-coupling tests, and is the recommended method to characterise high-leakage devices. The differential test provided the most accurate predictions of the torque-versus-speed curves of the loosely-coupled machine outperforming the IEEE tests in these predictions. The series-coupling tests have also been shown to operate effectively on devices ranging from mW power levels to kW power levels.

The development of the Wells turbine characteristic curve provides a simple but effective

method of modelling the power take-off of an OWC WEC. The model has been used in this thesis to study the thermal rise of an induction generator. This model can also contribute to other studies in the development of the OWC WEC electrical system. Other areas of interest would include energy storage solutions and also whether the system is configured by a fixed- or variable-speed control system. A further application of the model would be in implementing it in a dynamic model suitable for load-flow and transient stability studies in power system software packages.

Finally, the thesis provided a study on the thermal ratings and requirements for a 30 kW induction generator. The study provides insights into the likely ratings of an induction generator to be connected to an OWC WEC. The results from the simulations can be used to develop a better understanding of the challenges faced in generating electrical power from the OWC WEC. The simulated results may also lead to experimental testing aimed at validating the simulated results presented in this thesis. Ultimately the simulated results provide a valuable insight for OWC WEC device developers in their choice of electrical generator.

Publications resulting from the research include papers presented at the IEEE Power Electronics Specialist Conference [110], IEEE Inductry Applications Society General Meeting [111], IEEE Transactions on Industry Applications [35, 112] and 8th European Wave and Tidal Energy Conference [113].

Bibliography

[1] "IEA Wind energy annual report 2007," World Wide Web electronic publication, pp. 1–286, 2008. [Online]. Available: http://www.ieawind.org/AnnualReports_PDF/2007/2007%20IEA%20Wind%20AR.pdf

[2] "Eirgrid annual report 2008," World Wide Web electronic publication, pp. 1–77, 2008. [Online]. Available: http://www.eirgrid.com/media/Annual%20Report%202008.pdf

[3] H. C. Soerensen and A. Weinstein, "Ocean energy: Position paper for IPCC," in *IPCC Scoping Conference on Renewable Energy*. International Energy Agency, 15–15, 2008, web page, pp. 1–8. [Online]. Available: http://www.eu-oea.com/euoea/files/ccLibraryFiles/Filename/000000000400/Ocean_Energy_IPCC_final.pdf

[4] "Ocean energy conversion in Europe," World Wide Web electronic publication, pp. 1–36, 2006. [Online]. Available: http://www.wave-energy.net/index_files/documents/CA-OEBROCHURE.pdf

[5] "Wave energy utilisation in Europe: Current status and perspectives," World Wide Web electronic publication, pp. 1–28, 2002. [Online]. Available: http://www.cres.gr/kape/pdf/download/Wave%20Energy%20Brochure.pdf

[6] "Ocean energy in Ireland," World Wide Web electronic publication, pp. 1–46, 2005. [Online]. Available: http://www.marine.ie/NR/rdonlyres/86491414-3E7E-48E5-A0E1-287CA9191C61/0/OceanEnergyStrategy.pdf

[7] A. Clement and et al., "Wave energy in europe: Current status and perspectives ," *Renewable and Sustainable Energy Reviews*, vol. 6, pp. 405–431, 2002.

[8] "Renewable energy development 2006," World Wide Web electronic publication, pp. 1–31, 2006. [Online]. Available: http://www.sei.ie/About_Energy/Energy_Policy/National_Policy_Drivers/Renewable_Energy_Development_2006.pdf

[9] H. Polinder and M. Scuotto, "Wave energy converters and their impact on power systems," in *Future Power Systems, 2005 International Conference on*, Nov. 18–18, 2005.

[10] D. J. Pizer, C. Retzler, R. M. Henderson, F. L. Cowieson, M. G. Shaw, B. Dickens, and R. Hart, "Pelamis WEC - recent advances in the numerical and experimental modelling programme," in *6th European Wave and Tidal Energy Conference*, Sept. 2005, pp. 373–378.

[11] M. Jasinski, W. Knapp, M. Faust, and E. Fris-Madsen, "The power takeoff system of the Multi-MW Wave Dragon wave energy converter," in *7th European Wave and Tidal Energy Conference*, Sept. 11–13, 2007, pp. 1042–1050.

[12] M. Prado, F. Gardner, M. Damen, and H. Polinder, "Modelling and test results of the Archimedes Wave Swing," *Proc IMechE Part A. J Power Energy*, vol. 20, pp. 855–868, Aug. 2006.

[13] [Online]. Available: http://www.pelamiswave.com/

[14] R. Henderson, "Design, simulation, and testing of a novel hydraulic power take-off system for the Pelamis wave energy converter," *Renewable energy*, vol. 31, no. 2, pp. 271–283, 2006.

[15] S. L. Caraher, R. Crozier, A. S. Mc Donald, M. A. Mueller, and J. P. Chick, "Integrated structural and electrical design of the linear permanent magnet synchronous machine," in *8th European Wave and Tidal Energy Conference*, Sept. 7–10, 2009, pp. 766–776.

[16] H. Polinder, B. Mecrow, A. Jack, P. Dickinson, and M. Mueller, "Conventional and TFPM linear generators for direct-drive wave energy conversion," *Energy Conversion, IEEE Transactions on*, vol. 20, no. 2, pp. 260 – 267, june 2005.

[17] M. A. Mueller, A. S. Mc Donald, K. Ochije, and J. Jeffrey, "Integrated structural and electrical design of the linear permanent magnet synchronous machine," in *7th European Wave and Tidal Energy Conference*, Sept. 11–13, 2007, pp. 1123–1128.

[18] A. F. de O. Falcão, "First generation wave power plants: Current status and R&D requiremants," *Journal of Offshore Mechanics and Arctic Egineering*, vol. 126, pp. 384–388, Nov. 2004.

[19] "Islay Limpet wave power plant," World Wide Web electronic publication, pp. 1–62, 2002. [Online]. Available: http://www.wavegen.co.uk/pdf/LIMPET%20publishable%20report.pdf

[20] "Islay Limpet project monitoring final report," World Wide Web electronic publication, pp. 1–37, 2002. [Online]. Available: http://www.wavegen.co.uk/pdf/art.1707.pdf

[21] A. de O. Falcão, "The shoreline OWC wave power plant at the Azores," in *4th European Wave and Tidal Energy Conference*, Sept. 2000, pp. 42–48.

[22] D. Evans and R. Porter, "Hydrodynamic characteristics of an oscillating water column device," *Applied Ocean Research*, vol. 17, pp. 155–164, May 1995.

[23] R. Datta and V. T. Ranganathan, "Variable-speed wind power generation using doubly fed wound rotor induction machine-a comparison with alternative schemes," *Energy Conversion, IEEE Transactions on*, vol. 17, no. 3, pp. 414–421, Sept. 2002.

[24] S. Muller, M. Deicke, and R. De Doncker, “Doubly fed induction generator systems for wind turbines,” *IEEE Industry Applications Magazine*, vol. 8, pp. 26–33, 2002. [Online]. Available: http://ieeexplore.ieee.org/lpdocs/epic03/wrapper.htm?arnumber=999610

[25] L. Ran, D. Xiang, L. Hu, and K. Abbott, “Voltage stability of an HVDC system for a large offshore wind farm with DFIGs,” in *AC and DC Power Transmission, 2006. ACDC 2006. The 8th IEE International Conference on*, 28-31 2006, pp. 150 – 154.

[26] G. Pannell, D. Atkinson, R. Kemsley, L. Holdsworth, P. Taylor, and O. Moja, “DFIG control performance under fault conditions for offshore wind applications,” *IEE Conference Publications*, vol. 2005, no. CP504, pp. v4–80–v4–80, 2005. [Online]. Available: http://link.aip.org/link/abstract/IEECPS/v2005/iCP504/pv4-80/s1

[27] M. Eichler, “Offshore but online: PCS6000 wind converter for 5 MW offshore wind turbines,” World Wide Web electronic publication, pp. 1–6, 2008. [Online]. Available: http://www.abb.ie/search.aspx?q=Offshore%20but%20online

[28] D. O’Sullivan and A. Lewis, “Generator selection for offshore oscillating water column wave energy converters,” in *Power Electronics and Motion Control Conference, 2008. EPE-PEMC 2008. 13th*, Sept. 2008, pp. 1790–1797.

[29] J. G. Hayes, N. O’Donovan, M. G. Egan, and T. O’Donnell, “Inductance characterization of high-leakage transformers,” in *Applied Power Electronics Conference and Exposition, 2003. APEC ’03. Eighteenth Annual IEEE*, vol. 2, Feb. 9–13, 2003, pp. 1150–1156.

[30] B. Heeres, D. Novotny, D. Divan, and R. Lorenz, “Contactless underwater power delivery,” in *Power Electronics Specialists Conference, PESC ’94 Record., 25th Annual IEEE*, Jun 1994, pp. 418–423 vol.1.

[31] R. Severns, E. Yeow, G. Woody, J. Hall, and J. Hayes, “An ultra-compact transformer for a 100 W to 120 kW inductive coupler for electric vehicle battery charging,” in *Applied Power*

Electronics Conference and Exposition, 1996. APEC '96. Conference Proceedings 1996., Eleventh Annual, vol. 1, Mar 1996, pp. 32–38 vol.1.

[32] J. G. Hayes, M. G. Egan, N. Wang, and T. O'Donnell, "Series-coupling Test Characterization of On-chip Silicon-integrated and PWB-integrated Transformers," in *Applied Power Electronics Conference, APEC 2007 - Twenty Second Annual IEEE*, Feb. 25–Mar. 2007, 2007, pp. 97–103.

[33] M. Brunet, T. O'Donnell, L. Baud, N. Wang, J. O'Brien, P. McCloskey, and S. O'Mathuna, "Electrical performance of microtransformers for dc-dc converter applications," *Magnetics, IEEE Transactions on*, vol. 38, no. 5, pp. 3174–3176, Sep 2002.

[34] C. Sullivan and S. Sanders, "Measured performance of a high-power-density microfabricated transformer in a dc-dc converter," in *Power Electronics Specialists Conference, 1996. PESC '96 Record., 27th Annual IEEE*, vol. 1, Jun 1996, pp. 287–294 vol.1.

[35] J. G. Hayes, D. Cashman, M. G. Egan, T. O'Donnell, and N. Wang, "Comparison of test methods for characterization of high-leakage two-winding transformers," *Industry Applications, IEEE Transactions on*, vol. 45, no. 5, pp. 1729–1741, Sept.-oct. 2009.

[36] D. Xiang, L. Ran, P. Tavner, and S. Yang, "Control of a doubly fed induction generator in a wind turbine during grid fault ride-through," *Energy Conversion, IEEE Transactions on*, vol. 21, no. 3, pp. 652–662, Sept. 2006.

[37] "IEEE standard test procedure for polyphase induction motors and generators," *IEEE Std 112-2004 (Revision of IEEE Std 112-1996)*, pp. 1–79, 2004.

[38] Z. Yuan, H. Lu, R. Kerkman, T. Nondahl, and R. Lukaszewski, "Parameter sensitivity analysis of flux observers for induction motors," in *Industry Applications Conference, 2007. 42nd IAS Annual Meeting. Conference Record of the 2007 IEEE*, Sept. 2007, pp. 1015–1022.

[39] A. V. Stankovic, E. L. Benedict, V. John, and T. A. Lipo, "A novel method for measuring induction machine magnetizing inductance," *Industry Applications, IEEE Transactions on*, vol. 39, no. 5, pp. 1257–1263, Sept./Oct. 2003.

[40] S. Djurovic, S. Williamson, and W. Yang, "Condition monitoring artefacts for detecting winding faults in wind turbine DFIGs," in *European Wind Energy Conference and Exhibition, 2009*, 16–19 2009.

[41] T. Lehtla, J. Joller, M. Lehtla, and J. Laugis, "Parameter identification and comparison of an induction motor models," in *Power Electronics and Variable Speed Drives, 2000. Eighth International Conference on (IEE Conf. Publ. No. 475)*, London, UK, 2000, pp. 201–205.

[42] H. Guesbaoui, O. Touhami, and C. Iung, "Identification of asynchronous machine parameters by a recursive least-squares method," in *Control Applications, 1994., Proceedings of the Third IEEE Conference on*, Glasgow, UK, Aug. 24–26, 1994, pp. 715–720.

[43] A. Lima, C. Jacobina, and E. de Souza Filho, "Nonlinear parameter estimation of steady-state induction machine models," *Industrial Electronics, IEEE Transactions on*, vol. 44, no. 3, pp. 390–397, Jun 1997.

[44] S. R. Shaw and S. B. Leeb, "Identification of induction motor parameters from transient stator current measurements," *Industrial Electronics, IEEE Transactions on*, vol. 46, no. 1, pp. 139–149, Feb. 1999.

[45] R. Wamkeue, I. Kamwa, and M. Chacha, "Unbalanced transients-based maximum likelihood identification of induction machine parameters," *Energy Conversion, IEEE Transactions on*, vol. 18, no. 1, pp. 33–40, Mar. 2003.

[46] K. Wang, J. Chiasson, M. Bodson, and L. M. Tolbert, "A nonlinear least-squares approach for identification of the induction motor parameters," *Automatic Control, IEEE Transactions on*, vol. 50, no. 10, pp. 1622–1628, Oct. 2005.

[47] L. R. Georges, A. G. Kladas, and S. N. Manias, "Finite element based production motor model for adaptive field-oriented drive for electrical vehicle," in *Industrial Electronics, 1995. ISIE '95., Proceedings of the IEEE International Symposium on*, vol. 2, Athens, Greece, July 10–14, 1995, pp. 639–642.

[48] R. Shindo, A. C. Ferreira, and G. A. Soares, "Calculation of polyphase induction motor parameters using the finite element method," in *Wireless Communications and Applied Computational Electromagnetics, 2005. IEEE/ACES International Conference on*, Apr. 3–7, 2005, pp. 662–665.

[49] R. D. Weerdt, E. Tuinman, K. Hameyer, and R. Belmans, "Finite element analysis of steady state behavior of squirrel cage induction motors compared with measurements," *Magnetics, IEEE Transactions on*, vol. 33, pp. 2093–2096, Mar. 1997.

[50] S. Williamson and M. J. Robinson, "Calculation of cage induction motor equivalent circuit parameters using finite elements," in *Electric Power Applications, IEE Proceedings B*, vol. 138, no. 5, Sept. 1991, pp. 264–276.

[51] K. Davey, "Predicting induction motor circuit parameters," *Magnetics, IEEE Transactions on*, vol. 38, no. 4, pp. 1774–1779, Jul 2002.

[52] M. Despalatovic, M. Jadric, and B. Terzic, "Identification of induction motor parameters from free acceleration and deceleration tests," *AUTOMATIKA-ZAGREB-*, vol. 46, pp. 123–128, 2005. [Online]. Available: http://crosbi.znanstvenici.hr/prikazi-rad?chset=ASCII&lang=EN&rad=272762

[53] R. J. Kerkman, J. D. Thunes, T. M. Rowan, and D. W. Schlegel, "A frequency-based determination of transient inductance and rotor resistance for field commissioning purposes," *Industry Applications, IEEE Transactions on*, vol. 32, no. 3, pp. 577–584, May/June 1996.

[54] M. Depenbrock and N. R. Klaes, "Determination of induction machine parameters and their dependancies on saturation," in *Industry Applications Society Annual Meeting, 1989. IAS '89. IEEE*, May 15–17, 1989, pp. 17–22.

[55] A. Proca and A. Keyhani, "Identification of variable frequency induction motor models from operating data," *Energy Conversion, IEEE Transactions on*, vol. 17, no. 1, pp. 24–31, Mar 2002.

[56] S. D. Sudhoff, D. C. Aliprantis, B. T. Kuhn, and P. L. Chapman, "Experimental characterization procedure for use with an advanced induction machine model," *Energy Conversion, IEEE Transactions on*, vol. 18, no. 1, pp. 48–56, Mar. 2003.

[57] C. R. Sullivan and S. R. Sanders, "Models for induction machines with magnetic saturation of the main flux path," *Industry Applications, IEEE Transactions on*, vol. 31, no. 4, pp. 907–917, July/Aug. 1995.

[58] S. Ansuj, F. Shokooh, and R. Schinzinger, "Parameter estimation for induction machines based on sensitivity analysis," *Industry Applications, IEEE Transactions on*, vol. 25, no. 6, pp. 1035–1040, Nov./Dec. 1989.

[59] Y. Koubaa, "Induction machine drive parameters estimation," in *Systems, Man and Cybernetics, 2002 IEEE International Conference on*, vol. 6, Oct. 6–9, 2002.

[60] J. Pedra and F. Corcoles, "Estimation of induction motor double-cage model parameters from manufacturer data," *Energy Conversion, IEEE Transactions on*, vol. 19, no. 2, pp. 310–317, June 2004.

[61] S. Djurovic, S. Williamson, and A. Renfrew, "A dynamic model for DFIGs with winding and/or excitation asymmetry," *IET Electric Power Applications*, vol. 3, no. 3, pp. 171–177, 2009.

[62] J. J. Cathey, *Electric Machines Analysis and Design Using Matlab.* McGraw-Hill, 2001.

[63] "Terco Sweden electrical machines laboratory." World Wide Web electronic publication, 2005. [Online]. Available: http://www.terco.se/en/?page=viewproducts&id=31

[64] "Three phase induction motors with wound rotors for hoists," Marelli Motori Product Catalog, pp. 1–30, 2003.

[65] M. Kayikci and J. Milanovic, "Reactive power control strategies for DFIG-based plants," *Energy Conversion, IEEE Transactions on*, vol. 22, no. 2, pp. 389–396, June 2007.

[66] S. Seman, J. Niiranen, S. Kanerva, A. Arkkio, and J. Saitz, "Performance study of a doubly fed wind-power induction generator under network disturbances," *Energy Conversion, IEEE Transactions on*, vol. 21, no. 4, pp. 883–890, Dec. 2006.

[67] S. Djurovic, "Analysis of doubly-fed induction generator under electrical fault conditions," Ph.D. dissertation, University of Manchester, 2007.

[68] T. O'Donnell, N. Wang, M. Brunet, S. Roy, A. Connell, J. Power, C. O'Mathuna, and P. McCloskey, "Thin film micro-transformers for future power conversion," in *Applied Power Electronics Conference and Exposition, 2004. APEC '04. Nineteenth Annual IEEE*, vol. 2, 2004, pp. 939 – 944 vol.2.

[69] *HP 4284A Precision LCR Meter Operation Manual*, 1998.

[70] M. I. o. T. Staff of the Department of Electrical Engineering, *Magnetic Circuits and Transformers*. MIT press, 1943.

[71] P. C. Krause, *Analysis of Electrical Machines*. Kingsport Press Inc., 1986.

[72] D. R. Kiran, A. Palani, S. Muthukumar, and V. Jayashankar, "Steady Grid Power From Wave Energy," vol. 22, no. 2, pp. 539–540, June 2007.

[73] S. Muthukumar, S. Kakumanu, S. Sriram, R. Desai, A. A. S. Babar, and V. Jayashankar, "On Minimizing the Fluctuations in the Power Generated from a Wave Energy Plant," in

Electric Machines and Drives, 2005 IEEE International Conference on, May 15–15, 2005, pp. 178–185.

[74] S. Muthukumar, S. Kakumanu, S. Sriram, and V. Jayashankar, "Energy storage considerations for a stand-alone wave energy plant," in *Electric Machines and Drives, 2005 IEEE International Conference on*, May 15–15, 2005, pp. 193–198.

[75] D. B. Murray, M. G. Egan, J. G. Hayes, and D. L. O' Sullivan, "Applications of supercapacitor energy storage for a wave energy converter system," in *8th European Wave and Tidal Energy Conference*, Sept. 7–10, 2009, pp. 788–795.

[76] W. Tease, "Dynamic Response of a Variable Pitch Wells Turbine," in *Proc. 5th European Wave Energy Conf*, Sept 2003.

[77] A. de O. Falcão and P. Justino, "OWC wave energy devices with air flow control," *Ocean Engineering*, vol. 26, no. 12, pp. 1275–1295, 1999.

[78] A. Brito-Melo, L. Gato, and A. Sarmento, "Analysis of Wells turbine design parameters by numerical simulation of the OWC performance," *Ocean Engineering*, vol. 29, no. 12, pp. 1463–1477, 2002.

[79] M. Scutto and A. F. de O. Falcão, "Wells and impulse turbines in an OWC wave power plant: A comparison," in *6th European Wave and Tidal Energy Conference*, Sept. 2005, pp. 463–470.

[80] R. Curran, T. Whittaker, and T. P. Stewart, "Aerodynamic conversion of ocean power from wave to wire," *Energy Conversion and Management*, vol. 39, pp. 1919–1929, 1998.

[81] V. Jayashankar, S. Anand, T. Geetha, S. Santhakumar, V. Jagadeesh Kumar, M. Ravindran, T. Setoguchi, M. Takao, K. Toyota, and S. Nagata, "A twin unidirectional impulse turbine topology for OWC based wave energy plants," *Renewable Energy*, vol. 34, no. 3, pp. 692–698, 2009.

[82] M. Folley, R. Curran, and T. Whittaker, "Comparison of LIMPET contra-rotating wells turbine with theoretical and model test predictions," *Ocean Engineering*, vol. 33, no. 8-9, pp. 1056–1069, 2006.

[83] R. Arlitt, K. Tease, R. Starzmann, and J. Lees, "Dynamic system modeling of an oscillating water column wave power plant based on characteristic curves obtained by computaional fluid dynamics to enhcance engineered reliability," in *7th European Wave and Tidal Energy Conference*, Sept. 11–13, 2007, pp. 1–8.

[84] P. Filianoti and S. M. Camporeale, "In field measurements on small scale OWC device," in *8th European Wave and Tidal Energy Conference*, Sept. 7–10, 2009, pp. 284–294.

[85] S. M. Camporeale and P. Filianoti, "Behaviour of a small wells turbine under randomly varying oscillating flow," in *8th European Wave and Tidal Energy Conference*, Sept. 7–10, 2009, pp. 690–696.

[86] ——, "Experimental verification of the stochastic model for predicting the performance of oscillating water column devices," in *8th European Wave and Tidal Energy Conference*, Sept. 7–10, 2009, pp. 914–923.

[87] R. Alcorn, "Wave station modelling based on the Islay prototype plant," Ph.D. dissertation, Queens University Belfast, 2000.

[88] A. de O. Falcão, "Control of an oscillating-water-column wave power plant for maximum energy production," *Applied Ocean Research*, vol. 24, pp. 73–82, 2002.

[89] P. Justino and A. de O. Falcão, "Rotational speed control of an owc wave power plant," *Journal of Offshore Mechanics and Arctic Engineering*, vol. 121, pp. 65–70, 1999.

[90] A. Valenzuela L, P. Verbakel, and J. Rooks, "Thermal evaluation for applying TEFC induction motors on short-time and intermittent duty cycles," in *Pulp and Paper Industry Technical Conference, 2002. Conference Record of the 2002 Annual*, 2002, pp. 91 –97.

[91] A. Boglietti, A. Cavagnino, and D. Staton, "Thermal analysis of TEFC induction motors," in *Industry Applications Conference, 2003. 38th IAS Annual Meeting. Conference Record of the*, vol. 2, oct. 2003, pp. 849 – 856 vol.2.

[92] D. Staton, A. Boglietti, and A. Cavagnino, "Solving the more difficult aspects of electric motor thermal analysis in small and medium size industrial induction motors," *Energy Conversion, IEEE Transactions on*, vol. 20, no. 3, pp. 620 – 628, sept. 2005.

[93] A. Boglietti, A. Cavagnino, and D. Staton, "TEFC induction motors thermal models: A parameter sensitivity analysis," *Industry Applications, IEEE Transactions on*, vol. 41, no. 3, pp. 756 – 763, may-june 2005.

[94] M. Rajagopal, K. Seetharamu, and P. Ashwathnarayana, "Transient thermal analysis of induction motors," *Energy Conversion, IEEE Transactions on*, vol. 13, no. 1, pp. 62 –69, mar 1998.

[95] R. Ibtiouen, S. Mezani, O. Touhami, N. Nouali, and M. Benhaddadi, "Application of lumped parameters and finite element methods to the thermal modeling of an induction motor," in *Electric Machines and Drives Conference, 2001. IEMDC 2001. IEEE International*, 2001, pp. 505 –507.

[96] J. Driesen, R. Belmans, and K. Hameyer, "Finite element modelling of thermal contact resistances and insulation layers in electrical machines," in *Electric Machines and Drives, 1999. International Conference IEMD '99*, may 1999, pp. 222 –224.

[97] P. Mellor, D. Roberts, and D. Turner, "Lumped parameter thermal model for electrical machines of TEFC design," *Electric Power Applications, IEE Proceedings B*, vol. 138, no. 5, pp. 205 –218, sep 1991.

[98] A. Boglietti, A. Cavagnino, M. Lazzari, and M. Pastorelli, "A simplified thermal model for variable-speed self-cooled industrial induction motor," *Industry Applications, IEEE Transactions on*, vol. 39, no. 4, pp. 945 – 952, july-aug. 2003.

[99] M. Duran and J. Fernandez, "Lumped-parameter thermal model for induction machines," *Energy Conversion, IEEE Transactions on*, vol. 19, no. 4, pp. 791 – 792, dec. 2004.

[100] J. Moreno, F. Hidalgo, and M. Martinez, "Realisation of tests to determine the parameters of the thermal model of an induction machine," *Electric Power Applications, IEE Proceedings* -, vol. 148, no. 5, pp. 393 –397, sep 2001.

[101] N. Ghai, "IEC and NEMA standards for large squirrel-cage induction motors-a comparison," *Energy Conversion, IEEE Transactions on*, vol. 14, no. 3, pp. 545 –552, sep 1999.

[102] "IEC 60034-1 Rotating electrical machines - Part 1: Rating and performance," *IEC International Standard 60034-1 (Eleventh Edition 2004-04)*, pp. 1–137, 2004.

[103] W. Leonhard, *Control of electrical drives*. Springer Verlag, 2001.

[104] "Results from the work of the European Thematic Network on Wave Energy," World Wide Web electronic publication, pp. 1–502, 2003. [Online]. Available: http://www.wave-energy.net/Library/WaveNet%20Full%20Report%2811.1%29.pdf

[105] J. F. Douglas, J. M. Gasiorek, J. A. Swaffield, and L. B. Jack, *Fluid Mechanics*. Prentice Hall, 2005.

[106] N. Mohan, *Electric Drives An Integrative Approach*. MNPERE, 2003.

[107] R. Pena, J. Clare, and G. Asher, "Doubly fed induction generator using back-to-back pwm converters and its application to variable-speed wind-energy generation," *Electric Power Applications, IEE Proceedings* -, vol. 143, no. 3, pp. 231 –241, may 1996.

[108] A. Abo-Khalil, H.-G. Park, and D.-C. Lee, "Loss minimization control for doubly-fed induction generators in variable speed wind turbines," nov. 2007, pp. 1109 –1114.

[109] S.-D. Wee, M.-H. Shin, and D.-S. Hyun, "Stator-flux-oriented control of induction motor considering iron loss," *Industrial Electronics, IEEE Transactions on*, vol. 48, no. 3, pp. 602 –608, jun 2001.

[110] D. P. Cashman, J. G. Hayes, and M. G. Egan, "Parameter characterisation of a doubly-fed induction machine using series-coupling and IEEE Std.112 test methods," in *Power Electronics Specialists Conference, 2008. PESC 2008. IEEE*, June 15–19, 2008, pp. 3836–3842.

[111] ——, "Comparison of Test Methods for Characterisation of a Doubly-fed Induction Machine," in *Industry Applications Society Annual Meeting, 2008. IAS '08. IEEE*, Edmonton, Alta., Oct. 5–9, 2008, pp. 1–8.

[112] D. Cashman, J. Hayes, M. Egan, S. Djurovic, and S. Smith, "Comparison of test methods for characterisation of doubly-fed induction machines," *Industry Applications, IEEE Transactions on*, vol. 46, no. 5, Sept.-oct. 2010.

[113] D. P. Cashman, D. L. O' Sullivan, M. G. Egan, and J. G. Hayes, "Modelling and analysis of an offshore oscillating water column wave energy converter," in *8th European Wave and Tidal Energy Conference*, Sept. 7–10, 2009, pp. 924–933.

A

Appendix A

A.1 Transformation of parallel magnetising branch to series branch

The following section derives the parallel-to-series transformation equations for the magnetising branch of the doubly-fed induction machine shown in Chapter 2. The transformation is based on the equivalent circuits shown in Figure 2.1 and Figure 2.4.

A.1.1 Parallel to series branch transformation

Figure A.1 summarises the parallel and series magnetising branches from the equivalent circuits shown in Figure 2.1 and Figure 2.4.

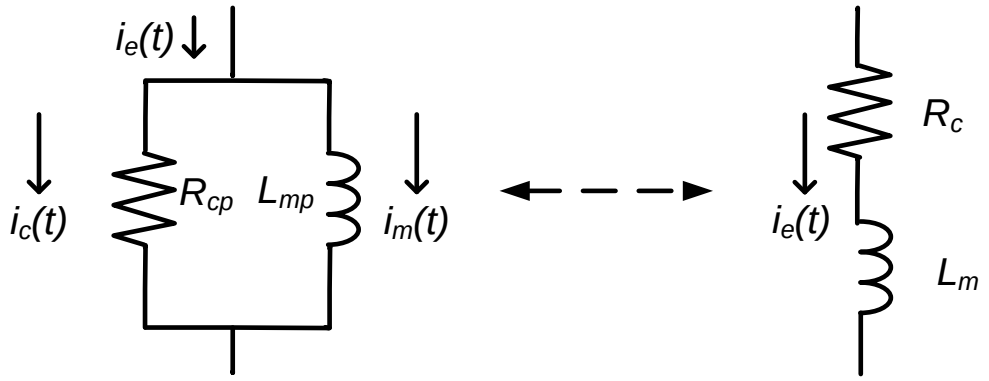

Figure A.1: Parallel-to-series transformation of DFIM magnetising branch

Analysing this figure and considering the impedance in each branch should be equivalent, the following expression can be obtained:

$$R_c + j\,\omega_e L_m = \frac{R_{cp} j\,\omega_e L_{mp}}{R_{cp} + j\,\omega_e L_{mp}} \tag{A.1}$$

By taking (A.1) and breaking up the parallel-impedance expression into real and imaginary components the resistance and reactance of the series branch can be determined.

$$R_c + j\,\omega_e L_m = \frac{R_{cp} j\,\omega_e L_{mp}}{R_{cp} + j\,\omega_e L_{mp}} \left(\frac{R_{cp} - j\,\omega_e L_{mp}}{R_{cp} - j\,\omega_e L_{mp}} \right) \tag{A.2}$$

$$R_c + j\,\omega_e L_m = \frac{j\,R_{cp}^2 \omega_e L_{mp} + R_{cp}\,\omega_e^2 L_{mp}^2}{R_{cp}^2 + \omega_e^2 L_{mp}^2} \tag{A.3}$$

$$R_c + j\,\omega_e L_m = \frac{R_{cp}\,\omega_e^2 L_{mp}^2}{R_{cp}^2 + \omega_e^2 L_{mp}^2} + j\frac{R_{cp}^2 \omega_e L_{mp}}{R_{cp}^2 + \omega_e^2 L_{mp}^2} \tag{A.4}$$

The series-branch resistance is the real part of the expression in (A.4) and the series-branch inductance is the imaginary part of (A.4). Thus, R_c and L_m are given as:

$$R_c = \frac{R_{cp}\,\omega_e^2 L_{mp}^2}{R_{cp}^2 + \omega_e^2 L_{mp}^2} \tag{A.5}$$

$$L_m = \frac{R_{cp}^2 L_{mp}}{R_{cp}^2 + \omega_e^2 L_{mp}^2} \tag{A.6}$$

These expressions are equivalent to those presented in (2.27) and (2.28) in Chapter 2.

A.1.2 Series to parallel branch transformation

Using a similar method as shown above, by considering Figure A.1 the series to parallel inverse transformation can be carried out.

$$\frac{1}{\frac{1}{R_{cp}} + \frac{1}{j\,\omega_e L_m}} = R_c + j\,\omega_e L_m \tag{A.7}$$

$$\frac{1}{R_{cp}} + \frac{1}{j\,\omega_e L_m} = \frac{1}{R_c + j\,\omega_e L_m} \tag{A.8}$$

The expression again needs to be arranged in a manner that the real and reactive components can be equated to determine the resistance and reactance of the parallel branch.

$$\frac{1}{R_{cp}} + \frac{1}{j\,\omega_e L_m} = \frac{1}{R_c + j\,\omega_e L_m}\left(\frac{R_c - j\,\omega_e L_m}{R_c - j\,\omega_e L_m}\right) \tag{A.9}$$

$$\frac{1}{R_{cp}} + \frac{1}{j\,\omega_e L_m} = \frac{R_c - j\,\omega_e L_m}{R_c^2 + \omega_e^2 L_m^2} \tag{A.10}$$

Rearranging (A.10) to obtain the resistance and inductance of the parallel branch gives the following expressions:

$$R_{cp} = \frac{R_c^2 + \omega_e^2 L_m^2}{R_c} \tag{A.11}$$

$$L_m = \frac{R_c^2 + \omega_e^2 L_m^2}{\omega_e^2 L_m} \tag{A.12}$$

This gives the expressions given in (2.29) and (2.30) in Chapter 2.

B

Appendix B

B.1 Sensitivity Analysis Equations Derivations

The following section explains the sensitivity analysis equations shown in Tables 2.5 and 2.6. Sample calculations to show the method for determining the values in the sensitivity tables in Chapter 2 are also shown.

The expressions shown in Table 2.5 are derived using the parameter equations in Chapter 2 and substituting in the experimental measured quantities in each case. The sensitivity of each output circuit parameter is then determined for an error in each of the measured quantities using

the sensitivity function.

$$S_{YX} = \frac{\delta Y}{\delta X}\frac{X}{Y} \approx \frac{\frac{\Delta Y}{Y}}{\frac{\Delta X}{X}} \tag{B.1}$$

For example, if the first expression in Table 2.5 is looked at it can be seen that this expresses the sensitivity of stator resistance, R_s, to variations in the measured open-circuit rotor voltage in the cumulative test procedure. The equation for R_s for the cumulutive test procedure shown in Table 2.3 in Chapter 2 is shown below:

$$R_s = \frac{(2n+1)R_{s-or} + R_{r-os} - R_{cum}}{2n} \tag{B.2}$$

Equation (B.2) can be rearranged to be expressed in terms of the measured quantities that are used to calculate the resistances in the expression. These quantities are the open-circuit rotor, open-circuit stator and cumulative voltages, currents and power factors. Thus, equation (B.2) can be expressed as:

$$R_s = \frac{(2n+1)\,\frac{V_{s-or}\,PF_{s-or}}{I_{s-or}} + \frac{V_{r-os}\,PF_{r-os}}{I_{r-os}} - \frac{V_{cum}\,PF_{cum}}{I_{cum}}}{2n} \tag{B.3}$$

The sensitivity function involves taking the partial derivative of the output function with respect to the varying quantity meaning that all other quantities are held constant. In this case, the partial derivative of R_s is taken with respect to V_{s-or}.

$$\frac{\delta R_s}{\delta V_{s-or}} = \left(1 + \frac{1}{2n}\right)\frac{PF_{s-or}}{I_{s-or}} \tag{B.4}$$

Taking equation B.4 and multiplying by V_{s-or}/R_s gives the sensitivity function:

$$S_{V_{s-or}R_s} = \left(1 + \frac{1}{2n}\right)\frac{PF_{s-or}}{I_{s-or}}\,\frac{V_{s-or}}{R_s} \tag{B.5}$$

It can be seen from Tables 2.5 and 2.6 that the same expression is obtained for the sensitivity of

R_s to power factor. For all resistive elements the sensitivity to voltage is equal to the sensitivity to power factor. In the case of the current I_{s-or} it can be seen that the expression for the sensitivity is simply equal to $-S_{VY}$ for all equivalent circuit parameters.

In the case of reactances the sensitivities for voltages and power factors differ. Initially the sensitivity of X_s to V_{s-or} for the cumulative test is considered. From Table 2.3 the stator leakage inductance from the cumulative test is given by:

$$L_{ls} = \frac{(2n+1)L_{s-or} + L_{r-os} - L_{cum}}{2n} \tag{B.6}$$

This can again be expressed in terms of the measured experimental quantites as given below:

$$X_{ls} = \frac{(1+2n)\,\frac{V_{s-or}\,Sin(\theta_{s-or})}{I_{s-or}} + \frac{V_{r-os}\,Sin(\theta_{r-os})}{I_{r-os}} - \frac{V_{cum}\,Sin(\theta_{cum})}{I_{cum}}}{2n} \tag{B.7}$$

where θ is the power factor angle and is given by the following expression:

$$\theta = Cos^{-1}(PF) \tag{B.8}$$

The partial derivative of X_{ls} with respect to open-circuit rotor voltage, V_{s-or}, is given by the following expression:

$$\frac{\delta X_s}{\delta V_{s-or}} = \left(1 + \frac{1}{2n}\right) \frac{Sin(\theta_{s-or})}{I_{s-or}} \tag{B.9}$$

The full sensitivity function can therefore be given by:

$$S_{V_{s-or}X_s} = \left(1 + \frac{1}{2n}\right) \frac{Sin(\theta_{s-or})}{I_{s-or}} \frac{V_{s-or}}{X_s} \tag{B.10}$$

For the case of the sensitivity of X_{ls} to PF_{s-or} equation (B.8) must be substituted into equa-

tion (B.7).

$$X_{ls} = \frac{\frac{(1+2n)V_{s-or}\,Sin(Cos^{-1}(PF_{s-or}))}{I_{s-or}} + \frac{V_{r-os}\,Sin(Cos^{-1}(PF_{r-os}))}{I_{r-os}} - \frac{V_{cum}\,Sin(Cos^{-1}(PF_{cum}))}{I_{cum}}}{2n} \quad \text{(B.11)}$$

The partial derivative of equation (B.11) is calculated by use of the chain rule of differential calculus thus giving:

$$\frac{\delta X_{ls}}{\delta PF_{s-or}} = -\left(1+\frac{1}{2n}\right)\frac{V_{s-or}\,PF_{s-or}}{I_{s-or}\sqrt{1-PF_{s-or}^2}} \quad \text{(B.12)}$$

The sensitivity function for X_{ls} to PF_{s-or} is therefore given by:

$$S_{PF_{s-or}X_{ls}} = -\left(1+\frac{1}{2n}\right)\frac{V_{s-or}\,PF_{s-or}}{I_{s-or}\sqrt{1-PF_{s-or}^2}}\,\frac{PF_{s-or}}{X_{ls}} \quad \text{(B.13)}$$

This method can be carried out on all test methods for all equivalent circuit parameters to complete Tables 2.5 and 2.6. In the case of the ESC test methods the equations for the parameters are complex functions and therefore expressions for the partial derivatives of these equations are quite complicated. The solutions for the ESC sensitivities can be found using mathematical software.

Mathematical software is also used to determine the sensitivities of maximum torque, full-load mechanical power and full-load reactive power to equivalent circuit parameters. The values for these sensitivities are presented in Tables 3.7 for the 1.1 kW Terco DFIM.

B.1.1 Sample Calculations

Sample calculations are now presented for the sensitivities of stator resistance, R_s, and stator leakage reactance, X_{ls}, to open-circuit rotor voltage and power factor in the cumulative test to outline the method of determining the values in Table 3.8 for the 1.1 kW Terco DFIM.

The cumulative test experimental values for stator resistance, R_s, stator leakage reactance, X_{ls}, open-circuit rotor voltage current and power factor are shown in Table B.1.

Initially the sensitivity of R_s to V_{s-or} is investigated. The values of Table B.1 are substituted

Table B.1: Experimental measurement for cumulative test method.

Test	$R_s(\Omega)$	$X_{ls}(\Omega)$	V_{s-or} (V)	I_{s-or}(A)	PF_{s-or}	n
Cum	2.6	5.9	126.1	1.05	0.114	0.667

into equation (B.5) to determine the sensitivity value. This is shown in the procedure below:

$$S_{V_{s-or}R_s} = \left(1 + \frac{1}{2n}\right) \frac{PF_{s-or}}{I_{s-or}} \frac{V_{s-or}}{R_s}$$

$$S_{V_{s-or}R_s} = \left(1 + \frac{1}{2(0.667)}\right) \frac{0.114}{1.05} \frac{126.1}{2.64}$$

$$S_{V_{s-or}R_s} = 9.08$$

This value demonstrates that a 1% overestimation error in V_{s-or} will lead to a 9.08% overestimation error in R_s. As mentioned previously the sensitivity in current measurement is opposite in sign to the voltage sensitivity meaning that an equivalent 1% error in I_{s-or} will lead to an underestimation error in R_s. The sensitivity of R_s to PF_{s-or} is equivalent to the sensitivity of R_s to V_{s-or}.

For the stator leakage reactance, X_{ls}, the procedure for determining the sensitivity to V_{s-or} is shown below:

$$S_{V_{s-or}X_{ls}} = \left(1 + \frac{1}{2n}\right) \frac{Sin(\theta_{s-or})}{I_{s-or}} \frac{V_{s-or}}{X_{ls}}$$

$$S_{V_{s-or}X_{ls}} = \left(1 + \frac{1}{2(0.667)}\right) \frac{Sin(Cos^{-1}(0.114))}{1.05} \frac{126.1}{5.9}$$

$$S_{V_{s-or}X_{ls}} = 35.52$$

Similarly using equation (B.13) the sensitivity of X_{ls} to PF_{s-or} can be determined using the

following calculation:

$$S_{PF_{s-or}X_{ls}} = -\left(1+\frac{1}{2n}\right)\frac{V_{s-or}\,PF_{s-or}}{I_{s-or}\sqrt{1-PF_{s-or}^2}}\,\frac{PF_{s-or}}{X_{ls}}$$

$$S_{PF_{s-or}X_{ls}} = -\left(1+\frac{1}{2(0.667)}\right)\frac{126.1\,0.114}{1.05\sqrt{1-(0.114)^2}}\,\frac{0.114}{5.9}$$

$$S_{PF_{s-or}X_{ls}} = -0.47$$

It can be seen clearly that the reactive components in the machine are much more sensitive to voltage and current measurement errors than they are to errors in power factor measurements.

This method can be carried out for each measurement quantity and each equivalent circuit parameter to complete Table 3.8. The differential test method senstivities for the 1.1 kW Terco DFIM and 30 kW Marelli DFIM are shown in Tables 3.9 and 3.13 and use the same method.

C

Appendix C

C.1 Experimental Results

This appendix gives the experimental measurements taken during testing of the devices presented in Chapter 3.

The data shown in the following tables correspond to that taken for the tests used in the IEEE characterisation procedures for both the 1.1 kW and 30 kW. The results for the 1.1 kW DFIM are shown in tables C.1, C.2 and C.3 for the no-load, locked rotor and dc tests respectively.

The open-circuit stator, open-circuit rotor, differential, cumulative and short circuit test measurements are shown in tables C.4, C.5, C.6, C.7 and C.8 respectively. The measurements used to

determine the results presented in Chapter 3 are highlighted in bold in these tables.

The data relating to the dc machines used to load the 1.1 kW and 30 kW DFIMs in the development of the torque versus speed curves for each machine are shown in table C.9. The torque versus speed data for the 1.1 kW machine is shown in Table C.10 while the 30 kW DFIM data is shown in Table C.18.

The no-load, locked-rotor and dc test measurement data for the 30 kW Marelli DFIM are shown in tables C.11, C.12 and C.13. The open-circuit stator, open-circuit rotor, differential and short circuit measurements are shown in tables C.14, C.15, C.16 and C.17 respectively. The numbers shown in bold in these tables are the numbers used in to obtain the results presented in Chapter 3.

Table C.1: Experimental measurements for 1.1 kW DFIM for No-load test

V_{ph} (V)	I_{ph} (A)	PF	ω_r (rad s^{-1})
33.46	0.90	0.717	131.58
57.57	0.70	0.591	144.65
83.06	0.77	0.414	153.12
116.56	0.99	0.305	153.94
131.83	1.11	0.305	154.78
152.06	1.28	0.236	155
179.75	1.55	0.209	155.19
217.57	2.05	0.173	155.36

Table C.2: Experimental measurements for 1.1 kW DFIM for locked-rotor test

V_{ph} (V)	I_{ph} (A)	PF
12.384	1.05	0.65
12.788	1.075	0.655
13.833	2.008	0.635
16.472	1.388	0.649
31.593	2.69	0.63
31.985	2.736	0.629
37.037	3.145	0.631
42.037	3.584	0.628
52.042	4.433	0.629
63.745	5.433	0.632
75.598	6.436	0.639

Table C.3: Experimental measurements for 1.1 kW DFIM for dc test

Phases	U1-V1	U1-W1	V1-W1	Average
R_{ph-ph}	4.85	4.84	4.84	4.843
R_s	2.425	2.42	2.43	2.422

Table C.4: Experimental measurements for 1.1 kW DFIM for open-circuit rotor test

V_{ph} (V)	I_{ph} (A)	PF	$R(\Omega)$	L (mH)
40.90	0.36	0.149	16.48	356
52.26	0.45	0.143	16.6	366
126.09	**1.05**	**0.114**	**13.73**	**381**
184.29	1.61	0.1	11.47	364

Table C.5: Experimental measurements for 1.1 kW DFIM for open-circuit stator test

V_{ph} (V)	I_{ph} (A)	PF	$R(\Omega)$	L (mH)
27.16	0.54	0.181	9.11	158
32.32	0.63	0.174	8.92	161
83.99	**1.57**	**0.138**	**7.39**	**169**
122.98	2.41	0.124	6.33	161

Table C.6: Experimental measurements for 1.1 kW DFIM for cumulative test

V_{ph} (V)	I_{ph} (A)	PF	$R(\Omega)$	L (mH)
67.69	0.2205	0.146	44.82	967
84.86	0.2698	0.14	44.03	992
205.59	**0.6302**	**0.11**	**35.89**	**1033**
300.33	0.9639	0.094	29.29	988

Table C.7: Experimental measurements for 1.1 kW DFIM for differential test

V_{ph} (V)	I_{ph} (A)	PF	$R(\Omega)$	L (mH)
22.83	1.09	0.335	7.03	63
28.73	1.35	0.326	6.94	64
67.48	**3.14**	**0.297**	**6.38**	**65**
97.66	4.82	0.3	6.08	62

Table C.8: Experimental measurements for 1.1 kW DFIM for short-circuit test

V_{ph} (V)	I_{ph} (A)	PF	$R(\Omega)$	L (mH)
12.9	1.09	0.656	7.75	28
15.9	1.35	0.651	7.69	29
37.2	**3.14**	**0.638**	**7.57**	**29**
59.2	4.82	0.667	8.19	29

Table C.9: 1.1 kW and 30 kW dc machine parameters

Rating (kW)	R_a (Ω)	k_t (V.s.rad^{-1})	T_{cfw} (Nm)
1.1	1.513	0.4674	0.856
30	0.494	2.582	4.392

Table C.10: Experimental measuremanets for torque versus speed profile of 1.1 kW DFIM

V_{s-line} (V)	I_{s-line} (A)	V_{dc} (V)	I_{dc} (A)	ω_r (rad s^{-1})	s	R_{ext} (Ω)
124.89	0.958	69.19	0	149.03	0.0512	open
124.94	1.026	68.48	0.148	147.24	0.063	462.70
124.94	1.031	68.43	0.167	147.24	0.063	409.76
124.92	1.031	68.33	0.19	146.84	0.065	359.63
124.9	1.075	68.11	0.221	146.85	0.0651	308.19
124.9	1.15	67.54	0.438	145.96	0.0708	154.20
124.9	1.18	66.88	0.66	145.46	0.074	101.33
124.85	1.38	64.97	1.23	141.40	0.100	52.74
124.83	1.551	63.32	1.61	140.08	0.108	39.33
124.79	1.704	61.92	1.97	137.97	0.122	31.43
124.74	2.074	58.86	2.81	132.24	0.158	20.92
124.7	2.457	55.46	3.56	125.14	0.203	15.58
124.64	3.131	49.6	4.602	115.48	0.265	10.78
124.55	4.23	37.1	5.55	90.29	0.42	6.69
124.51	4.72	30.25	5.598	75.81	0.517	5.404
124.56	4.93	26.8	5.36	67.22	0.572	5
114.28	5.013	16.34	4.03	45.99	0.71	4.05
113.7	5.001	13.46	4.01	37.90	0.759	3.361

Table C.11: Experimental measurements for 30 kW DFIM for no-load test

V_{ph} (V)	I_{ph} (A)	PF	ω_r (rad s^{-1})
170.25	3.30	0.390	156.45
180.81	3.37	0.381	156.56
192.01	3.60	0.332	156.67
201.92	3.82	0.299	156.68
209.60	3.78	0.307	156.68
221.21	4.04	0.275	156.76
233.01	4.27	0.249	156.76
243.48	4.34	0.241	157.07

Table C.12: Experimental measurements for 30 kW DFIM for locked-rotor test

V_{ph} (V)	I_{ph} (A)	PF
18.03	5.53	0.293
25.36	7.76	0.284
33.47	10.22	0.279
41.56	12.71	0.270
49.36	15.12	0.267
58.30	17.89	0.266
61.73	18.94	0.263
64.51	19.84	0.264
67.51	20.74	0.264

Table C.13: Experimental measurements for 30 kW DFIM for dc test

Phases	U1-V1	U1-W1	V1-W1	Average
R_{ph-ph}	0.806	0.816	0.822	0.815
R_s	0.403	0.408	0.411	0.407

Table C.14: Experimental measurements for 30 kW DFIM for open-circuit rotor test

V_{ph} (V)	I_{ph} (A)	PF	$R(\Omega)$	L (mH)
157.11	2.73	0.0794	4.55	181.47
168.29	**2.93**	**0.0781**	**4.47**	**181.47**
176.92	3.08	0.077	4.41	181.47
192.90	3.37	0.0753	4.31	181.47
205.14	3.58	0.0741	4.24	181.47

Table C.15: Experimental measurements for 30 kW DFIM for open-circuit stator test

V_{ph} (V)	I_{ph} (A)	PF	$R(\Omega)$	L (mH)
59.43	7.37	0.0827	0.642	25.585
63.55	**7.86**	**0.0787**	**0.632**	**25.58**
66.46	8.23	0.0797	0.629	25.58
73.16	9.05	0.0758	0.613	25.58
77.30	9.57	0.0732	0.599	25.58

Table C.16: Experimental measurements for 30 kW DFIM for differential test

V_{ph} (V)	I_{ph} (A)	PF	$R(\Omega)$	L (mH)
103.21	4.39	0.089	2.10	74.52
110.53	**4.69**	**0.088**	**2.07**	**74.52**
116.57	4.95	0.0814	2.05	74.52
126.38	5.38	0.0855	2.01	74.52
134.55	5.73	0.084	1.977	74.52

Table C.17: Experimental measurements for 30 kW DFIM for short-circuit test

V_{ph} (V)	I_{ph} (A)	PF	$R(\Omega)$	L (mH)
12.37	4.097	0.348	1.05	9.01
14.4	**4.78**	**0.339**	**1.02**	**9.01**
16.20	5.37	0.335	1.01	9.01
17.42	5.78	0.331	0.997	9.01
18.22	6.05	0.329	0.99	9.01

Table C.18: Experimental measuremanets for torque versus speed profile of 30 kW DFIM

V_{s-line} (V)	I_{s-line} (A)	V_{dc} (V)	I_{dc} (A)	ω_r (rad s^{-1})	s	R_{ext} (Ω)
190.26	4.34	222.9	0	154.67	0.015	open
189.20	3.77	221.7	0.417	155.19	0.012	531.65
188.13	3.82	221.4	0.464	154.88	0.014	477.15
190.59	3.73	221	0.533	154.98	0.013	414.63
190.14	3.82	220	0.612	154.56	0.016	359.47
190.04	3.94	220	0.739	154.57	0.016	297.70
189.76	4.029	219.6	0.926	154.46	0.017	237.149
189.21	4.278	219.2	1.216	154.36	0.017	180.26
189.16	4.77	218.5	1.876	154.04	0.019	116.47
189.17	4.85	217.8	2.429	153.94	0.02	89.66
189.56	5.39	217.7	2.74	153.83	0.02	79.57
188.37	6.051	216.5	3.651	153.10	0.025	59.30
188.01	7.375	216	5.396	152.47	0.029	40.03
188.54	7.747	215.4	6.153	152.16	0.031	35.01
186.11	9.847	214	7.87	150.79	0.04	27.19
186.48	10.64	213.7	8.573	150.16	0.044	24.93
182.25	13.74	215.2	11.14	147.97	0.058	19.32
183.11	15.00	213.3	12.31	146.92	0.065	17.33
181.48	16.31	210.8	13.01	145.351	0.075	16.20
180.58	16.73	209.7	13.43	144.72	0.078	15.61
179.83	17.13	209	13.97	144.30	0.081	14.96
177.49	18.583	206.3	14.27	142.314	0.094	14.46
175.72	19.84	203.8	14.14	140.95	0.103	14.41

D

Appendix D

D.1 Development of non-dimensional torque versus flow coefficient curve

The following section outlines the development of the non-dimensional torque versus flow coefficient characteristic curve for the Wells turbine shown in Chapter 4.

Data from a common sea-state was taken and the non-dimensional torque and flow coefficient were determined using the method shown in Section 4.4 of Chapter 4. A scatter diagram of the non-dimensional torque versus flow coefficient for the sea-state is shown in Figure D.1.

The data shown in Figure D.1 is for both inflow and outflow from the OWC WEC chamber.

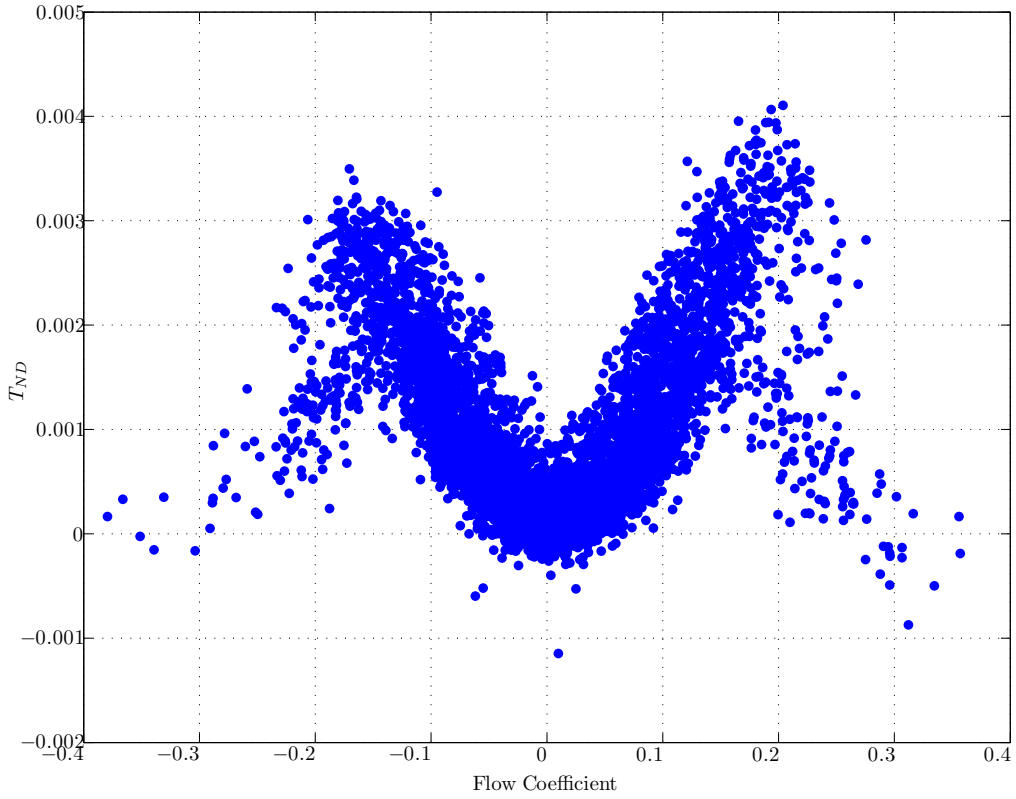

Figure D.1: Scatter plot of ND Torque vs Flow coefficient for common sea-state

A symmetry between the inflow and outflow can be seen and the assumption that these regimes performed equally was made. The outflow data was solely considered for the study.

The theory of the Wells turbine assumes that the rotational speed of the turbine is constant and therefore the data shown in Figure D.1 were divided into speed ‘bins’ of 20 RPM intervals. A selection on speed bins in the range of 1770-1890 RPM are shown in Figure D.2. The data shown in this figure is for the outflow data.

The speed bins could then be taken individually to determine a characteristic for the turbine in each case. Figure D.3 shows one of the speed bins in isolation.

It can be seen from this figure that there is still a significant amount of scatter present. In order to further remove this scatter the data within each speed bin is further sub-divided into groups of

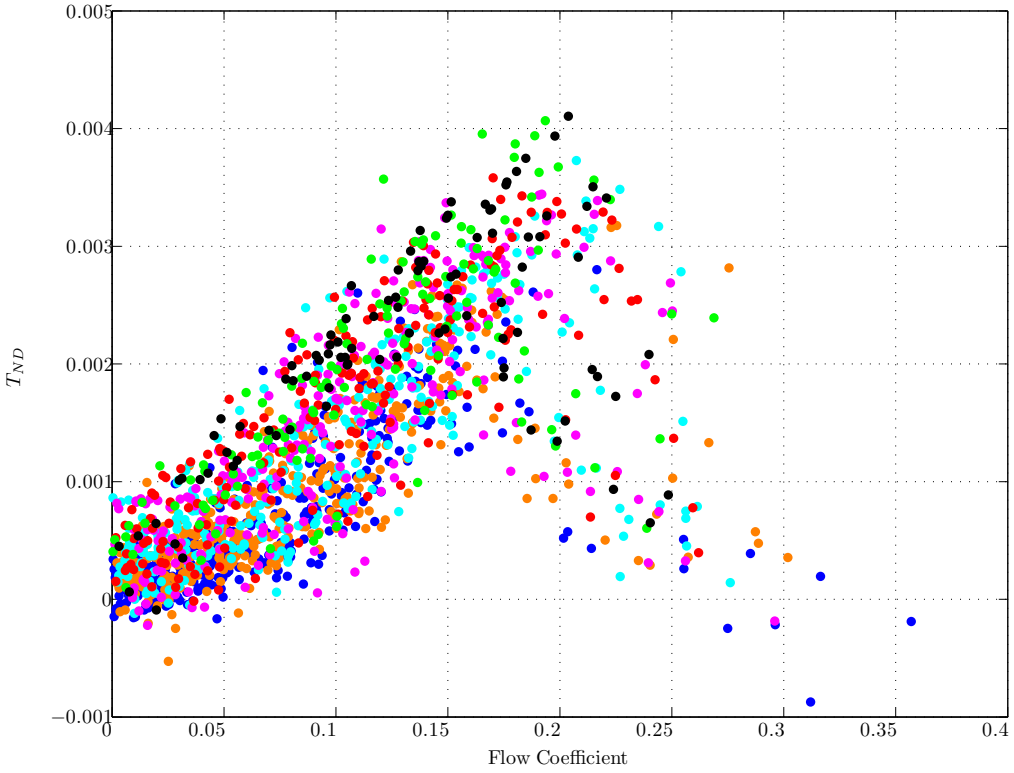

Figure D.2: Scatter plot of ND Torque vs Flow coefficient divided in speed bins

flow coefficinet Φ. This grouping of data can be seen for the selected speed bin in Figure D.4.

In this figure the speed bin is divided into groups of 0.02 intervals of Φ. This is highlighted by the different colour points shown in Figure D.4. The scatter in this plot was then removed by determining the mean non-dimensional torque in each of the Φ sub-groups in Figure D.4. This allows for the curve shown in Figure D.5 to be determined.

Using a similar method for the other speed bins in the sea-state, a family of curves can be determined as shown in Figure D.6. Different colour curves are shown for the different speed bins with the curve developed in Figure D.5 is highlighted in red.

A best fit curve is developed through the scatter shown in this figure to determine the characteristic curve of the Wells turbine as shown in Figure 4.4 of Chapter 4.

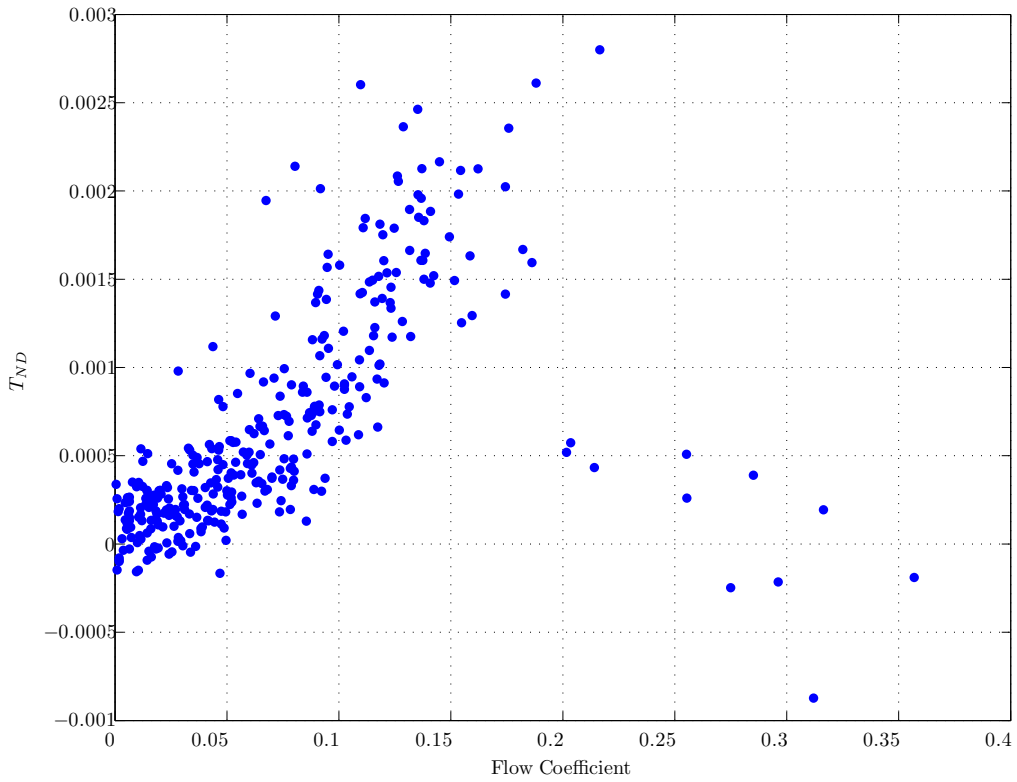

Figure D.3: Scatter plot of ND Torque vs Flow coefficient for one speed bin

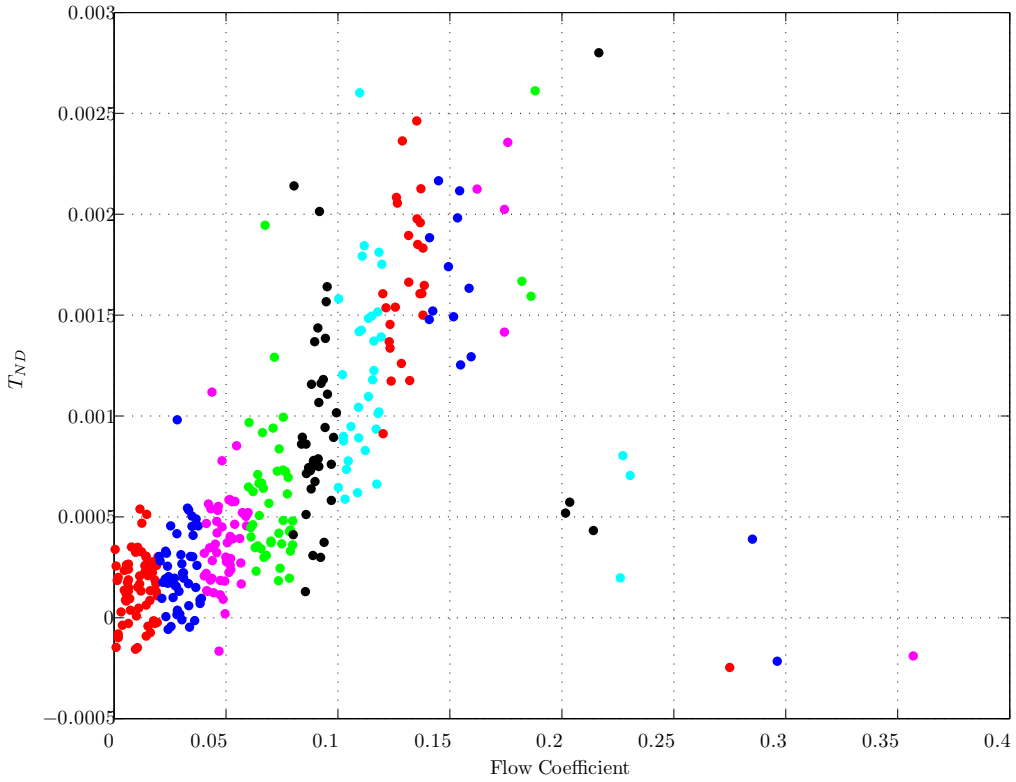

Figure D.4: Scatter plot of ND Torque vs Flow coefficient for one speed bin split into groups of Φ

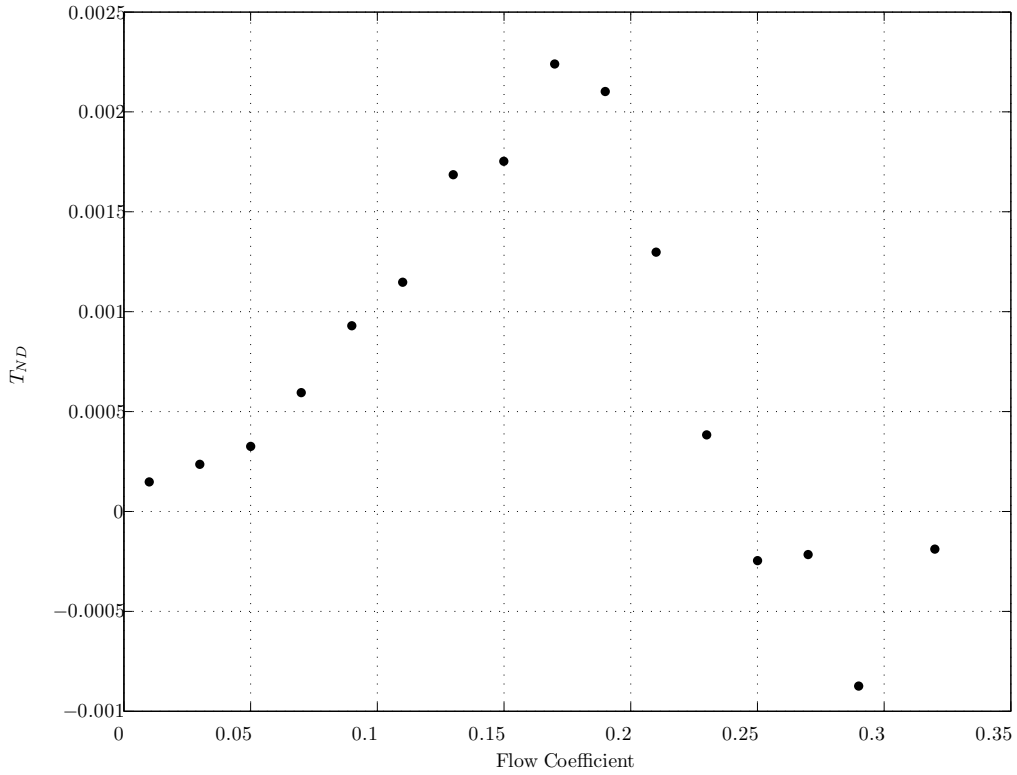

Figure D.5: Averaged scatter plot of ND Torque vs Flow coefficient for one speed bin

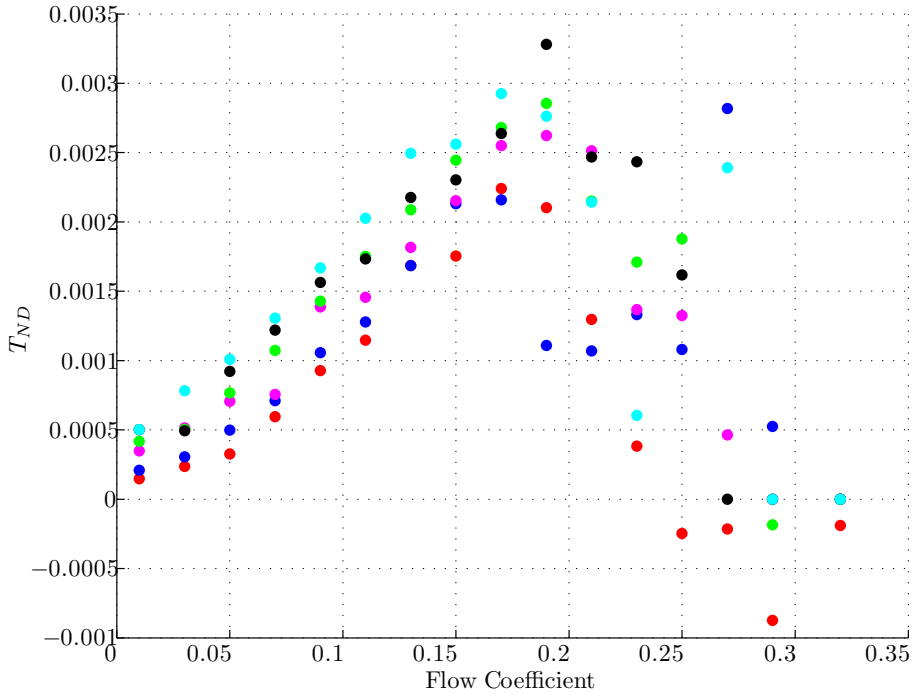

Figure D.6: Scatter plot of ND Torque vs Flow coefficient for all speed bins

E

Appendix E

E.1 Froude Scaling

This section outlines the method behind determining the Froude scaling factors shown in Tables 5.3 and 5.4.

When scaling device models, similarities between geometric, dynamic and kinematic data must exist. Forces acting on models of various scales must therefore act in a similar fashion [105]. The Froude number is a non-dimensional quantity and is used to relate inertial and gravitational forces on models at different scales. The Froude number is determined using the ratio of the inertial force to the gravitational force. The inertial force F_j and gravitational force F_g are given

below:

$$F_j = m\,a \tag{E.1}$$

$$F_g = m\,g \tag{E.2}$$

where m is mass, a is acceleration and g is acceleration due to gravity. Mass m, acceleration a and velocity u can be given by the following expressions.

$$m = \rho\,l^3 \tag{E.3}$$

$$a = \frac{u}{t} \tag{E.4}$$

$$u = \frac{l}{t} \tag{E.5}$$

where ρ is density, u is velocity, t is time and l is length.

By substituting equations (E.3)-(E.5) into (E.1) and (E.1) and rearranging gives the following expressions for F_j and F_g

$$F_j = \rho\,u^2\,L^2 \tag{E.6}$$

$$F_g = \rho\,g\,l^3 \tag{E.7}$$

The ratio of F_j to F_g is given below:

$$\frac{F_j}{F_g} = \frac{\rho\, u^2\, l^2}{\rho\, g\, l^3}$$

$$\frac{F_j}{F_g} = \frac{u^2}{g\, l}$$

For dynamic similarity between a scaled model and a full-scale device the following equality must be held:

$$\frac{u_m^2}{g_m\, l_m} = \frac{u_f^2}{g_f\, l_f}$$

$$\frac{u_m}{\sqrt{g_m\, l_m}} = \frac{u_f}{\sqrt{g_f\, l_f}} = F_n$$

where the subscripts m and f denote scaled model and full-scale model respectively. F_n is the Froude number and is therefore given as:

$$F_n = \frac{u}{\sqrt{g\, l}} \tag{E.8}$$

As has been mentioned geometric similarity must exist between scaled models and full-scale systems therefore the scaling ratio μ can be related to the length of both systems as given below:

$$\mu = \frac{l_f}{l_m} \tag{E.9}$$

By equating the Froude numbers of the full-scale system and the scaled model system the scaling ratios can be determined for length and velocity:

$$\frac{u_f}{\sqrt{l_f\, g_f}} = \frac{u_m}{\sqrt{l_m\, g_m}}$$

$$\frac{u_f}{u_m} = \sqrt{\frac{l_f}{l_m}}$$

$$\frac{u_f}{u_m} = \sqrt{\mu} \tag{E.10}$$

Therefore the scaling of velocity is given by $\sqrt{\mu}$.

By using the physical units of desired physical quantities the scaling ratios can be derived for each quantity. For example, considering the units of velocity as metres per second ($m\,s^{-1}$) and noting that the scale of dimension in metres is μ, then it can be seen that the dimension of time in seconds would be $\sqrt{\mu}$. Similarly by considering the units of acceleration as metres per second squared ($m\,s^{-2}$) the scaling factor can be determined to be unity.

This method can be carried out for all physical quantities in Tables 5.3 and 5.4 to obtain the scaling ratios for each of the quantities.

E.2 Sample Calculations

This section gives some sample calculations to show how the device parameters scale based on the Froude scaling ratios. Table E.1 shows the scaling ratios of the physical quantities related to the OWC WEC. The values of the original 1:2.5 scale is shown with the data given on a per unit basis. The final column of the table shows the 1:1 full-scale device ratings in per-unit. In the case of scaling 1:2.5 device to a 1:1 full-scale device the scaling ratio μ is given as 2.5 from (5.7).

The calculation of the values shown in Table E.1 are shown below. As mentioned earlier dimesion scales with the scaling factor μ therefore the turbine diameter will scale by the following expression:

$$D_1 = \mu\, D_{2.5}$$

$$D_1 = 2.5$$

where D_1 is the full-scale turbine diameter and $D_{2.5}$ is the turbine diameter at 1:2.5 scale.

Table E.1: Froude scaling data for OWC WEC

Quantity	Scale		
-	ratio	1:2.5	1:1
D (p.u.)	μ	1	2.5
A_a (p.u.)	μ^2	1	6.25
N (rated) (p.u.)	$\mu^{-1/2}$	1	0.63
J (p.u.)	μ^5	1	97.66
T (p.u.)	μ^4	1	39.06
P_m (rated) (p.u.)	$\mu^{3.5}$	1	24.7

Similarly the annular area A_a scales to μ^2. The rotational speed of the turbine N will scale to $\mu^{-1/2}$ this calculation is shown below:

$$N_1 = \mu^{-1/2}\, N_{2.5}$$

$$N_1 = 2.5^{-1/2}$$

$$N_1 = 0.63$$

where N_1 is the full-scale rotational speed and $N_{2.5}$ is the rotational speed at 1:2.5 scale.

Inertia can be seen to scale to μ^5 and torque scales μ^4. The rated mechanical power of the device is seen to scale to $\mu^{3.5}$. The calculation of scaled mechanical power is shown below:

$$P_{m1} = \mu^{3.5} P_{m2.5}$$

$$P_{m1} = 2.5^{3.5}$$

$$P_{m1} = 24.7$$

where P_{m1} and $P_{m2.5}$ is the mechanical power at full scale and at 1:2.5 scale, respectively.